ACTA DE EVALUACIÓN DE LA TESIS DOCTORAL
(FOR EVALUATION OF THE ACT DOCTORAL THESIS)

Año académico *(academic year)*: 2018/19

DOCTORANDO *(candidate PHD)*: YUAN, LEI
D.N.I./PASAPORTE *(Id.Passport)*: ****05774
PROGRAMA DE DOCTORADO *(Academic Committee of the Programme)*: **D441-ELECTRÓNICA: SISTEMAS ELECTRÓNICAS AVANZADOS. SISTEMAS INTELIGENTES**
DEPARTAMENTO DE *(Department)*: ELECTRÓNICA
TITULACIÓN DE DOCTOR EN *(Phd title)*: **DOCTOR/A POR LA UNIVERSIDAD DE ALCALÁ**

En el día de hoy 31/10/2018, reunido el tribunal de evaluación, constituido por los miembros que suscriben el presente Acta, el aspirante defendió su Tesis Doctoral realizada mediante **Convenio de Cotutela**, en la Universidad de Xi'an (China).*In today assessment met the court, consisting of the members who signed this Act, the candidate defended his doctoral thesis carried out through joint supervision Convention at the Xiàn University of Technology)* , elaborada bajo la dirección de *(prepared under the direction of)* ALVARO HERNÁNDEZ ALONSO//YUAN, YANG

Sobre el siguiente tema *(Title of the doctoral thesis)*: STUDY ON REAL-TIME TRACK BREAKAGE DETECTION SYSTEM AND SIGNAL PROCESSING

Finalizada la defensa y discusión de la tesis, el tribunal acordó otorgar la CALIFICACIÓN GLOBAL[1] de (**no apto, aprobado, notable** y **sobresaliente**) *(After the defense and defense of the thesis, the court agreed to grant the GLOBAL RATING (fail, pass, good and excellent)*: _____ EXCELLENT· _____

City...... X.I'AN , CHINA

Fdo. *(Signed)*: ...JUN LI...   Fdo. *(Signed)*: ZHAOIAN YANG   Fdo. *(Signed)*: ...JESÚS UREÑA...

Fdo. *(Signed)*: ...ZHIBIN PAN...   Fdo. *(Signed)*: ...NINGMEI YU...   Fdo. *(Signed)*: ...YUAN YANG...

FIRMA DEL ALUMNO (candidate's signature),

Con fecha 19 de noviembre de 2018 la Comisión Delegada de la Comisión de Estudios Oficiales de Posgrado, a la vista de los votos emitidos de manera anónima por el tribunal que ha juzgado la tesis, resuelve:

☒ Conceder la Mención de ''Cum Laude''
☐ No conceder la Mención de ''Cum Laude''

Fdo. *(Signed)*: ....

Fdo. *(Signed)*: ...YUAN LEI...

La Secretaria de la Comisión Delegada

[1] La calificación podrá ser "no apto" "aprobado" "notable" y "sobresaliente". El tribunal podrá otorgar la mención de "cum laude" si la calificación global es de sobresaliente y se emite en tal sentido el voto secreto positivo por unanimidad. *(The grade may be "fail" "pass" "good" or "excellent". The panel may confer the distinction of "cum laude" if the overall grade is "Excellent" and has been awarded unanimously as such after secret voting.)*.

INCIDENCIAS / OBSERVACIONES:
(Incidents / Comments)

One of the member [original] of the jury did not attend. According to Chinese regulations if there are more than 5 present members, de jury can be formed and act.
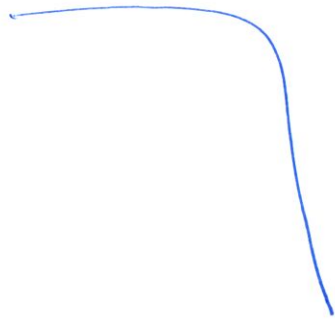
En aplicación del art. 14.7 del RD. 99/2011 y el art. 14 del Reglamento de elaboración, autorización y defensa de la tesis doctoral, la Comisión Delegada de la Comisión de Estudios Oficiales de Posgrado, en sesión pública de fecha 19 de noviembre, procedió al escrutinio de los votos emitidos por los miembros del tribunal de tesis para determinar si a la misma se le concede la mención cum laude, arrojando como resultado que la tesis defendida por YUAN, LEI, el día 31 octubre de 2018 titulada STUDY ON REAL-TIME TRACK BREAKAGE DETECTION SYSTEM AND SIGNAL PROCESSING, ha obtenido los votos secretos positivos por unanimidad.

In application of art. 14.7 of RD. 99/2011 and art. 14 of the Regulation regarding the writing, authorisation and examination of doctoral theses, in public session on 19 november, the Delegate Commission of the Official Postgraduate Studies Committee scrutinised the votes cast in secret by the members of the thesis's examining panel in order to determine whether said thesis should be awarded the distinction of "cum laude". The outcome of the scrutiny was that the thesis defended by YUAN, LEI on 10/31/2018 with the title STUDY ON REAL-TIME TRACK BREAKAGE DETECTION SYSTEM AND SIGNAL PROCESSING has obtained a unanimously favourable vote.

Por lo tanto, se resuelve otorgar a dicha tesis la,
Wherefore, the Official Postgraduate Studies Committee resolves to grant said thesis the,

MENCIÓN "CUM LAUDE"

DISTINCTION "CUM LAUDE"

Alcalá de Henares, 20 de noviembre de 2018
EL VICERRECTOR DE INVESTIGACIÓN Y TRANSFERENCIA
THE VICE PRESIDENT FOR RESEARCH AND TRANSFER

F. Javier de la Mata de la Mata

DOCTORANDO (*Doctoral Student***):** YUAN, LEI
Copia por e-mail a (e-mail to):
DIRECTOR/A DE LA TESIS (*DIRECTOR OF THE THESIS***):** YUAN, YANG

Universidad de Alcalá

ESCUELA DE DOCTORADO.
Servicio de Estudios Oficiales de Posgrado

DILIGENCIA DE DEPÓSITO DE TESIS.

Comprobado que el expediente académico de D./Dª LEI YUAN

reúne los requisitos exigidos para la presentación de la Tesis, de acuerdo a la normativa vigente, y habiendo

presentado la misma en formato: ☒ soporte electrónico ☐ impreso en papel, para el depósito de la

misma, en el Servicio de Estudios Oficiales de Posgrado, con el nº de páginas: 146 se procede, con

fecha de hoy a registrar el depósito de la tesis.

Alcalá de Henares a 1 de OCTUBRE de 20 18

Aurora Juárez Abril

Fdo. El Funcionario

RESTAURAR   IMPRIMIR

Xi'an University of Technology

Faculty of Automation and Information Engineering

Program of Doctorate in Circuits and Systems

University of Alcala

School of Engineering

Program of Doctorate in Electronics
Advanced Electronic Systems, Intelligent Systems

Study on real-time track breakage detection system and signal processing

PhD Thesis

Author: Lei Yuan

Supervisors: Prof. Yuan Yang

Prof. Álvaro Hernández Alonso

2018

DEPARTAMENTO DE ELECTRÓNICA
Escuela Politécnica Superior
28805 Alcalá de Henares (Madrid)
Teléfonos: 91 885 65 40   Fax: 91 885 65 91
eldep@depeca.uah.es

Dr. Yuan Yang, Professor from the Xi'an University of Technology, and

Dr. Álvaro Hernández Alonso, Professor from the University of Alcala

INFORM: That the PhD thesis with title "Study on real-time track breakage detection system and signal processing", submitted by Ms. Lei Yuan, and carried out under our supervision, in the field of the **design of signal processing for safety systems in the detection of breakages in railway transport systems**, fulfils all the requirements about quality and originality to obtain the Degree of Doctor.

Xi'an / Alcalá de Henares, 20th October 2018.

Prof. Yuan Yang   Prof. Álvaro Hernández Alonso

Universidad de Alcalá

DEPARTAMENTO DE ELECTRÓNICA
Edificio Politécnico
Campus Universitario s/n
28805 Alcalá de Henares (Madrid)
Teléfono: 91 885 65 40
Fax: 91 885 65 91
Dpto.electronica@uah.es

Dr. D. Miguel González Herráez, coordinador del Programa de Doctorado "ELECTRÓNICA: Sistemas Electrónicos Avanzados. Sistemas Inteligentes".

INFORMA: Que la Tesis Doctoral titulada *"Study on real-time track breakage detection system and signal processing"* presentada por Dª. Lei Yuan y dirigida por los doctores Dª Yuan Yang y D. Álvaro Hernández Alonso, cumple con todos los requisitos científicos y metodológicos, para ser defendida ante un Tribunal para optar al Grado de Doctor, según lo indicado por la Comisión Académica del Programa de Doctorado.

Esta tesis se ha desarrollado en co-tutela internacional entre la Universidad de Alcalá y la Xi´An University of Technology, realizándose la defensa de la misma en esta última universidad.

Alcalá de Henares, 19 de octubre de 2018

Fdo. D. Miguel González Herráez

Abstract

As one of the lifeblood of national economic development, rail transportation carries heavy passenger and cargo tasks. Rail line is an important part of railway transportation. The accident losses caused by track breakage cannot be estimated. Its integrity affects the safety of people's lives and property. Real-time, accurate and stable fault detection is of great significance. The breakage detection is realized by analyzing and processing the signals transmitted in the track. Therefore, it is of great significance to study the denoising of signals in the breakage detection system and improve the signal recognition algorithm.

Firstly, in order to overcome shortcomings of complex wavelet selection, mode mixing, et al. in the current ultrasonic guided wave (UGW) signal denoising algorithms, this work proposes the use of variational mode decomposition (VMD) algorithm to suppress the interference of UGW signals. Based on the denoised UGW signal, a feature extraction method based on the UGW signal under different track status is proposed. The differences between the extracted features (the root mean square voltage value V_{rms} and the frequency component F_p corresponding to the highest amplitude point in the amplitude-frequency characteristics) in three different track states and their respective temporal and spatial dependencies are proposed. The idea of real-time identification and classification of track states by the recurrent neural network (RNN) is also proposed. Through the simulation and experimental results of denoising algorithm, the UGW signal can be reconstructed correctly, the extracted features are obviously different in three track conditions, and through the accuracy of the classification results and the display on the two-dimensional plane, it can be known that the RNN network can detect the track state in real time and discover the track breakage situation over time.

Secondly, aiming at the situation that the UGW signal cannot propagate through the joint maintenance of broken repaired structure, the previous UGW-based track breakage detection system cannot work anymore, the improved real-time track breakage detection system combined with the detection principle of the track circuit is proposed. The improved system is compatible with the transmission and processing of UGW and electrical signals, and is suitable for more complex train operating environments. At the same time, for the part of the improved track breakage detection system based on the principle of track circuit detection, two simulation models of railway line are proposed. These two models provide a suitable simulation platform for analyzing the transmission and detection of electrical signals.

Again, for the part of the improved track-breakage detection system based on the principle of the track circuit, the idea of direct sequence spread spectrum communication is used, and the

spread spectrum sequence has the characteristics of higher auto-correlation function peak and lower cross-correlation side lobes, which is proposed to be transmitted. The transmitter modulates the carrier signal by using a spread spectrum sequence, and obtains a new transmission mode by demodulation and correlation processing at the receiver end. In order to determine the spread spectrum sequence used in the transmission mode, the concept of correlation bound is proposed. Under different signal-to-noise ratio and the soil water content, signal transmission and interference tests are simulated by using track models. 63-bit Kasami sequences are adopted to modulate 125Hz sine signal, and the proposed electrical signal transmission method has better ability to resist noise and multipath interference.

Last, in order to correctly identify the signals transmitted by the new transmission method, a novel adaptive peak detection algorithm based on wavelet transform (WT) and Hilbert transform (HT) is proposed. The correctness and reliability of the proposed transmission method and adaptive peak detection algorithm are verified by different track states and signal transmission experiments under different noise conditions.

Note that when the improved real-time track breakage detection system is working, the UGW signal is mainly used, and the electrical signal is complementary

. The improved track breakage detection system is stable and reliable, and can determine the track status information of the detected section in real time, and timely deal with the broken track to ensure driving safety.

Key words: track breakage detection; ultrasonic guided wave (UGW); recurrent neural network (RNN); track circuit; Kasami sequence; adaptive peak detection

To my parents,
to my supervisors,
to everyone who gave me a lot of support

Acknowledgement

The life of my Ph.D study is coming to the end. Looking back on my four years of research, they are full of laugh, tear, achievement and growth. Experienced the frustration by the rejection of the paper, the failure of the experiment, fortunately, there is always the care of my parents, the care and support of the supervisors, and the encouragement of friends. As the thesis will be completed, I would like to express my gratitude to my supervisors and all the people who accompanied me on the trip of scientific research.

First of all, I would like to thank my supervisors, Prof. Yuan Yang in Xi'an University of Technology and Prof. Álvaro Hernández Alonso in University of Alcala. I could not easily pass through every critical step of my Ph.D., research topic selection, route planning, and problem research, without the careful guidance of them. Their spirit of dedicated to researches have an enormous impact on me. Every time when I want to give up, the suggestions about how to coordinate and handle various problems are proposed by them. I am grateful to Prof. Yang and Álvaro for guiding me to open the door for scientific research, for setting an example of independence, coordination and dedication to me. All these spirits guided me to continue firmly on the road of scientific research.

Secondly, I would like to thank Prof. Álvaro again. With his help, I can quickly overcome the helplessness of the abroad life and dedicated in scientific research. Under his guidance, my English writing level has been gradually improved, and my oral expression ability has become increasingly fluent. The successful completion of the thesis is inseparable from the guidance and help of Prof. Jesús Ureña, Juan Jesús, María Carmen and Felipe Espinosa.

Once again, I would like to thank the members of research group in Xi'an University of Technology, the Ph.D Xiaoyuan Wei, Ph.D Mingjing Zhai, and the Master Guotao Du, Jiaxu Wang, Juan Wang, Lin Shi, Fu Chen, Gengyi Zhang, Xiaobing Dang, Yuan Li, Xiaochao Ding, Xingfeng Du and other master students who help me in my theoretical research and experimental testing. In particular, Shi Lin gave me a powerful help during the construction of hardware platform and the experiment. I am grateful to Post Dr. David, Dr. Pablo, Dr. José, Dr. Teo, as well as all the members of the research team in University of Alcala for giving me both academic and life support during my stay period in Spain, which has enriched my days of studying in a foreign country.

Special thanks to my parents for giving me understanding and support during my Ph.D. period. It is with their love that I can complete the academic tasks of the doctoral period without any problems, and be able to retrieve the state as soon as possible when I´m feeling down.

In addition, thanks to all the editors and reviewers in the submission of the papers, it is these comments and suggestions that will enable me to continually revise the research route and improve the quality of the work.

Finally, I would like to thank the experts and professors who took the time to review my thesis!

Contents

Index of Figures

1. Introduction

2. Related Basic Knowledge Introduction of Track Breakage Detection System

3. Study on the Denoising and Track Status Recognition Algorithms of UGW Signal

5. Electrical Signal Transmission and Detection Algorithm for the Improved System

Index of Tables

3. Study on the Denoising and Track Status Recognition Algorithms of UGW Signal

5. Electrical Signal Transmission and Detection Algorithm for the Improved System

List of Symbols

Name	Description
$\oplus$	Operation of module 2 addition
$*$	Operation of convolution
F_t	Forgot gate
W_f	Weight matrix of the forgot gate
h_t	Current output value of LSTM.
i_t	Input value of the current network
b_f	Bias term of the forget gate,
σ	Sigmoid function.
I_t	Input gate,
W_i	Weight matrix of the input gate
b_i	Bias term of the input gate
$\tilde{c}_t$	Current input state
tanh	Hyperbolic tangent function
W_c	Weight matrix of the cell state
b_c	Bias term of the cell state
c_t	Cell state
O_t	Output gate
W_o	Weight matrix of the output gate
b_o	Bias term of the output gate
$p(j|i)$	Conditional probability
σ_i	Variance of the Gauss distribution
C	Loss function
q_{ij}	Joint probability of low-dimensional space
p_{ij}	Joint probability of high-dimensional space
R_a	Rate of information
g_n	Gate function.
R_c	Rate of the pseudo-random code
$g_c(t)$	Gate function of the pseudo-random code
$d(t)$	The extended sequence
f_0	Carrier frequency
$n(t)$	Channel noise
$J(t)$	Interference signal

Name	Description
$s_J(t)$	Spread spectrum signal from other networks
$(\boldsymbol{a}, \boldsymbol{b})$	A complementary sequence pair
$R_a(\tau)$	Aperiodic auto-correlation functions of sequence $\boldsymbol{a}$
$R_b(\tau)$	Aperiodic auto-correlation functions of sequence $\boldsymbol{b}$
Δ	A random time
$R_{\mathrm{ACF}}(\tau)$	Auto-correlation function
τ_w	Window size of interference free window
$R_{\mathrm{CCF}}(\tau)$	Cross-correlation function
L_0	Length of complementary sequence
W_0	Number of 0 inserted in the middle of LS code
$LS(L_0, L, W_0)$	LS code with the length of L
$\phi_{l,M}$	Lower bound of cross-correlation
$\mathbf{u}$	A binary sequence of length L
$\mathbf{w}$	A sequence of sampling intervals of $2^{n/2}+1$ for $\mathbf{u}$
T_m	Left shift operator
m	Shift parameter of the sequence $\mathbf{w}$
$K_s(\mathbf{u}, n, m)$	Small set of Kasami sequence derived from $\mathbf{u}$
M	Number of sequences obtained in a small set of Kasami sequence
$Kas(n, M, L)$	Kasami sequence with the length of L
$h(t)$	Cauchy kernel
$p.v.$	Cauchy principal value
$H[\ ]$	Result of HT
$H(j\omega)$	Fourier transform of $h(t)$
$\mathrm{sgn}(\omega)$	Sign function
$\mathrm{DWT}_{a,b}$	Discrete wavelet transform with scale factor a, and offset parameter b
$\psi_{j,k}(\ )$	A wavelet function
$A[\ ]$	Approximate part of each level in DWT
$D[\ ]$	Detailed part of each level in DWT
s_{UGW}	Ideal UGW signal
β	Amplitude of UGW signal
∂	A positive constant which determines the UGW bandwidth
f_c	Center frequency of UGW signal
φ	Initial phase of the UGW signal
s_{R}	Actual received UGW signal

Name	Description
n_{UGW}	Noise containing in UGW signal
$u_k(t)$	Intrinsic mode function
∂_t	Partial derivative of function to time t
$\delta(t)$	Unit impulse function
j	Imaginary unit
$\zeta(\ )$	Augmented Lagrangian function
α	Quadratic penalty term
$\lambda(t)$	Lagrangian multiplier
$\hat{u}_k^{n+1}(\omega)$	Minimum value of IMF u_k
ω_k	Minimum value of center frequency
τ	Updating parameters
$\tilde{s}_{\mathrm{UGW}}$	Sum of all IMF components
P_s	Average energy of signal
P_n	Average energy of the noise
V_{rms}	RMS value
F_p	Frequency corresponding to the peak value of the spectrum signal
R	Resistant
L	Inductance
C	Leakage capacitance between two tracks
G	Leakage conductance between two tracks
R_c	Resistant of cable
L_c	Inductance of cable
C_c	Capacitance of cable
C_{trans}	Capacitances of transformer
R_t	Resistant of track
L_t	Inductance of track
C_t	Capacitance of track
G_t	Conductance of track
R_{t100}	Resistance of 100m track section
L_{t100}	Inductance of 100m track section
G_{t100}	Conductance of 100m track section
C_{t100}	Capacitance of 100m track section
ρ	Ground conductance
W	Dimensionless water content

Name	Description
ε	Ground permittivity
G_{ground}	Conductance of ground
C_{ground}	Capacitance of ground
$e[k]$	Modulated signal
$c[k]$	Binary sequence used to encode the emission
$p[k]$	A modulation symbol with P samples per period
$d[k]$	Demodulated signal
$r[k]$	Received signal
$t[k]$	Correlation output
θ_{AC}	AC bound
θ_{CC}	CC bound
θ	Global bound
$C_{ap,ap}$	AC function for certain test conditions
$C_{np,np}[0]$	AC main lobe under ideal conditions
$s[k]$	Squared signal
$m[k]$	Averaged signal
$n[k]$	Normalized signal
$DW_{ACF}[k]$	Reconstructed ACF signal

List of Abbreviation

ACF	Auto-correlation functions
ADC	Analog to Digital Converter
AI	Artificial Intelligence
AM-FM	Amplitude Modulated-Frequency Modulated
ANN	Artificial Neural Network
ARM	Advanced RISC Machines
BPSK	Binary Phase Shift Keying
BPTT	Back Propagation Through Time
CBTC	Communication Based Train Control
CCF	Cross-Correlation Function
CWR	Continuous Welded Rail
CWT	Continuous Wavelet Transform
DAC	Digital to Analog Converter
dB	Decibel
db2	Second-order Daubechies Wavelet
DC	Direct Current
DS-SS	Direct Sequence Spread Spectrum
DW	Discrete Wavelet Transform
EEMD	Ensemble Empirical Mode Decomposition
EMD	Empirical Mode Decomposition
FFT	Fast Fourier Transform
GPRS	General Packet Radio Service
HT	Hilbert Transform
ID	Identification
IFW	Interference Free Window
IMF	Intrinsic Mode Function
ISI	Inter-Symbol Interference
KL	Kullback-Leibler
LS	Loosely Synchronous
LSTM	Long Short-Term Memory
MA	Moving Average
MAI	Multiple Access Interference

MCU	Microcontroller Unit
MOSFET	Metal-Oxide-Semiconductor Field-Effect Transistor
PN	Pseudo-Noise
RMS	Root Mean Square
RNN	Recurrent Neural Network
SGD	Stochastic Gradient Descent
SNE	Stochastic Neighbor Embedding
SNR	Signal to Noise Ratio
SPUT	Sandwich Piezoelectric Ultrasonic Transducer
SS	Spread Spectrum
STFT	Short Time Fourier Transform
t-SNE	t-Distributed Stochastic Neighbor Embedding
UGW	Ultrasonic Guided Wave
VMD	Variational Mode Decomposition
WT	Wavelet Transform
ZFFT	Zoom Fast Fourier Transform

1 Introduction

1.1 Research Significance of Track Breakage Detection

Since Shaoshan-8 became the first high-speed train in China in January 1997 at a speed of 240 km/h, China's railway technology has been developing continuously. The new Qinhuangdao-Shenyang high-speed railway line in October 2003 marked that China's railway has been officially stepping into the rapid development [1]. In August 2008, the Beijing-Tianjin intercity railway line, China's first high-speed railway with full independent intellectual property rights and a speed of 350 km/h, was open to traffic. By the end of 2012, the total revenue kilometers of China's high-speed railway had reached 9,356 km. By 2015, the operating mileage of China's high-speed railway line had exceeded 18,000 km [2]. With the rapid growth of China's economy and the steady progress of the construction of "The Belt and Road", the railway transportation industry has achieved rapid development in recent years. Up to 2018, the operating mileage of the high-speed railway line has increased to 25 thousand km, accounting for 2/3 of the total operating mileage of the world's high-speed railway operation. Meanwhile, the high-speed railway and its related fields of major technological breakthroughs, also makes China's high-speed railway go abroad and serve the world [3].

As a vital part of railway construction, the function of the track is to provide continuous, smooth and rolling surface with minimal resistance for the wheels, guide the train wheels to travel, withstand the tremendous pressure brought by the train running and transfer the pressure to the sleeper. For automatic block or electrified section, the track also acts as part of the track circuit to transmit the electrical signals [4]. The standard railway lines usually use joint bars to connect and fasten the tracks with the standard length of 12.5m and 25m together. With the gradual expansion of the laying scope of high-speed railways, continuous welded rails (CWR) are increasingly applied to high-speed railways to eliminate the impact force of joints caused by the use of joint bars, reduce the damage of the railway line, save raw materials, improve train speed, and increase the smoothness, stableness and intimacy for passengers [5]. The CWR has its corresponding advantages, meanwhile, it faces new problems and challenges. As the seasonal temperature changes, the CWR bears the temperature force generated by thermal expansion and contraction. When tracks temperature changes by 1°C, it will bear 1.654 tons of pressure or tension [6]. In China, there are some areas with large temperature difference between day and night, the working tracks in the outdoor often bear the pressure or tension caused by thermal expansion and contraction for a long time. In addition, the pressure generated by the rolling

compaction while train is running, makes the breakage occurs in CWR, especially at the welded joint of the CWR. Frequently happened natural disasters and some man-made damages are also the factors leading to the widespread distribution, numerous types and frequent occurrence of disasters on railway lines [7]. Presently, the sections where the disaster once took place exceed 20% of the total operating mileage, resulting in more than 100 interruptions on average in railway transportation annually, and there are still a large number of railway lines with potential disasters, which has a serious impact on train safety [8]. With the rapid development of railway construction in China, the safety requirements for train operation are becoming more and more rigorous. Especially for high-speed railway lines which with high speed and large density of train operation, and with the passenger transportation as its main task, the guarantee of running safety becomes especially important [9-10]. Though the obstacles in railway also effect the running safety [11-13], this work mainly focus on the problem of track breakage, Fig. 1-1 is an example of a broken rail.

Fig. 1-1 An example of track breakage

Once the track breakage occurs, the monitoring center must be able to detect the situation in real time and take corresponding measures to prevent the train from entering the section where the track has broken. If the situation cannot be disposed in time, it may lead to train derailment and rollover accident, ranging from economic losses to serious casualties.

Accidents caused by track breakage occur all over the world. Before the dawn on December 19th 2004, ten trains were delayed caused by frost cracks of the track at the crossing of Fatasi in Beijing due to frost weather for several days. On December 19th 2007, a running train in Pakistan suddenly derailed, resulting in 58 deaths and more than 120 injuries, which was caused by the sudden expansion of crack resulting in track breakage. On April 28th 2008, the train T195 from Beijing to Qingdao was off the line at the section of Zhouwang village due to track breakage, causing the collision with the train No. 5034 from Yantai to Xuzhou, and resulting in 70 deaths and 247 injuries. On November 14th 2014, two trains in Caston of the United States, derailed due to track breakage, resulting in a large number of infrastructure damage. When train No. 3707 in Taiwan passed the location of 305 kilometer of Dongzheng Line from Jiayi to Nanjing On April 19th 2015, the left side of the railway line was found to have fractured about 10 cm. The fracture

was later verified to be caused by the rapid fatigue aging of the track. Due to timely discovery, the fracture did not cause any accident [14].

It is of great significance to conduct the detection of the track breakage with real-time, small false alarm rate, low environmental impact, low cost and remote access and control to track status.

1.2   Research Status at Home and Abroad

1.2.1 Research Status of Track Breakage Detection Technology

In order to prevent track breakage accidents, experts and scholars at home and abroad continue to explore new equipment and methods for track breakage detection, making track breakage detection more convenient, efficient and reliable. At present, the main methods of detecting broken track in the world are:

(1) Detection method of off-line manual track detection vehicle

The off-line manual track detection vehicle was researched and developed by Chinese researchers on the basis of the resonant ultrasonic breakage detector produced by MATISA company in Switzerland, which usually has three kinds of probes based on ultrasonic detection technology. Among them, the 0° probe is used to detect horizontal and longitudinal cracks at all parts of the track, the 37° probe is used to detect transverse cracks and internal flaws at the bottom of the track, and the 70°probe is used to detect flaws at the track head, cracks at the track waist, bubbles, ballasts and cracks at welds. When the off-line manual track detection vehicle is working, the probe converts the electrical signals into ultrasonic signals and sends them to the track under test. The track breakage will be determined according to the ultrasonic echo signals received and shown in the displayer. The method has the advantages of high flexibility, low cost and strong stability with multi-channel operation. However, off-line detection limits it to work only in the free period of the railway line, and the slow detection speed leads to long track occupation time. The detection method has brought about heavy workload to workers, which cannot be used conveniently in atrocious weather. The outdoor operation of off-line manual track detection vehicle is shown in Fig. 1-2 [15].

Fig. 1-2 Diagram of off-line manual track detection vehicle

(2) Detection method of double tracks ultrasonic detection vehicle

Compared with the off-line manual track detection vehicle, the double tracks ultrasonic detection vehicle can not only detect two rails at the same time, but also provide seats for the operators, so as to lower the workload of operation workers. Its detection principle is basically as same as the off-line manual track detection vehicle, which uses ultrasonic echo characteristics to determine the track breakage. This vehicle is driven by batteries, the detection speed can be maintained at 10 km / h approximately, and the test results can be stored, replayed and queried. The shape and structure of the vehicle is shown in Fig. 1-3 [16-17].

Fig. 1-3 Double tracks ultrasonic detection vehicle

The double tracks ultrasonic detection vehicle has high detection rate, working efficiency and sensitivity, and is currently promoted and applied. However, since it is battery-driven, the continuous operation time is relatively short, and it can only work in the free period of the railway line. Its weight is more than 200 kg, once in the detection process there encounters an emergency in which a train needs to pass, more people are needed to remove it [18].

(3) Detection method of large-scale track breakage detection vehicle

The technology of using large-scale track breakage detection vehicle for flaw detection and track breakage detection has been quite mature in the developed regions and countries such as Europe and America. The ultrasonic probe is fixed on the wheel of this type of vehicle. During the operation, the ultrasonic probe emits ultrasonic beam to the track and collects the echo signals reflected by the track. Many sensors are connected with the internal detection instrument of the vehicle. Finally, the echo signals are analyzed by the instruments in the control room to detect whether the track is broken or not, which has the advantages of fast detection speed and strong resistance to interference. The large-scale track breakage detection vehicle usually works in a standstill mode, i.e. the inspection section will be closed during the breakage detection process. When the damage, cluster damage or track breakage is found, it can confirm immediately and arrange the subsequent repair work [19]. Fig. 1-4 shows a large-scale track breakage detection vehicle manufactured by Swiss SPENO company.

Fig. 1-4 Large-scale track breakage detection vehicle produced by SPENO company

At present, the large-scale track breakage detection vehicle developed by China can achieve the highest detection speed of 107km/h. Although the speed of the detection method is faster, it is still off-line and can only work in the free period of the railway line, together with the expensive construction cost, relatively high cost of repair and maintenance, the severe mismatching between the quantity on-hand and quality demanded and its high requirement on the cleanliness of the track surface. In view of the heavy task of railway transportation in China, the free periods of the railway line are less and the duration is shorter. Many lines cannot be patrolled by large-scale track breakage detection vehicle, and the flexibility is poor [20].

(4) Real -time optical fiber track breakage detection method

Real -time optical fiber track breakage detection method uses special epoxy glue to attach the standard single-mode optical fiber firmly to the track waist in parallel with the ground. Light emitter (i.e. light source) and optical receiver are respectively placed at both ends of the optical fiber and Fig. 1-5 is the basic schematic diagram of this detection method. Normally, the light generated by the light source transmits through the optical fiber to the optical receiver. Once the track breaks, the optical fiber tightly attached to it will also break. The optical signal cannot continue to transmit normally, and the detection equipment cannot receive effective signal and send out the track breakage alarm information. This method has high accuracy and reliability, which can not only detect track breakage, but also detect the track deformation, as well as can help the monitoring center to deal with early hidden dangers in time. Moreover, this method will not be affected by the parameters of ballast and environment, and the principle of implementation is relatively simple. However, due to the fragile material of the optical fiber itself, it is easy to break in the installation process. Meanwhile, it is a necessity to ensure that the surface of its installation environment is smooth, without any rust and pollutant. The optical fiber should be sheared off at the joint between the turnout and track, and need to be bypassed by using the bridge connector. Therefore, as far as the actual situation of railway lines in China, such careful installation and detection method is not suitable for long-distance track detection [21-25].
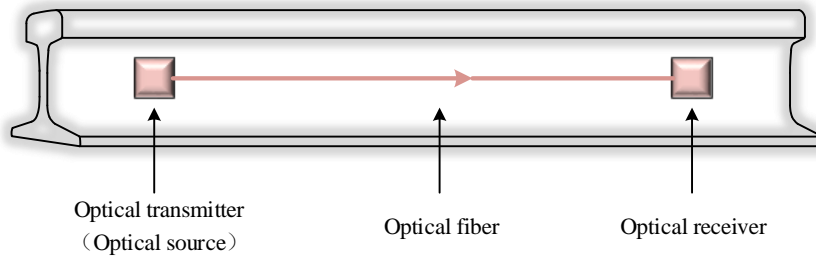
Fig. 1-5 Diagram of real-time track breakage detection method by optical fiber

(5)   Detection method based on ultrasonic guide wave

Ultrasound guided wave (UGW) is generated when ultrasonic wave is confined within the boundary of rod-like or tubular waveguide medium, where the ultrasonic wave repeatedly reflects. Compared with ultrasonic wave, UGW detection provides relatively low detection frequency and longer transmission and detection distance. By exactly taking advantage of feature that the track is a good waveguide medium, the UGW signal transmitting along the track can be obtained by the continuous reflection of ultrasonic wave on the track boundary surface. The guided wave attenuates less when transmitting in the track and can maintain the original signal character after long-distance transmission, which consequently fits long-distance track breakage detection. For these reasons, UGW track breakage detection method is able to be proposed and developed [26-34] and Fig. 1-6 is the basic structure of UGW-based track breakage detection system.
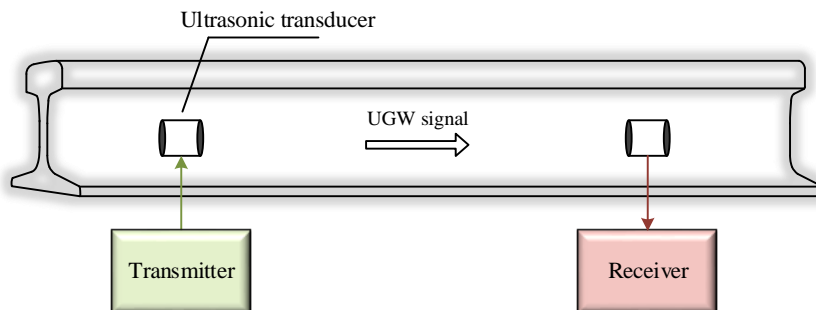
Fig. 1-6 The diagram of track breakage detection method based on UGW

As can be seen from Fig. 1-6, transmitting and receiving equipment are installed at both ends of the detection section, which are connected to the track by ultrasonic transducers installed on the track waist. The transmitter triggers the ultrasonic transducer to produce UGW signals, which transmit along the track to the receiver end and are converted into electrical signals by the ultrasonic transducer to the receiving equipment. If the track does not break in the detection section, the receiver will collect and recognize the correct UGW signal. Once the track breaks in the detection section, the energy of UGW signal will greatly attenuate, and the receiver can judge the track breakage according to the algorithm processing. UGW is a mechanical wave, which is almost not affected by electromagnetic and ballast parameters, and its energy conversion efficiency is comparatively high [35-36]. However, although CWR abandons the use of joint bar as

the connecting fixture, joint bar is selected and used to connect the two ends of the gap caused by the breakage. The maintenance structure of track breakage is shown in Fig. 1-7.
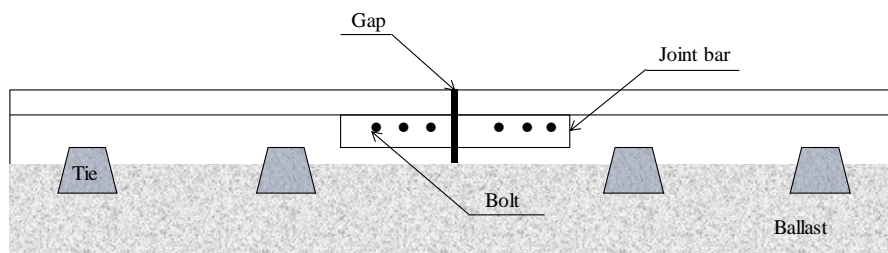
Fig. 1-7 The maintenance structure for breakage

After the broken track is connected and repaired, UGW signal will attenuate tremendously while transmitting in the air, thus when it passes through the repaired structure great attenuation will generate and the detection method based on UGW signal cannot continue to be used normally. In addition, the use of the repaired structure is uncertain in space and time, leading to the use of UGW signal in the repaired structure cannot continue to detect rail breakage within the existing time bucket, which will seriously limit the application and promotion of UGW rail breakage detection method through engineering approaches.

(6) Detection method based on track circuit

Track circuit is a circuit composed of railway line and insulation, which is used to supervise the operation line (free, occupied, or broken), and link the signal display with the train operation condition, so as to realize the control of train operation condition [37-41]. The track acts as the transmission conductor of the electrical signal in the track circuit. The electrical signal generated by the transmitter can transmit to the receiver through the track. In the receiver, the signal relay is usually used to receive the signal current. When the track in the detection section is complete and without train occupancy, the signal relay energized and indicates the free condition; when a train passes through the detection section, the relay drops down since the train's wheelset resistance is far less than the relay coil resistance; if the track in the section is broken, the electrical signal cannot continue to transmit, the whole track circuit system cannot form the current loop, resulting in no current flow on the signal relay. At the time, the relay drops down, the alarm light turns on, and the train is forbidden to enter the corresponding section [42]. Fig. 1-8 shows the basic principle of track breakage detection by using track circuit. It is very expensive to use track circuit alone for breakage detection, and the detection result is easily affected by the factors such as environment, ballast and electromagnetism and so on.

In addition to the six track breakage detection methods mentioned above, there are also unbalanced traction current detection method [43], electromagnetic detection method [44], optical image detection method [45], etc.
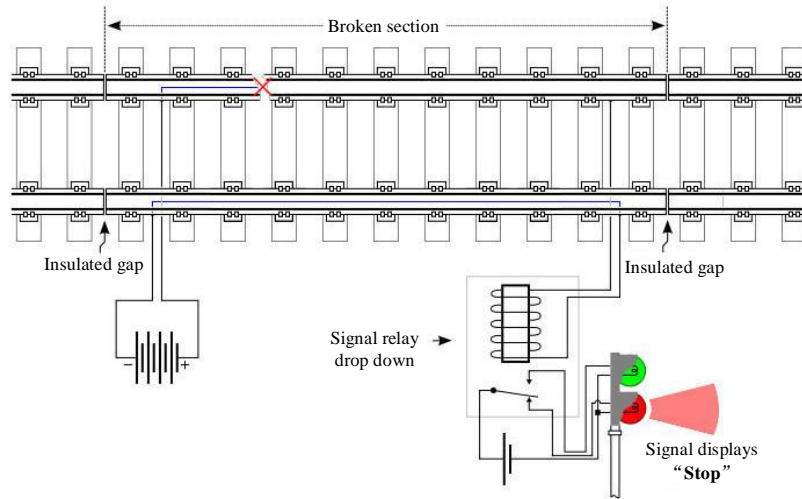
Fig. 1-8 The diagram of track breakage detection based on track circuit

1.2.2 Research Status of UGW Signal Processing Algorithm

Presently, the analytical method is mostly used in UGW signal research by applying the finite element or semi-analytical finite element method to research on the dispersion curve and wave characteristics of UGW signal transmission [46-49]. The number of projects using signal processing method to denoise and recognize the received UGW signal is relatively less. As the transmission medium of UGW signal, track is exposed to the complex outdoor environment for a long time, and interference will be inevitably introduced in the transmission process. Therefore, in order to improve the sensitivity and accuracy of the detection system, it is necessary to process the received signal by algorithm.

J.L.Rose took advantage of the characteristics of the generation of impulse echo when UGW signals encounter track defects or breakage, and proposed to identify the track breakage according to the echo intensity [50]. This method can identify the damaged parts such as track head, waist or bottom according to the echo characteristics, and determine the distance between the damaged parts and the transmitter end. However, in the process of UGW signal transmission, the energy of itself will attenuate whenever there is any damage. One part will return to the transmitter in the form of echo, the other part will continue to transmit along the track in the form of transmission waveform. The amplitude of the echo signal is relatively small and difficult to be recognized. Therefore, the method is limited to short-distance usage.

O.R.Gericke first puts forward the application of spectrum analysis technology to detect ultrasonic signals [51-52]. However, the actual UGW signal is usually not a regular stable signal, which may contain noise signal which has the similar frequencies with useful signals. Therefore, spectrum analysis and general filtering processing method often filter out useful signals while filtering out noise, resulting in the error detection of UGW signal.

As a widely used time-frequency analysis method, short-time Fourier transform (STFT) can be used in the detection of UGW, such as signal denoising, wave-packet separation for multi-modal and determination of dispersion characteristic curve. Kwun et al. uses STFT to study the dispersion characteristics of UGW signals in long-distance liquid-filled pipes, and determines the guided wave modes in the signals [53]. Xiangming Zheng and Marc et al. have proved that the STFT method can be used for multimodal separation of ultrasonic Lamb waves [54]. In this method, the window function is used to analyze the signal, usually, narrow window is used to improve the time resolution and it is adopted for fast-changing signal; while wide window is used to improve the frequency resolution and it is used to process the slow-changing signal. However, for the non-stationary UGW signal, which changes sometimes fast and sometimes slow, the application of windowing method highlights its contradiction between the time domain and frequency domain resolution.

Wavelet Transform (WT) can automatically change the resolution of time and frequency according to the frequency of the analyzed signal. Wavelet filter can also automatically change the width of frequency band according to the frequency of the signal. Therefore, this method overcomes the shortcomings of STFT and has been well applied in UGW signal processing. The application of WT in guided wave analysis is mainly to analyze the transmission of guided wave in dispersion medium; to study the circular transmission of guided wave in the case of axial crack on the outer surface of steel tube; when detecting the defects of steel tube by using guided wave, the multi-scale WT is used to denoise and extract the defect echo signal; and the threshold denoising method based on WT is used to process the UGW signal transmitted in the rail [55-57]. Although compared with the general time-frequency analysis method, WT has many advantages, there are still some deficiencies, for instance the choice of wavelet basis function is more complex, finite wavelet basis will cause the leakage of signal energy, the meaningless false components will be generated in the analysis of non-linear, non-stationary UGW signal.

Intrinsic Mode Function (IMF) is an Amplitude Modulated-Frequency Modulated (AM-FM) signal. A multi-component signal $s(t)$ can be decomposed into the sum of several IMFs and a residual signal [58-59]. Empirical Mode Decomposition (EMD) algorithm can adaptively decompose complex signal into a series of IMF components, and the frequencies of these components distribute from high to low. The IMF component decomposed by EMD algorithm is closely related to the original signal itself. It is adaptively decomposed based on the original signal data and does not need to pre-select the wavelet basis function like WT method. But it also has its own shortcomings, mainly reflect in the decomposition of the components with the similar frequencies into the identical IMF when the noise signal is being processed. The phenomenon that the appearing of originally different modes on the identical IMF caused by the failure of

effectively separating the IMFs according to the time scale is called mode mixing, which leads to the loss of original purpose and significance of EMD algorithm [60-61].

In order to solve the problem of mode mixing, Wu et al. decomposed the signals which repeatedly overlapping the finite amplitude Gaussian white noise by using EMD algorithm, and proposed Ensemble Empirical Mode Decomposition (EEMD) algorithm [62]. The average values of each IMF decomposed by EMD algorithm are treated as the actual IMF of EEMD, which does not only solve the problem of mode mixing, but also suppress the flying wing phenomenon at the boundary point caused by too few extreme points, correctly separating the mode signals without any prior knowledge. References [63] and [64] use the EEMD algorithm to suppress the interference of medical ultrasound images. Although EEMD effectively solves the problem of mode mixing, the reconstructed signal obtained by this algorithm contains the noise which has not be eliminated after ensemble averaging. The reconstructed signal cannot accurately represent the original signal, that means EEMD algorithm cannot accurately recover the original signal.

With the rapid development of artificial intelligence (AI), artificial neural network (ANN) is gradually applied to UGW nondestructive testing technology. At present, the commonly used training algorithm is the Back Propagation (BP) algorithm. Chen, Zhenqing Liu and others use neural network algorithm to classify the defects in their respective researches [65]. Sylvie and Solis use wavelet analysis to extract the characteristics of time-domain UGW signals. On the basis of obtaining a large number of samples, ANN is used to classify the solder joints [66-67].

1.2.3 Research Status of Track Circuit-based Track Breakage Detection

Track breakage detection of railway line is initially realized by track circuit, but the basic function of track circuit is to reflect whether the track is occupied by the train or not, and breakage detection is only an assistant function. With the development of high-speed railway, communication technology has been widely used in train control system, the function of track circuit has weakened. At the same time, the track circuit can only detect the complete disconnection of the track, the phenomenon of track cracks cannot be truly detected. Therefore, the research on track breakage detection based on track circuit principle is relatively less currently, and the representative detection technologies are [68]:

(1) Using the unbalanced traction current to detect the track breakage. This method is based on the principle of the generation of larger unbalanced traction current after the track broken. The main advantage of the method is that the circuit structure is simple, only by short connecting conductor and installing sensors. This method takes advantage of the traction return current and without any signal source. However, it also has some deficiencies, such as the complex path and distribution of the traction current, the low accuracy of the calculation model of the traction

current, and not timely train braking caused by its failure to detect only until the train drives into the track circuit section and the traction current flows through the rail.

(2) Using the balance degree of the excitation source to detect the broken track. The method overcomes the defect that only when the train drives into the track circuit section and the traction current flows through the two tracks can it detect the track breakage. However, due to the existence of the leakage impedance in the ballast bed, this method is insensitive to the track breakage detection at the end of the track, thus lead to the installation of mechanical insulated gap between the adjacent two sections.

(3) Communication based train control (CBTC) system. This method will short the two ends of the detection section, set the signal transmitting equipment in the middle of the detection section, and add the "8" shaped coupling induction coil in this closed section, to determine whether the track breaks or not by detecting the induced electromotive force. This method can realize the whole track breakage detection; cannot require mechanical insulated gap and can be directly insulated by short-connected conductors; overcome the impact of traction current on current sensors. However, this method cannot distinguish which side of the power supply and which track is broken.

Although the track breakage detection method based on track circuit principle has poor sensitivity and reliability in special sections such as turnout and guard rail part. The basic theory and technology involved in track circuit are more extensive and mature, the track breakage technology based on track circuit principle has the advantages of simply structured equipment and easily to be realized.

At present, there are few papers on signal processing of track circuits, mainly focusing on the root mean square (RMS) calculation of the transmitted voltage or current signals [69]; extracting characteristic frequencies of signals by Fast Fourier Transform (FFT) and refining the local frequency bands of interest in the signal spectrum to improve the spectral resolution by Zoom Fast Fourier Transform (ZFFT) algorithm, thereby improving the reliability of track circuit signal detection [70].

In addition, there is work to detect the track section broken by setting a threshold to detect the peak value of the voltage signal at the receiving end. However, the signal recognition method relying on the fixed threshold may cause the leakage and redundant detection of the peak value in some cases, reducing the detection efficiency [71]. In order to solve this problem, the method of detecting signal peak value based on dynamic threshold is proposed in the literature [72]. However, the updating process of dynamic threshold involves some empirical parameters and signal characteristic, which is not universal.

1.3   Research Content and Structure of the Thesis

1.3.1 Research Content

Aiming at the drawbacks of existing UGW signal denoising methods and the failure of UGW-based track breakage detection system when there is a breakage maintenance structure in the corresponding section, the following research has been conducted:

Firstly, in view of the fact that UGW signal will be affected by various environmental noises in the process of transmission and the effect of existing signal denoising algorithms is not ideal, this work introduces the Variational Modal Decomposition (VMD) algorithm to denoise UGW signal. The denoising effect is determined by simulation and experimental result, and the feature extraction will be conducted on denoised UGW signal in different track status. The difference of extracted features and the temporal and spatial dependencies among features are used to identify and classify the track status in real-time by using recurrent neural network (RNN).

Secondly, aiming at the problem that the UGW signal cannot propagate through the maintenance structure of the broken track normally, and the existing UGW-based track breakage detection system cannot continue to be used normally, on the basis of the existing detection equipment, this work proposes to add the electrical signal processing part based on the detection principle of the track circuit, so as to realize the improved track breakage detection system, which primarily base on UGW detection and is supplemented by the track circuit principle detection. Using the existing equipment and facilities, the cost of reconstruction and the difficulty of construction can be reduced. The two methods based on UGW and electrical signal can be compatible with each other in the installation mode and detection equipment, and can be switched to the other mode at any time, which can deal with the complex outdoor environmental conditions, so as to improve the detection rate of track breakage, and the simulation model of railway line for the proposed electrical signal transmission part is established.

Finally, in order to make the newly added electrical part realize a long-distance, strong resistance to interference, as well as stable and reliable transmission, a new transmission mode of electrical signal is proposed based on the idea of direct sequence spread spectrum (DS-SS). At the same time, in order to determine the characteristics of the code or sequence used, the concept of correlation bound is proposed. An adaptive peak detection algorithm based on Hilbert transform (HT) and WT is proposed.

By combining the detection results of UGW signal and electrical signal, the track status information of the area covered by the improved track breakage detection system can be obtained in real-time.

1.3.1 Structure of the Thesis

The thesis is divided into six chapters. The detailed content of each chapter is as follows:

Chapter 1 is the introduction part, expounding the significance and background of this work, emphatically introducing the updating of the corresponding signal detection algorithm during the development of UGW-based and track circuit principle-based track breakage detection technology. The research content of this work is summarized, and the content arrangement of each chapter is described in detail.

The Chapter 2 introduces the existing UGW-based track breakage detection system and the basic theoretical knowledge which will be used in the follow-up research.

In the Chapter 3, the methods of UGW signal denoising, feature extraction and track status recognition algorithm based on RNN are proposed. According to the simulation and experimental result, the algorithms proposed are verified.

Chapter 4 describes each part of the improved track breakage detection system in detail, and puts forward the simulation model for the newly added electrical detection part based on the principle of track circuit.

In the Chapter 5, based on the idea of DS-SS communication and the correlation of spread spectrum sequence, the transmission mode of electrical signal and the adaptive detection algorithm of electrical signal at the receiver in the improved track breakage detection system are proposed.

Chapter 6 is the summary and outlook, in which the research studied in this work is summarized and some ideas and plans for the future research is put forward.

2 Related Basic Knowledge Introduction of Track Breakage Detection System

In this chapter, the existing UGW-based track breakage detection system, as well as the basic concepts, theories and algorithms needed in the follow-up work of the thesis are briefly introduced.

2.1 UGW-based Track Breakage Detection System

The general overview of the existing track breakage detection system based on UGW signal is shown in Fig. 2-1. It includes a monitoring center and a set of nodes distributed along the railway line. Each node mainly involves a solar power supply system, a transmitter or a receiver (depending on the type of node), ultrasonic transducers, as well as a wireless communication module. The solar power supply system provides the power required by each node, and transmitters and receivers are placed alternately every 1km. Each transmitter or receiver is connected to the rail waist through two ultrasonic transducers (one per rail), again with a distance of 1km from each other. The rail segment between a transmitter and the following receiver is known as a track section. Through a wireless communication module based on General Packet Radio Service (GPRS), information collected by each track section can be sent to a remote monitoring center.
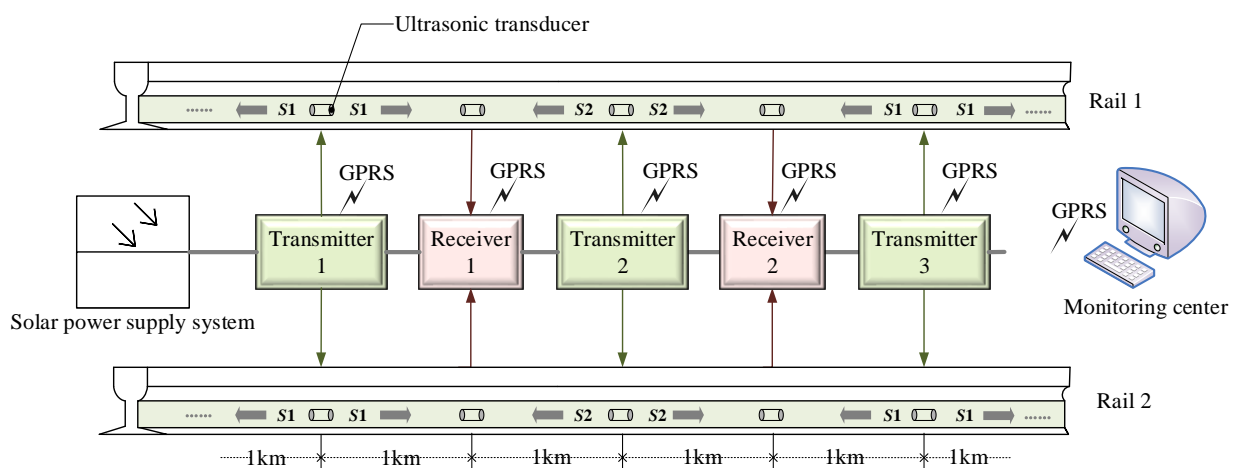
Fig. 2-1 Typical structure for the UGW-based track breakage detection system

The block diagram for the transmitter is shown in Fig. 2-2. The transmitter structures are denoted within the dotted box, where the available Advanced RISC Machines (ARM) core-board is in charge of generating the three sets of driving square signals at intervals of 3s or 1s every 1

minute. The interval between the three driving signals is 3s or 1s, depending on the odd and even number of the sending node. When it is the odd number, the interval is 3s; when it is the even number, the interval is 1s. Each control signal group has 30 square wave signals with amplitude of 3.3V and frequency of 30 kHz. The driving signal is shown in Fig. 2-3. Then, these driving signals are sent to two identical processing line to weaken the influence of the high voltage of the back stage on the front stage microcontroller unit (MCU) through the electromagnetic isolation of Adum1201 in first. These driving signals continue to pass through the Metal-Oxide-Semiconductor Field-Effect Transistor (MOSFET) driver, MOSFET and transformer. The ultrasonic transducer T_A is connected with Rail 1 and T_B is connected with Rail 2, which realize the conversion of electrical signal to ultrasonic signal, and then energize the rail to generate UGW signals. Under normal working conditions, all transmitters marked as odd number generate signal $S1$' to drive ultrasonic transducer T_A and T_B to send UGW signal $S1$ along the track to both sides simultaneously. After 30 seconds, all transmitters marked as even number generate signal $S2$' to drive T_A and T_B to send the UGW signal $S2$ to adjacent sections simultaneously in the same way. The driving signal $S1$' and $S2$' are shown in Fig. 2-4.
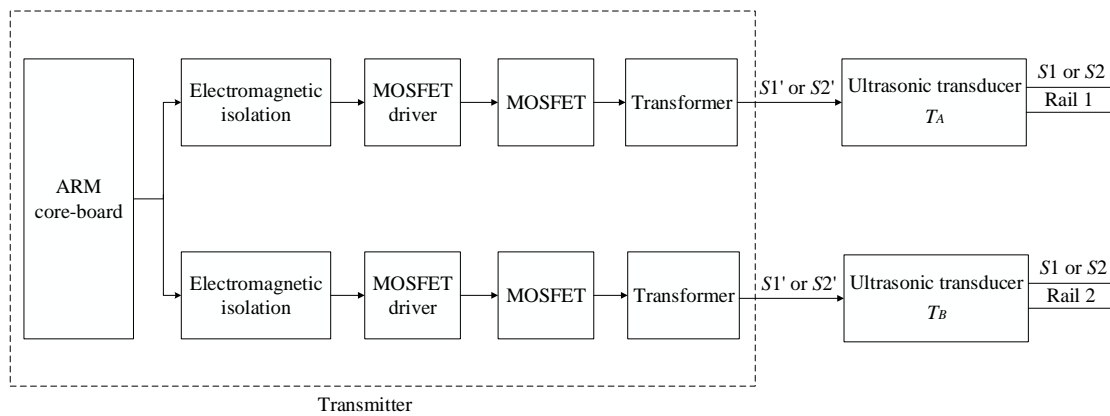
Fig. 2-2 Block diagram for the UGW transmitter
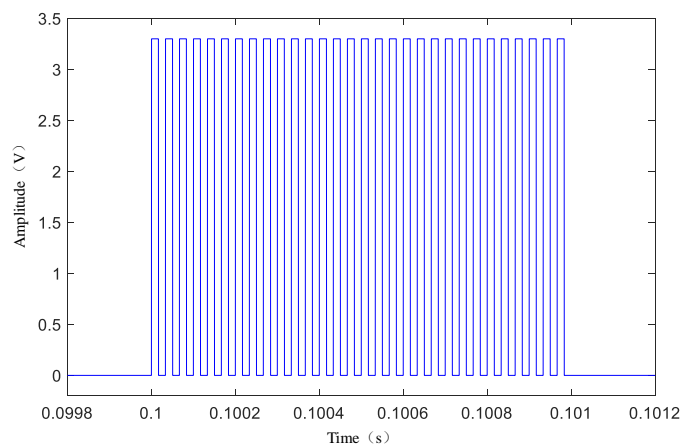
Fig. 2-3 Single group control signal generated by ARM core-board
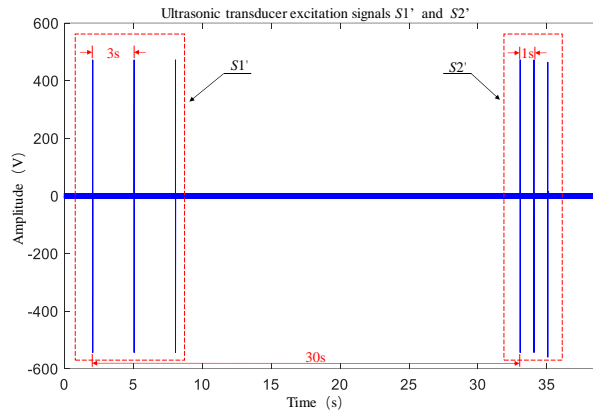
Fig. 2-4 An example of ultrasonic transducer driving signal S1' and S2'

According to the scheme shown in Fig. 2-1, along the track, receivers are arranged at 1km away from the transmitter. UGW signals transmitted by rail are captured by ultrasonic transducers R_A and R_B at the receiver end. Corresponding to the transmitter, R_A is connected to the rail waist of Rail 1, and R_B is connected to the rail waist of Rail 2. As shown in Fig. 2-5, within the dotted box is a receiver structure. The ultrasonic transducers R_A and R_B at the receiver end convert the obtained UGW signals into electrical signals and send them to the receiver. Both received signals are processed and acquired in two identical processing lines in the receiver. These lines consist of an amplification stage (based on an operational amplifier) and a band-pass filter to discard undesired noise. Through the Analog-Digital Converter (ADC), the digital signals are sent to the ARM core-board for further processing operation.
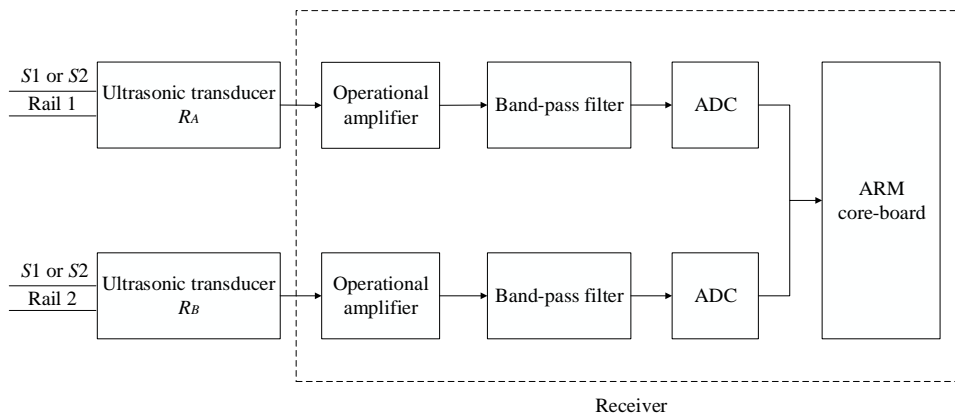
Fig. 2-5 Block diagram for the UGW receiver

Corresponding to the transmitter, the ultrasonic transducer R_A and R_B in the receiver end obtain the UGW signals S1 and S2 from the two adjacent different sections alternately at 30s intervals. All the odd-numbered receivers get the signal S1 from left and S2 from right, while all the even-numbered receivers obtain the signal S2 from left and S1 from right. By checking the time and frequency characteristics of the received signals over a certain interval containing the UGW signals transmitted by T_A and T_B, the status of the corresponding track section under analysis can be determined. Fig. 2-6 is an example of a UGW signal from an odd-numbered receiver in Rail

17

2. Although the graph is similar to Fig. 2-4, each signal group is a UGW signal, not a square-wave signal at the transmitter.
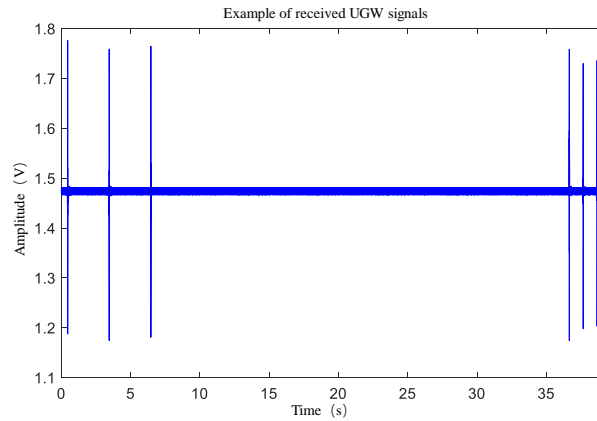
Fig. 2-6 An example of received UGW signals by an odd receiver

2.2　The Realization of RNN and Visual Dimension Reduction

2.2.1　Long-Short Term Memory Network

In the traditional neural network model, data are from the input layer to the hidden layer and then to the output layer. Layer to layer is fully connected, and the nodes between each layer are connectionless. This ordinary neural network is unable to solve the problem which there is a connection among many input links. RNN is a neural network for modeling sequence data, the current output of a sequence is also related to the previous output [73-75]. Fig. 2-7 is the circulation structure of RNN, for the module A of neural network, there is an input i_t at a certain time and then outputs a value h_t. Cycle **A** allows the information to be transmitted from the current network to the next.
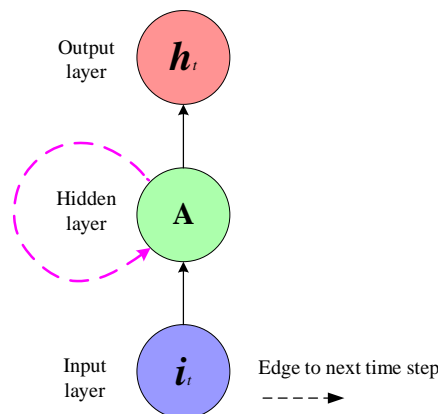
Fig. 2-7 Circulation structure of RNN

RNN can be seen as multiple copies of the same neural network module **A**, and each neural network module passes messages to the next. So, after the loop of Fig. 2-7 is expanded, the unfolded circulation structure of RNN can be acquired as in Fig. 2-8.
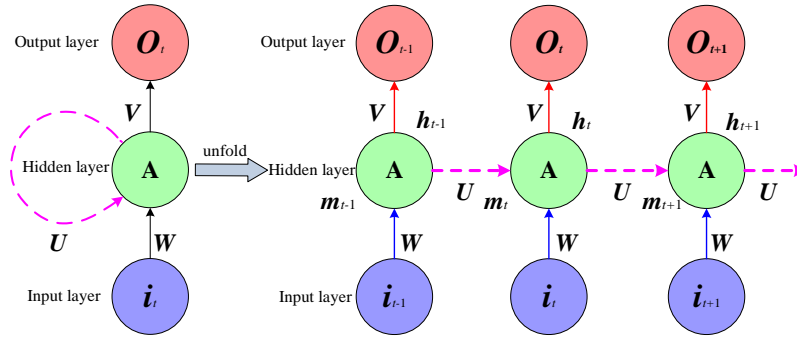
Fig. 2-8 Unfolded circulation structure of RNN

As can be seen from Fig. 2-8, RNN is usually composed of three layers: input layer, hidden layer and output layer. For time t, i_t is the input of RNN, m_t is the input of RNN hidden layer, h_t is the output of RNN hidden layer, W is the weight from input layer to hidden layer, U is the weight from the previous moment on the hidden layer to the current moment, V is the weight from hidden layer to output layer. In the structure of RNN, each neuron module of RNN calculates the input m_t of the current neuron by the input i_t of the current time and the output h_{t-1} of the previous moment, then through the activation function to get h_t, and passes h_t to the hidden unit of the next moment. RNN is a time-based neural network model, so Back Propagation Through Time (BPTT) algorithm is used to calculate back-propagation loss or error. RNN minimizes the cost function by Stochastic Gradient Descent (SGD) algorithm.

The key point of RNN network structure lies in that it can connect the previous information to the current task. However, with the continuous increasing of time interval, the output calculation of the current hidden layer of RNN model depends on the calculation of the n previous times, which leads to an exponential increase in computational load, a significant increase in model training time, and the loss of learning ability to connect the remote information (gradient will disappear). Therefore, RNN model is not directly used for long-term memory calculation. The Long Short-Term Memory (LSTM) network exactly solves this problem. LSTM is a special type of RNN, which can solve the problem that RNN cannot deal with the long-distance dependency [76-77]. Fig. 2-9 is a comparison between LSTM and traditional RNN, where the hidden layer of traditional RNN has only one state, namely h, and in the hidden layer of LSTM, a cell state c is added to preserve the long-term state. The LSTM model in Fig. 2-9 is expanded according to the time dimension and shown in Fig. 2-10.
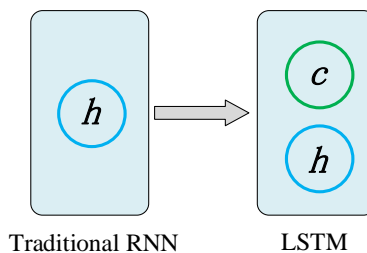
Fig. 2-9 The comparison of traditional RNN and LSTM

19
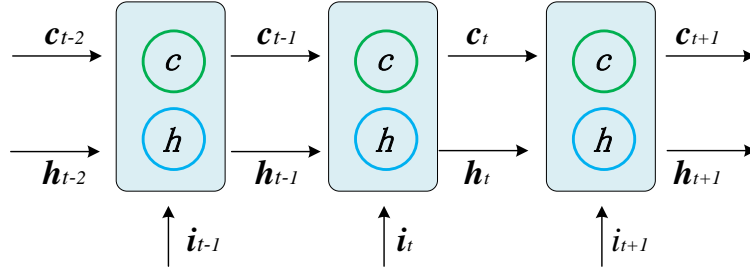
Fig. 2-10 LSTM expanding in time dimension

At the moment t, the LSTM has three inputs: the input value i_t of the current network, the output value h_{t-1} of the LSTM at previous moment, and the cell state c_{t-1} of the previous moment. At the same time, there are two outputs: the current time LSTM output value h_t, and the current time cell state c_t. i, h and c are all vectors.

LSTM uses two gates to control the content of the cell state c, where the forget gate determines how much of the cell state c_{t-1} of the previous time is retained to the current state c_t; and the input gate determines how much of the input i_t of the current time network is saved to the cell state c_t. LSTM uses the output gate to control how much cell state is output to the current output value h_t of LSTM. Forgot gate can be expressed as an expression (2-1), where W_f is the weight matrix of the forgot gate, $[h_{t-1}, i_t]$ means to connect two vectors h_{t-1} and i_t into a longer vector, b_f is the bias term of the forget gate, and σ is the Sigmoid function.

$$F_t = \sigma(W_f \cdot [h_{t-1}, i_t] + b_f) \tag{2-1}$$

Input gate can be represented by equation (2-2), where W_i is the weight matrix of the input gate and b_i is the bias term of the input gate.

$$I_t = \sigma(W_i \cdot [h_{t-1}, i_t] + b_i) \tag{2-2}$$

The current input state $\tilde{c}_t$ is calculated by the input at the last time and the current time, which can be expressed as equation (2-3), where W_c is the weight matrix of the cell state, b_c is the bias term of the cell state, and tanh is the hyperbolic tangent function.

$$\tilde{c}_t = \tanh(W_c \cdot [h_{t-1}, i_t] + b_c) \tag{2-3}$$

The cell state c_t of the current moment can be expressed by equation (2-4), that means c_t is the result obtained by multiplying the forget gate F_t by the last cell state c_{t-1} according to the element. Then, multiplying the input gate I_t by the current input cell state $\tilde{c}_t$ also according to the element, and then adding the two products together.

$$c_t = F_t \cdot c_{t-1} + I_t \cdot \tilde{c}_t \tag{2-4}$$

Thus, the current memory $\tilde{c}_t$ and long-term memory c_{t-1} of LSTM are combined to form a new cell state c_t. Under the control of the forget gate, the long-term information can be saved, and due to the control of the input gate, the negligible content can also be avoided into the memory.

The output gate can be represented by (2-5), where W_o is the weight matrix of the output gate and b_o is the bias term of the output gate.

$$O_t = \sigma(W_o \cdot [h_{t-1}, i_t] + b_o) \tag{2-5}$$

The final output h_t of LSTM is determined by both the output gate and the cell state.

$$h_t = O_t \cdot \tanh(c_t) \tag{2-6}$$

The above (2-1) to (2-6) is the formula for forward direction calculation of LSTM.

2.2.2 t-SNE Dimension Reduction Algorithm

t-Distributed Stochastic Neighbor Embedding (t-SNE) algorithm is a high-dimensional data visualization technology. By reducing the dimension of high-dimensional data point and giving two-dimensional (2D) or three-dimensional (3D) coordinate point, the data can be visualized in a 2D or 3D space that can be easily understood.

t-SNE is developed from the Stochastic Neighbor Embedding (SNE) algorithm. SNE algorithm is used to convert the Euclidean distance between high-dimensional data points into the probability representing the similarity between the data. The similarity between high-dimensional data points x_i and x_j can be expressed by conditional probability $p(j|i)$, that is, if the Gaussian distribution centered on x_i is used to select adjacent points, then the probability of x_i choosing x_j as the adjacent point is $p(j|i)$ [78]. If two data points are close to each other, then $p(j|i)$ is larger, if the distance is very far, $p(j|i)$ can be close to infinitesimal. The conditional probability $p(j|i)$ of high-dimensional data similarity is defined as equation (2-7), where σ_i is the variance of the Gauss distribution centered on x_i.

$$p(j|i) = \frac{\exp(\dfrac{-\| x_i - x_j \|^2}{2\sigma_i^2})}{\sum_{k \neq i} \exp(\dfrac{-\| x_i - x_k \|^2}{2\sigma_i^2})} \tag{2-7}$$

Similarly, for low-dimensional point y_i (corresponding to high-dimensional x_i) and y_j (corresponding to high-dimensional x_j), the conditional probability $q(j|i)$ of the similarity between the data is estimated, all variances σ_i of the Gaussian distribution is set as $1/\sqrt{2}$. The similarity probability $q(j|i)$ between the data point y_i and y_j in low dimensional space after mapping is as follows:

$$q(j \mid i) = \frac{\exp(-\| y_i - y_j \|^2)}{\sum_{k \neq i} \exp(-\| y_i - y_k \|^2)} \tag{2-8}$$

Theoretically, if low-dimensional data points correctly represent high-dimensional data points, the $q(j|i) = p(j|i)$, Kullback-Leibler (KL) divergence is selected to verify whether $q(j|i)$ can represent $p(j|i)$. SNE uses gradient descent method to calculate the sum of minimized KL divergence of all data points. The loss function is as follows:

$$C = \sum_i KL(P_i \| Q_i) = \sum_i \sum_j p(j \mid i) \log \frac{p(j \mid i)}{q(j \mid i)} \tag{2-9}$$

——P_i represents the conditional probability distribution of all other data points on the basis of a given data point x_i.

——Q_i represents the conditional probability distribution of other low-dimensional mapping data points on the basis of a given low-dimensional mapping data point y_i.

By taking the gradient of SNE loss function to y_i, equitation (2-10) can be obtained:

$$\frac{\delta C}{\delta y_i} = 2 \sum_j (p(j \mid i) - q(j \mid i) + p(i \mid j) - q(i \mid j))(y_i - y_j) \tag{2-10}$$

Due to the asymmetry of KL divergence, the weights of different types of errors between the data points to distances are not uniform. In other words, when the dispersive low-dimensional data points are used to represent the aggregate high-dimensional data points, the loss value is large, and the aggregate low-dimensional data points are used to represent the dispersive high-dimensional data points, the loss value is small. The purpose of minimizing SNE loss function is to preserve the local structure of high-dimensional data as much as possible in low-dimensional data. However, in the loss function, when the distance between high-dimensional data points are distant, the low-dimensional points after mapping are comparatively very close, which is unreasonable.

Consequently, Laurens van der Maaten proposes t-SNE algorithm to solve the problem of the asymmetry in SNE algorithm and the problem of cluster congestion between different classes [79]. In the process of dealing with the asymmetric problem, the joint probability distribution is used to replace the conditional probability distribution, and the joint probability of low-dimensional space and high-dimensional space is obtained as shown in equation (2-11) and (2-12), respectively.

$$q_{ij} = \frac{\exp(-\| y_i - y_j \|^2)}{\sum_{k \neq i} \exp(-\| y_i - y_k \|^2)} \tag{2-11}$$

$$p_{ij} = \frac{p_{j|i} + p_{i|j}}{2n} \qquad (2\text{-}12)$$

The obtained loss function is:

$$C = \sum_i KL(P \| Q) = \sum_i \sum_j p_{(ij)} \log \frac{p_{(ij)}}{q_{(ij)}} \qquad (2\text{-}13)$$

The y_i is calculated by the loss function and the result is:

$$\frac{\delta C}{\delta y_i} = 4 \sum_j (p_{ij} - q_{ij})(y_i - y_j) \qquad (2\text{-}14)$$

In order to solve the problem that different clusters tend to be crowded together after data are mapped from high-dimensional space to low-dimensional space, t-distribution with 1 freedom degree is introduced into low-dimensional space in t-SNE algorithm. Compared with normal distribution, the tends to be 0 at the tail of t-distribution is slower. The joint probability formula for such low-dimensional data changes to:

$$q_{ij} = \frac{(1 + \| y_i - y_j \|^2)^{-1}}{\sum_{k \neq l} (1 + \| y_k - y_l \|^2)^{-1}} \qquad (2\text{-}15)$$

Meanwhile, the y_i is calculated by the loss function and the result is:

$$\frac{\delta C}{\delta y_i} = 4 \sum_j (p_{ij} - q_{ij})(y_i - y_j)(1 + \| y_i - y_j \|^2)^{-1} \qquad (2\text{-}16)$$

2.3   Spread Spectrum Communication

2.3.1 The Basic Principle of DS-SS Communication

Spread Spectrum (SS) technology is an information transmission mode. SS sequence is used to modulate signal at the transmitter, thus the spectrum width of the signal is much larger than the bandwidth needed for the transmitted information. At the receiver end, the same SS sequence is used for correlation processing and demodulation, and finally the transmitted information data is recovered. In other words, after the original signal is processed by the SS technology, the spectrum of the signal is broadened and this broadening is realized by the SS sequence modulation method, and the receiver uses correlation processing to de-spread. SS communication systems can be divided into DS-SS, time hopping, frequency hopping, linear frequency modulation and the combination of the methods mentioned before according to the different SS modes. DS-SS expands the spectrum of the signal directly at the transmitter by using the high bit rate SS sequence, and de-spreads the signal at the receiver by using the same sequence [80-82].

The outputs symbol duration is T_a, symbol rate is R_a, and information stream is $a(t)$, $R_a=1/T_a$, signal $a(t)$ can be expressed in the form of equation (2-17). Among them, a_n is information code, by taking probability P of +1 or taking probability $1-P$ of -1, g_n is gate function.

$$a(t) = \sum_{n=0}^{\infty} a_n g_n (t - nT_a) \tag{2-17}$$

The symbol width generated by the pseudo-random code generator is T_c, the rate is R_c and the pseudo-random code is $c_1(t)$, $R_c = 1/T_c$. $c_1(t)$ can be expressed by equation (2-18), where c_n is a pseudo-random code element with +1 or - 1, and $g_c(t)$ is gate function.

$$c_1(t) = \sum_{n=0}^{\infty} c_n g_c (t - nT_c) \tag{2-18}$$

The spread spectrum process essentially adds or multiplies the code $a(t)$ with the pseudo-random code $c(t)$ of module 2. The pseudo-random code rate R_c is much larger than the information rate R_a. Generally, the ratio of R_c/R_a is an integer and $R_c/R_a \geq 1$, so the extended sequence rate is still pseudo-random code rate R_c. The extended sequence $d(t)$ can be expressed by equation (2-19), where d_n is shown in equation (2-20).

$$d(t) = a(t)c_1(t) = \sum_{n=0}^{\infty} d_n g_c (t - nT_c) \tag{2-19}$$

$$d_n = \begin{cases} +1 & a_n = c_n \\ -1 & a_n \neq c_n \end{cases} \quad (n-1)T_c \leq t \leq nT_c \tag{2-20}$$

Then, the SS sequence is used to modulate the carrier signal, so that the spread spectrum modulated radio frequency signal is obtained. In principle, most of the digital modulation methods can be used for modulation of DS-SS systems. Taking Binary Phase Shift Keying (BPSK) modulation as an example, the modulated signal $s(t)$ with carrier frequency f_0 is obtained by:

$$s(t) = d(t)\cos(2\pi f_0 t) = a(t)c_1(t)\cos(2\pi f_0 t) \tag{2-21}$$

At the receiver end, after receiving the spread spectrum signal through high-frequency amplification and mixing, a signal including useful signal $s_1(t)$, channel noise $n(t)$, interference signal $J(t)$ and spread spectrum signal $s_J(t)$ of other networks are obtained, i.e. the received spread spectrum signal can be expressed as:

$$r_1(t) = s_1(t) + n(t) + J(t) + s_J(t) \tag{2-22}$$

The pseudo-random sequence generated by the pseudo-random code generator at the receiver end is the same as that generated by the transmitter end, but the starting time or initial phase may

be different, which is $c_2(t)$. The despreading process is the same as the spread spectrum process. The local pseudo-random sequence $c_2(t)$ is multiplied by the received signal. The multiplied sequence is:

$$
\begin{aligned}
r_2(t) &= r_1(t)c_2(t) \\
&= s_1(t)c_2(t) + n(t)c_2(t) + J(t)c_2(t) + s_J(t)c_2(t) \\
&= s'(t) + n'(t) + J'(t) + s'_J(t)
\end{aligned}
\tag{2-23}
$$

As for the signal component $s'(t)$, there is:

$$
s'(t) = s_1(t)c_2(t) = a(t)c(t)c_2(t)\cos(2\pi ft)
\tag{2-24}
$$

If the locally generated pseudo-random sequence $c_2(t)$ is synchronized with the $c_1(t)$ in the transmitter end, i.e. $c_1(t)=c_2(t)$, and then $c_1(t)c_2(t)=1$, so that the signal component $s'(t) = a(t)\cos(2\pi ft)$, where f is the carrier frequency of the received signal. The bands of the following filters just allow the signal to pass through, thus it can enter into the demodulator to demodulate the useful signal.

Since $n(t)$, $J(t)$ and $s(t)$ signals are not correlated with pseudo-random sequences, they are equivalent to a spread spectrum under the action of correlated de-spread. When their frequency bands are extended, their spectral densities decrease, which greatly reduces the interference and power into the signal band and improves the input signal-to-noise ratio (SNR) of the demodulator. Therefore, the anti-interference ability of the system is improved. DS-SS communication has strong anti-jamming ability, good anti-fading characteristics and good anti-multipath effect. It can provide multiple accesses to digital signals or analog signals, as well as a secure channel for information transmission, which has been increasingly applied to military communications, navigation, positioning, mobile communications and other aspects [83-85].

2.3.2 LS Code

In proving the coding theorem, Shannon pointed out that the signals with white noise statistical properties can be used to code. However, modulation, amplification, detection, control and synchronization of white noise cannot be realized at present, which can only be approached by pseudo-random codes with statistical properties similar to white noise, and these pseudo-random codes can be used as the spread spectrum sequence of the SS system. This type of pseudo-random code is called the Pseudo-Noise (PN) sequence.

In 1961, Golay put forward the concept of complementary sequence in the literature [86], which consists of complementary sequence a and sequence b. Set $a = [a_0, a_1, \cdots, a_{N-1}]$, $b = [b_0, b_1, \cdots, b_{N-1}]$, the length of the two sequences is both N, where $a_i=\pm 1$, $b_i=\pm 1$, $0\leq i\leq N-1$. If (a, b) satisfies:

$$R_a(\tau) + R_b(\tau) = \begin{cases} 2N & \tau = 0 \\ 0 & 1 \leq \tau \leq N-1 \end{cases} \tag{2-25}$$

(a, b) is called a complementary sequence pair, in which $R_a(\tau)$ and $R_b(\tau)$ are aperiodic auto-correlation functions (ACF) of sequence a and b, respectively. Meanwhile, the correlation function superposed by these two sequences can form perfect correlation function. Loosely Synchronous (LS) codes are composed of complementary sequences, and they have ideal auto-correlation and cross-correlation characteristics in the interference free window (IFW). Therefore, using LS code as SS sequence can greatly reduce inter-symbol interference (ISI) and multiple access interference (MAI) [87-88].

LS codes consist of complementary sequence pair [89], set $C=[C_1, C_2, \cdots, C_N]$ and $S=[S_1, S_2, \cdots, S_N]$ to be a sequence of length N, and they are orthogonal sequences, and $|C_i|=|S_i|=1$, $i=1, \cdots, N$. C and S are orthogonal sequences, and the ACF of C and S is equal at the zero delay, and the absolute values are equal elsewhere, the signs are opposite. Therefore, the sum of the ACF of C and S can form an ideal ACF. The sum of the cross-correlation functions (CCF) of C and S cannot cancel each other out, but because C and S are orthogonal, the value of the CCF is very small. In order to construct the ideal correlation function, C and S need to be combined by some orthogonal way. In the orthogonal (such as time division, frequency division and orthogonal polarization) interval of C and S, the interaction between C and S should be removed, and their respective correlation functions should be superimposed to form the ideal correlation function, thus forming LS code, which is recorded as $LS = (C, S)$. Record t $R_{\text{ACF}}(\tau)$ to be the aperiodic ACF of LS, which can be expressed as:

$$R_{\text{ACF}}(\tau) = \begin{cases} \displaystyle\sum_{n=\tau+1}^{N} (C_n C^*_{n-\tau} + S_n S^*_{n-\tau}) & 0 \leq \tau \leq N \\ \displaystyle\sum_{n=1}^{N+\tau} (C_n C^*_{n-\tau} + S_n S^*_{n-\tau}) & -N \leq \tau < 0 \end{cases} \tag{2-26}$$

If there exists a random time Δ and $0<\Delta<N$, then:

$$R_{\text{ACF}}(\tau) = \begin{cases} 0 & 0 < |\tau| \leq \Delta \\ 2N & \tau = 0 \end{cases} \tag{2-27}$$

Let $\tau_w=\max\{\Delta\}$, i.e. τ_w takes the maximum value of Δ, then the sequence LS is called a window self-complementary sequence with a bilateral zero correlation window of $2\tau_w+1$, and τ_w is called the window size of IFW. In particular, when $\tau_w=N-1$, i.e. except $\tau=0$, $R_{\text{ACF}}(\tau)$ is zero in anywhere, the sequence LS at the moment is an ideal complementary sequence.

After discussing the ACF of a single sequence, two different sets of LS codes both with the length $2N$ will be discussed: in $LS_1=(C_1, \; S_1)$ and $LS_2=(C_2, \; S_2)$, the CCF of C_1 and C_2, S_1 and S_2 is $R_{CCF}(\tau)$, which can be expressed as follows:

$$R_{C_1,C_2}(\tau) = \begin{cases} \sum_{n=\tau+1}^{N}(C_{1,n}C^*_{2,n-\tau}) & 0 \le \tau < N \\ \sum_{n=1}^{N+\tau}(C_{1,n}C^*_{2,n-\tau}) & -N < \tau < 0 \end{cases} \qquad (2\text{-}28)$$

$$R_{S_1,S_2}(\tau) = \begin{cases} \sum_{n=\tau+1}^{N}(S_{1,n}S^*_{2,n-\tau}) & 0 \le \tau < N \\ \sum_{n=1}^{N+\tau}(S_{1,n}S^*_{2,n-\tau}) & -N < \tau < 0 \end{cases} \qquad (2\text{-}29)$$

$$R_{CCF}(\tau) = R_{C_1,C_2}(\tau) + R_{S_1,S_2}(\tau) \qquad (2\text{-}30)$$

If there exists any time Δ, and $0<\Delta<N$, then $R_{CCF}(\tau)=0$, where $0\le|\tau|\le\Delta$. And still let τ_w takes the maximum value of Δ, then LS_1 and LS_2 are complementary sequences with a bilateral zero correlation window of $2\tau_w+1$. When $\tau_w=N-1$, LS_1 and LS_2 are ideal complementary sequences.

As mentioned above, LS codes consist of two orthogonal complementary sequences. Let L_0 be the length of these two complementary sequences, K be the number of generated LS codes, and W_0 be the number of 0 inserted in the middle of LS codes, usually $W_0=L_0-1$. For the generated K LS codes, the length of each LS code is $L=K\cdot L_0+W_0$. LS codes can be represented by symbol $LS(L_0, L, W_0)$.

2.3.3 Kasami Sequence

Kasami sequence is a quasi-orthogonal sequence proposed by Prof. Kasami in 1960, which has a good cross-correlation value that can satisfy the lower bound of Welch [90]. For any pair of binary sequences with periodic l in M group sequences, the lower bound of cross-correlation can be expressed as follows:

$$\phi_{l,M} \ge l\sqrt{\frac{M-1}{Ml-1}} \qquad (2\text{-}31)$$

Kasami sequence evolves from m sequence. For a group of m sequence a, the qth bit of each sequence in a is taken to form a' and written as $a[q]$. a' is called the sampling sequences of a, by selecting $q=2^{n/2}+1$, where n is the order of sequence a and the period of a' is $2^{n/2}-1$. Repeat sequence a' q times can obtain a new sequence b. On the basis of sequences a and b, by cyclically left-shifting $2^{n/2}-2$ times of sequence b and then adding with sequence a in module 2 can build a new sequence. Including sequences a and b. A total number of $2^{n/2}$ sequences are obtained and

these sequences are called Kasami sequences. Because the extraction process needs the faster clock, the hardware generation of Kasami sequence is relatively complex. Fortunately, the extracted sequence itself is an $n/2$ order m sequence, which can be used to generate the Kasami sequence. On the other hand, it should be noted that not all polynomial pairs of order n or $n/2$ can be used to generate Kasami sequence, and some calculations or tests should be used to detect their cross-correlation values.

There are two kinds of Kasami sequences: the large set and the small set. The large set contains all the sequences in the small set. From the point of view that correlation function matching the lower bound of Welch, only the small set is optimal. The Kasami sequence has a periodic length of $L=2^n-1$, where n is a non-negative even number. Let $\mathbf{u}$ be a binary sequence of length L, let $\mathbf{w}$ be a sequence of sampling intervals of $2^{n/2}+1$ for $\mathbf{u}$. Then the small Kasami set can be defined in the form of (2-32), where T represents the left shift operator, m is the shift parameter of the sequence $\mathbf{w}$, and the symbol $\oplus$ represents module 2 addition. Moreover, a small Kasami set contains $M=2^{n/2}$ sequences.

$$K_s(\mathbf{u},n,m) = \begin{cases} \mathbf{u} & m=-2 \\ \mathbf{u} \oplus T_m\mathbf{w} & m=0,\ldots,2^{n/2}-2 \end{cases} \tag{2-32}$$

The correlation function values of the Kasami sequence are $\{-t(n), -s(n), -1, s(n)-2, t(n)-2\}$, where for even n, $t(n)=1+2^{(n+2)/2}$, $s(n)=(t(n)+1)/2$. The small set Kasami can be expressed by symbol $Kas(n, M, L)$ [91].

Although some work has been done to study the aperiodic correlation properties of sequences, the selection and optimization of sequences with appropriate aperiodic correlation properties are still concerned by researchers. At present, the selection of sequences with good correlation characteristics is usually based on the experience. The complexity of this study will increase with the increase of sequence length, which limits the possibility of further study. The common way to solve this problem is to use a suboptimal process, that means to limit the study to a small range, or to stop the study when the characteristic parameters of the evaluation sequence reach a certain threshold.

2.4   Hilbert Transform and Wavelet Transform

Hilbert Transform of signal $s(t)$ can be considered as the result of convolution of signal $s(t)$ with another signal $h(t)=1/(\pi t)$, where $h(t)$ is called Cauchy kernel. Because $h(t)$ is not integrable, the integral of the convolution defined is not convergent. Therefore, HT can be defined by Cauchy principal value (represented by $p.v.$). The result of HT is expressed as $H[s(t)]$, $y(t)=H[s(t)]$, and there are:

$$y(t) = H[s(t)] = s(t) * h(t) = s(t) * \frac{1}{\pi t} = \frac{1}{\pi} \, p.v. \int_{-\infty}^{+\infty} \frac{s(\tau)}{t - \tau} d\tau \qquad (2\text{-}33)$$

$$s(t) = H^{-1}[y(t)] = -\frac{1}{\pi t} * y(t) = -\frac{1}{\pi} \, p.v. \int_{-\infty}^{+\infty} \frac{y(\tau)}{t - \tau} d\tau \qquad (2\text{-}34)$$

Among them, $y(t)$ is the HT of the signal $s(t)$, while $s(t)$ is the inverse HT of signal $y(t)$. From the point of view of signal processing, HT can be regarded as the result of a filtering system in which the original signal $s(t)$ passes through an impulse response $h(t)$. Fourier transform of $h(t)$ can be obtained:

$$H(j\omega) = -j \, \text{sgn}(\omega) \qquad (2\text{-}35)$$

The equation (2-35) can also be expressed as:

$$H(\omega) = \begin{cases} -j & \omega \geq 0 \\ +j & \omega < 0 \end{cases} \qquad (2\text{-}36)$$

Among them, sgn() is a sign function. From the perspective of spectrum, the filter multiplies the positive frequency part of the original signal by $-j$ and the negative frequency part by j, that is the phase of the positive frequency part is shifted by $-\pi/2$, while the negative frequency part is shifted by $\pi/2$ in the condition that the amplitude remains the same [92].

Wavelet transform can divide data, functions or operators into different frequencies components, and then use decomposition method to study the components of corresponding scales. There are two types of WT: Continuous Wavelet Transform (CWT) and Discrete Wavelet Transform (DWT). The expression of DWT is:

$$\text{DWT}_{a,b} = \sum_{n \in Z} f(n) \psi_{j,k}(n) \qquad (2\text{-}37)$$

Among them, $\psi_{j,k}(n)$ is a wavelet function; a is a scale factor, which is used to "compress" or "stretch" the wavelet under the condition of maintaining a complete similarity; and b is an offset parameter, indicating the amount of waveform offset along the time axis. Generally speaking, scale factor and offset parameter are discretized according to the power of 2. In DWT analysis, signals of different frequency bands and resolutions are decomposed into "approximate" and "detailed" parts. DWT uses two sets of functions: scale function (related to low-pass filter) and wavelet function (related to high-pass filter). The signal is decomposed by L layer continuous high-pass filter $h(n)$ and low-pass filter $l(n)$ to obtain different frequency signals. For each level, the "approximate" part A[i], i=1, $\cdots$, L is the result of low-pass filtering, and the "detailed" part D[i], i=1, $\cdots$, L is the result of high-pass filtering, and the L of the decomposition depends on the signal itself.

In WT, since the wavelet function is selectable, different wavelet functions will produce different results. Presently, the commonly used wavelet functions are Haar, Daubechies, Symlets,

Morlet and Mexican Hat. Therefore, self-similarity principle, discrimination function, supporting length, symmetry and regularity are used as the criteria for selecting wavelet functions [93].

2.5 Conclusion

This chapter introduces the UGW-based track breakage detection system and the basic knowledge related to signal processing algorithm, which has lay an effective foundation for the follow-up work of the proposed system improvement and signal processing algorithm.

3 Study on the Denoising and Track Status Recognition Algorithms of UGW Signal

Aiming at the problems of mode mixing and inaccurate signal reconstruction in existing UGW signal denoising, this chapter proposes to use Variational Mode Decomposition (VMD) algorithm to denoise UGW signal. After denoising, the features of UGW signals are extracted under different track status, and an intelligent algorithm is proposed to identify and classify the track status by using the temporal and spatial dependencies of the features. The simulation and experimental results verify the feasibility and reliability of the denoising and intelligent track status recognition algorithm.

3.1 Research on Denoising Algorithm of UGW Signal

3.1.1 Denoising Algorithm of UGW Signal

In order to solve the problem of mode mixing and the failure of correct reconstruction for original signal in existing UGW signal denoising algorithm, the VMD algorithm is proposed. Based on the solving process of classical Wiener filter, Hilbert transform and the variational problem of hybrid frequency, the algorithm finds the optimal solution of the constrained variational model to complete the adaptive signal decomposition, and decomposes the input signal into several mode components which have sparse characteristics [94]. The VMD algorithm determines the center frequency and bandwidth of each intrinsic mode component by iteratively searching the optimal solution of the variational model, and realizes the adaptive "screening" of the signal frequency domain and the IMF components.

The ideal UGW signal s_{UGW} is usually a bandwidth signal modulated by the center frequency of the transducer, which can be represented by the mathematical model shown in (3-1), where the amplitude of the UGW signal is β; ∂ is a positive constant, which determines the bandwidth of the UGW signal; f_c is the center frequency of the ultrasonic impulse signal; and φ is the initial phase of the UGW signal. Fig. 3-1 is an example of the 30kHz ideal UGW signal used in the research.

$$s_{\mathrm{UGW}}(t) = \beta e^{-\partial(t-\tau)^2} \cos(2\pi f_c(t-\tau) + \varphi) \tag{3-1}$$
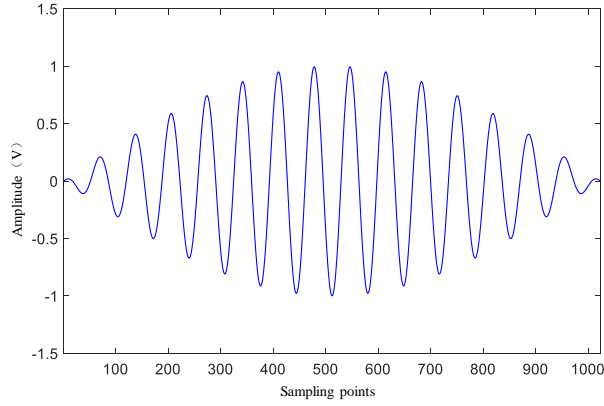
Fig. 3-1 An example of ideal UGW signal

For the actual received signal s_R, besides UGW signal s_{UGW}, there are also environmental interferences and signals containing defective information, which are collectively known as noise signals and denoted as n_{UGW}. The signal s_R can be expressed as:

$$s_R = s_{UGW} + n_{UGW} \tag{3-2}$$

For signal s_R, the whole process for VMD to denoise is displayed in Fig. 3-2.
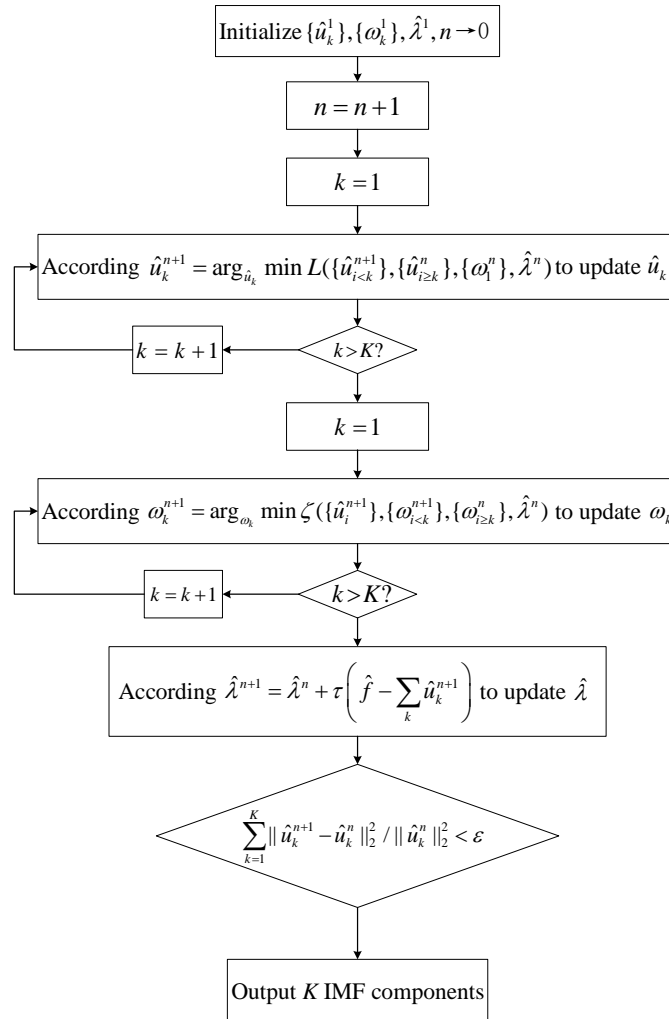
Fig. 3-2 Flow chart of the VMD algorithm

The VMD algorithm decomposes the original signal $x(t)$ into several mode functions $u_k(t)$. The central frequency and bandwidth of each IMF component are updated and iterated, where the bandwidth of the signal is decomposed adaptively. Finally, the narrow-band IMF component with the same number of preset scales K is obtained. In order to estimate the bandwidth of each IMF, the following schemes are proposed:

(1) For each mode function $u_k(t)$, the analytical signal is calculated by HT, and then the single-side frequency spectrum is obtained.

(2) The spectrum of IMF is shifted to the estimated center frequency by index modification.

(3) Gaussian smoothing (i.e., the square root of L^2 norm gradient) is used to demodulate the signals to obtain the bandwidth of each mode function.

The variational constraint problem is:

$$\min_{\{u_k\},\{\omega_k\}} \left\{ \sum_{k=1}^{K} \left\| \partial_t \left\{ [\delta(t) + \frac{j}{\pi t}] * u_k(t) \right\} e^{-j\omega_k t} \right\|_2^2 \right\} \tag{3-3}$$

Among them, $u_k=\{u_1, u_2, \ldots, u_K\}$ is a set of mode functions, $\omega_k=\{\omega_1, \omega_2, \ldots, \omega_K\}$ is the set of central frequencies, ∂_t is the partial derivative of function to time t, $\delta(t)$ is the unit impulse function, j is the imaginary unit, and $*$ represents the convolution.

In order to solve the above constrained optimization problem, the VMD algorithm utilizes the advantages of the quadratic penalty term and Lagrangian multiplier to obtain the augmented Lagrangian function ζ:

$$\zeta(\{u_k\},\{\omega_k\},\lambda) = \alpha \sum_{k=1}^{K} \left\| \partial_t \left\{ \left[\delta(t) + \frac{j}{\pi t} \right] * u_k(t) \right\} e^{-j\omega_k t} \right\|_2^2 + \left\| f(t) - \sum_{k=1}^{K} u_k(t) \right\|_2^2$$
$$+ \left\langle \lambda(t), f(t) - \sum_{k=1}^{K} u_k(t) \right\rangle \tag{3-4}$$

Among them, α is the quadratic penalty term, which represents the bandwidth parameter, and $\lambda(t)$ is the Lagrangian multiplier.

The processing step for VMD algorithm is as follows:

(1) The minimum value of IMF u_k is:

$$\hat{u}_k^{n+1}(\omega) = \frac{\hat{f}(\omega) - \sum_{i\neq k} \hat{u}_i(\omega) + \frac{\hat{\lambda}(\omega)}{2}}{1 + 2\alpha(\omega - \omega_k)^2} \tag{3-5}$$

(2) The minimum value of center frequency ω_k is:

$$\omega_k^{n+1} = \frac{\int_0^\infty \omega |\hat{u}_k(\omega)|^2 \, d\omega}{\int_0^\infty |\hat{u}_k(\omega)|^2 \, d\omega} \tag{3-6}$$

(3) The iterative constraint is:

$$\frac{\sum_{k=1}^{K}\left\|\hat{u}_k^{n+1}-\hat{u}_k^n\right\|_2^2}{\left\|\hat{u}_k^n\right\|_2^2}<\varepsilon \tag{3-7}$$

As for the iterative constraint shown in equation (3-7), the following processing is continued:

a.   Initialize $\{\hat{u}_k^1\}$, $\{\omega_k^1\}$, $\hat{\lambda}^1$, $n\leftarrow 0$

b.   Add 1 to the number of iterations

c. k=1: K, as for $\omega\geq 0$, update the IMF according to (3-8) and the frequency function according to (3-9):

$$\hat{u}_k^{n+1}(\omega)\leftarrow\frac{\hat{f}(\omega)-\sum_{i<k}\hat{u}_i^{n+1}(\omega)-\sum_{i>k}\hat{u}_i^n(\omega)+\dfrac{\hat{\lambda}^n(\omega)}{2}}{1+2\alpha(\omega-\omega_k^n)^2} \tag{3-8}$$

$$\omega_k^{n+1}\leftarrow\frac{\int_0^{\infty}\omega\left|\hat{u}_k^{n+1}(\omega)\right|^2 d\omega}{\int_0^{\infty}\left|\hat{u}_k^{n+1}(\omega)\right|d\omega} \tag{3-9}$$

d.   For $\omega\geq 0$, Lagrangian multiplier is updated according to equation (3-10), where τ denotes the updating parameters. Usually, in order to achieve better denoising effect, when the signal contains strong noise, let τ=0.

$$\hat{\lambda}^{n+1}(\omega)\leftarrow\hat{\lambda}^n(\omega)+\tau(\hat{f}(\omega)-\sum_k\hat{u}_k^{n+1}(\omega)) \tag{3-10}$$

Repeat the above step b to d until the constraint condition of equation (3-7) is established, and the VMD decomposition algorithm is completed.

3.1.2 Simulation and Experimental Results for Denoising Algorithm

After adding Gaussian white noise, discontinuous noise and impulse interference to the ideal UGW signal s_{UGW}, applied the VMD algorithm to denoise the signal. The denoising effect of the algorithm is determined by the deviation between the reconstructed signal and the ideal signal, as well as the SNR of the reconstructed signal. Meanwhile, the simulation result will be further verified by the experiment.

The reconstructed signal $\tilde{s}_{\text{UGW}}$ is the sum of all IMF components IMF_i which contain the useful part of signals.

$$\tilde{s}_{\text{UGW}}=\sum_{i=k+1}^{N}IMF_i(t) \tag{3-11}$$

SNR is an important index to measure the quality of signals. Equation (3-12) is used to calculate the SNR in decibel (dB), where P_s is the average energy of the signal to be detected and P_n is the average energy of the noise sampling points.

$$SNR\big| dB = 10 \times \log_{10} \frac{P_s}{P_n} = 10 \times \log_{10} \left[\frac{\frac{1}{N}\sum_{i=1}^{N}\left|\tilde{s}_{\mathrm{UGW}}(i)\right|^2}{\frac{1}{N}\sum_{i=1}^{N}\left|n_{\mathrm{UGW}}(i)\right|^2} \right] \qquad (3\text{-}12)$$

Firstly, when the added noise n_{UGW} is Gaussian white noise with the average of 0, the variance of 1, and the amplitude of 0.5V, only one kind of noise is known to be added to the original UGW signal. Therefore, for VMD algorithm, setting the decomposition mode $K=3$ is enough to obtain the effective signal, noise and residual components. On the other hand, in order to represent the frequency range of each decomposed mode component, set the quadratic penalty term, namely the bandwidth parameter $\alpha=2000$. Certainly, if the initial set number of decomposition modes K does not match the actual decomposition situation, the decomposition process will be adaptively updated according to the quadratic penalty term. Fig. 3-3 is the mode decomposition after using the VMD algorithm.
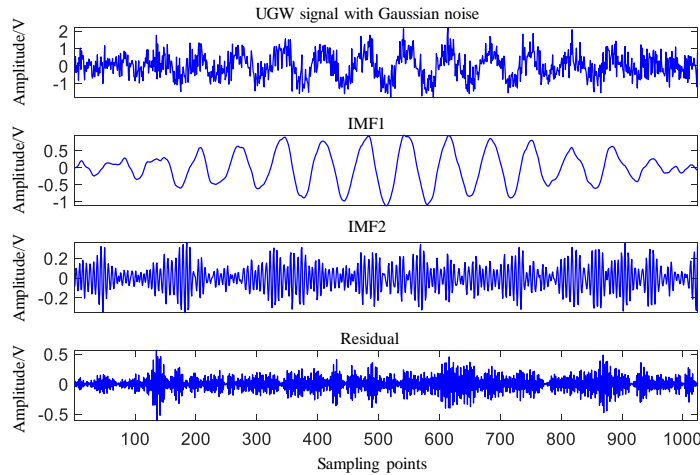
Fig. 3-3 Signal s_R with Gaussian noise and IMFs obtained by the VMD algorithm

As can be seen from the graph, the first level of decomposition by the VMD algorithm completely extracts the useful signal, and IMF2 contains most of the noise signal. The VMD algorithm is efficient in decomposing the signal, and only two times the useful signals are stripped off from the noise. Meanwhile, comparing the reconstructed signal with the original signal in Fig. 3-4, the deviation between them is small. The reconstructed signal obtained by VMD algorithm has clean waveform and high SNR, effectively suppressing the mode mixing phenomenon.
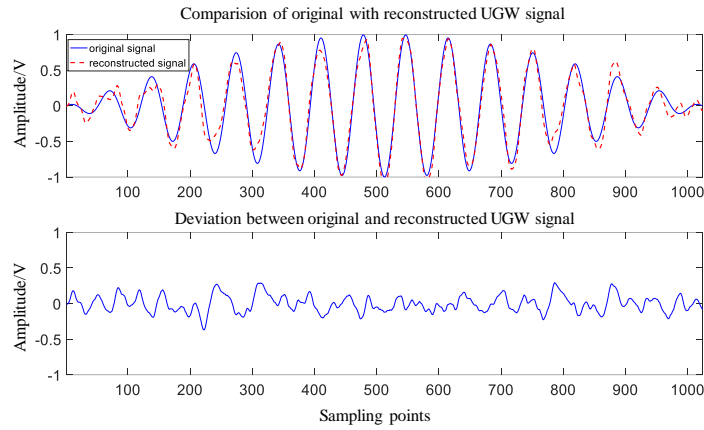
Fig. 3-4 Reconstructed UGW signal and the ideal UGW signal, as well as the deviation between them

Next, let the added noise signal $n_{UGW}=0.2*\cos(2\pi*20000*t-5000\pi)$, add the n_{UGW} to the second half of the original UGW signal to simulate the sudden external knock. Fig. 3-5 and Fig. 3-6 show the IMF components obtained by decomposing the UGW signal with VMD algorithm and the reconstructed signal respectively.

Fig. 3-5 Signal s_R with discontinuous noise and IMFs obtained by the VMD algorithm
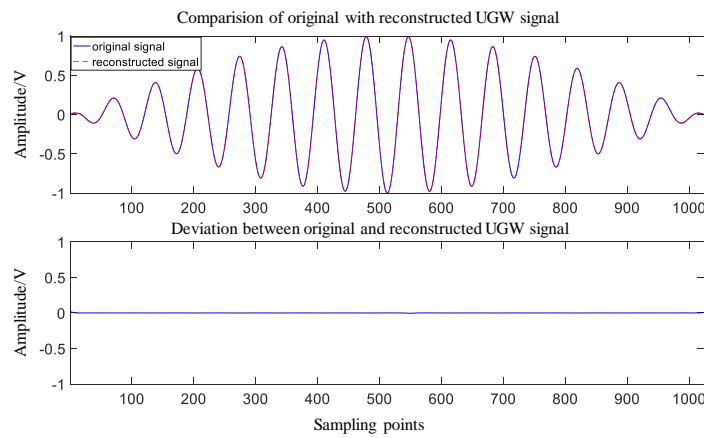
Fig. 3-6 Reconstructed UGW signal and the ideal UGW signal, as well as the deviation between them

In Fig. 3-5, also sets K=3, α=2000, in which the noisy signal is decomposed into IMF1, IMF2, and a residual. The time domain waveform of IMF1 is clean, and most useful signals are included. From the comparison between the reconstructed signal and the original signal in Fig. 3-6, it can be seen that the deviation between them is very small, and the original signal can be accurately reconstructed.

Finally, a rectangular pulse signal with a pulse width of 0.03s, duty ratio of 50%, and amplitude of ±0.1V is added. When the VMD algorithm is used to process the impulse interference signal, the initial setting which is consistent with the previous two types of noise is used: the number of mode K = 3, and the quadratic penalty term α=2000. Fig. 3-7 is the decomposition result of VMD algorithm. The signal can be reconstructed by using the first intrinsic mode component IMF1, and without mode mixing phenomenon. From the comparison between the reconstructed signal and the original signal in Fig. 3-8, it can be seen that the difference between the reconstructed signal and the original signal is still very small (less than 0.1V), and the SNR of the reconstructed signal is 24.6151dB.
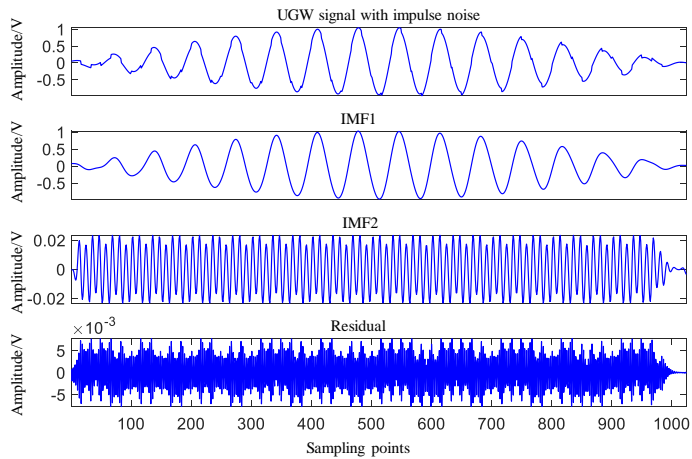
Fig. 3-7 Signal s_R with impulse interference and IMFs obtained by the VMD algorithm

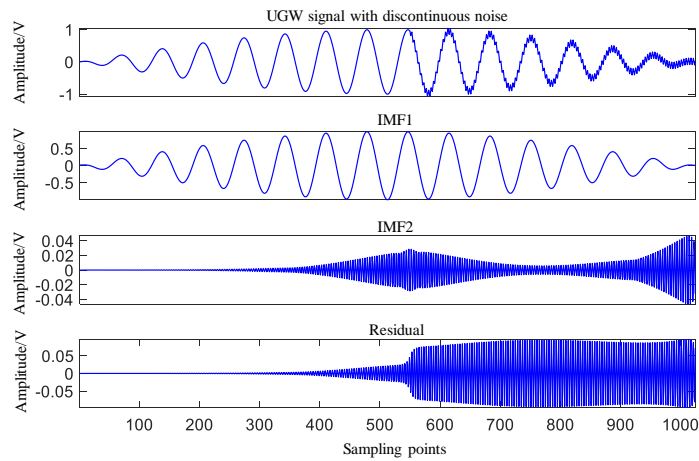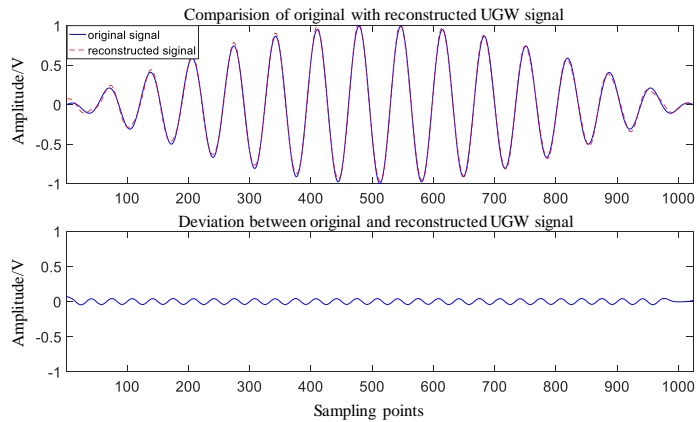Fig. 3-8 Reconstructed UGW signal and the ideal UGW signal, as well as the deviation between them

Tab. 3-1 compares the SNR of the reconstructed signals with three different denoising algorithms under three types of noise conditions, P_s is taken as the average energy of the reconstructed signal.

Tab. 3-1 The comparison among different noise and denoising algorithm

Denosing algorithm Noise type	EMD	EEMD	VMD
Gaussian white noise	8.6966 dB	8.6502 dB	12.7501 dB
Discontinuous noise	14.6660 dB	29.2691 dB	52.6106 dB
Impulse noise	14.3397 dB	16.5071 dB	24.6151 dB

Combining the simulation results of VMD denoising algorithm under three kinds of noises and the SNR results in Tab. 3-1, it can be seen that no matter which kind of the three noises are added to the original UGW signal, the VMD algorithm can get better denoising effect when processing the noisy signal, and the reconstructed signal has little deviation from the original signal. The VMD method has the smallest number of decomposition layer and the highest decomposition efficiency.

On the basis of the above simulation results, the actual noisy UGW signal obtained by experiment is processed and the noisy signal is shown in Fig. 3-9. The EMD algorithm, EEMD algorithm and VMD algorithm are used to denoise the noisy signals respectively, and the IMF components of the noisy signals are obtained respectively as shown in Fig. 3-10 to Fig. 3-12. It can be seen that when EMD algorithm and EEMD algorithm are used to decompose, the number of iterations is large, the decomposition efficiency is low, and the phenomenon of over-decomposition exists. When VMD algorithm is adopted, the signal is decomposed by three iterations, and it can be seen from Fig. 3-12 that IMF1 is the noise introduced in the transmission process, IMF2 is the expected signal with smooth envelope, and the transmitted signal can be reconstructed by IMF2.
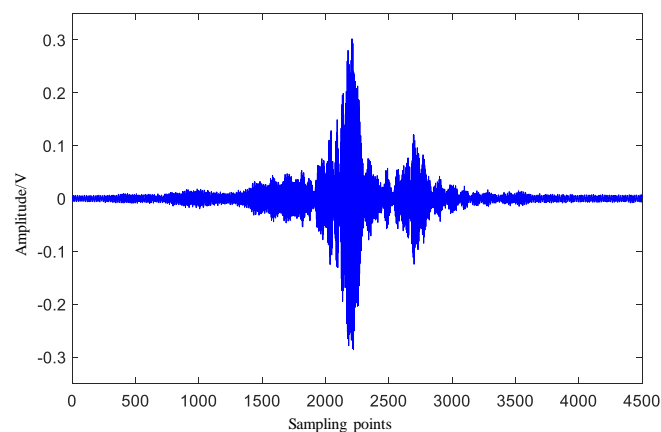
Fig. 3-9 Received real UGW signal with interference
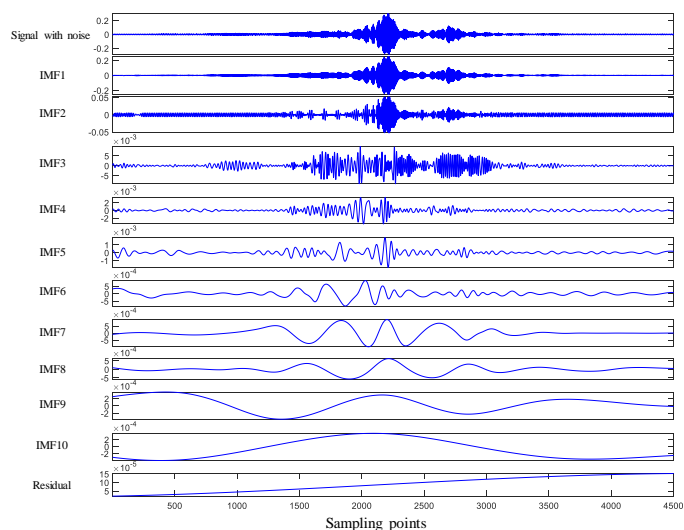
Fig. 3-10 The decomposition result of real UGW signal by EMD algorithm

Fig. 3-11 The decomposition result of real UGW signal by EEMD algorithm
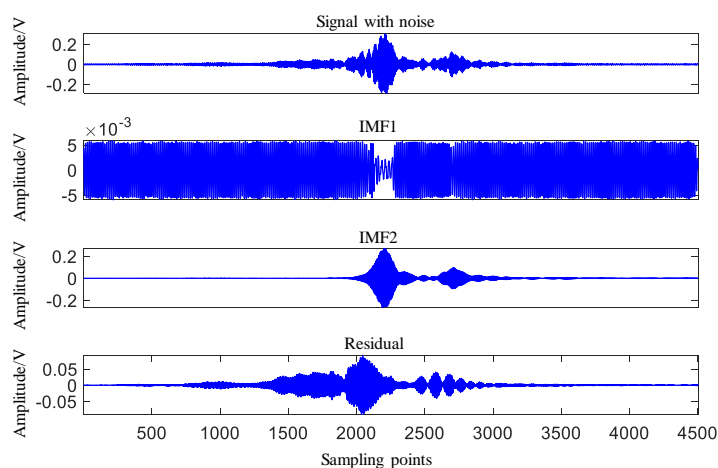
Fig. 3-12 The decomposition result of real UGW signal by VMD algorithm

In order to evaluate the denoising effect for the experimental signal, the values of SNR for these three different methods are also calculated. Let the reconstructed signal as the useful signal, and the noisy part comes from the result which the UGW signal in Fig. 3-9 minus the

reconstructed signal. Then, according to equation (3-12), the values of SNR for these three methods can be observed in Tab. 3-2.
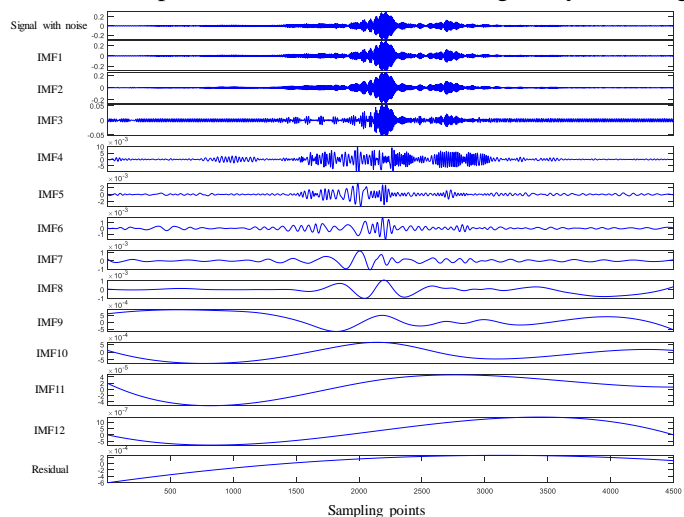
Tab. 3-2 The SNR comparison among different denoising algorithm for experimental results

Algorithm	SNR value
EMD	13.4386
EEMD	13.4237
VMD	18.6786

The simulation and experimental results show that the VMD algorithm can obtain the reconstructed signal with high SNR through less decomposition times, and has obvious denoising effect and high decomposition efficiency. Meanwhile, it effectively solves the problem of mode mixing, over decomposition and the incorrect signal reconstruction.

3.2　Feature Extraction of UGW Signal

Targeting at the denoised UGW signal, in order to identify and classify the track status of a huge monitoring network by using ANN, it is necessary to obtain the features of UGW signals which can distinguish different track status. The larger the differences of features in different track status are, the higher the success rate of status classification will be. Therefore, a track status feature extraction method based on UGW signals is proposed, in order to improve the accuracy of subsequent track status classification.

For each monitoring section, there are three main types of track status: free, occupied and broken. Therefore, at the receiver end, the RMS value V_{rms}, as well as the frequency F_p corresponding to the peak value of the spectrum signal are extracted for the signal captured in the 20ms time window which contains the effective UGW signal. As for two rails of a railway line, Rail 1 and Rail 2 have the same initialization settings and the same transmission signals. Therefore, for the sake of concise description, only the signal of Rail 2 under three track status is analyzed, and the analysis result can be extended to Rail 1. It should be noted that the signals used in extracting the features of different track status are all the measured signals collected from Baoji-Chengdu railway line by the improved track breakage detection system. The distance between the transmitter and the receiver is 1km, and the climate is dry on the day of data collection.

3.2.1　Track Status: Free

When the track section is free, the track is complete, and the train can enter safely. Fig. 3-13 shows an example of two sets of UGW signals from the two adjacent sections in the Rail 2

receiver. It can be observed that the receiver in the middle receives the UGW signal $S1$ from the left section and the UGW signal $S2$ from the right section. These two sets of signals arrive at the receiver 30 seconds apart. Meanwhile, a signal over a 20ms period containing useful UGW signal is shown in Fig. 3-14, which has already eliminated the direct current (DC) bias. After the signal is denoised by VMD algorithm and reconstructed by effective IMF components, the two features of V_{rms} and F_p for the current track status are calculated.

Fig. 3-13 Example of a reception in Rail 2 under free track condition
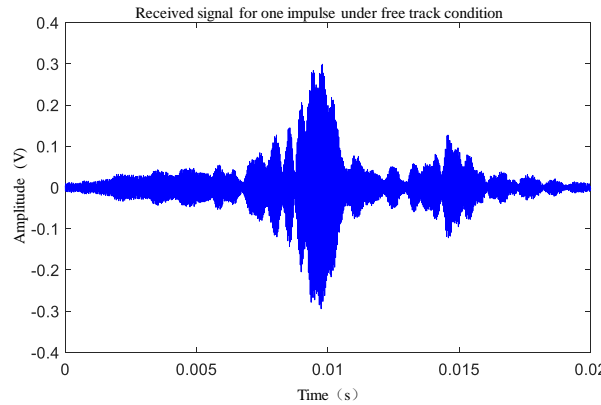
Fig. 3-14 Zoom of an UGW signal received for a free track section

The feature V_{rms} is used to measure voltage variations. It should be noted that at the receiver end, UGW signals are sampled at 250kHz, and 20ms signals contain $N = 5000$ sampling points. Therefore, for each UGW signal, the feature V_{rms} can be calculated by equation (3-13), v_n represents the signal amplitude of the nth sampling point.

$$V_{rms} = \sqrt{\frac{1}{N} \sum_{n=1}^{N} v_n^2}$$
(3-13)

The extraction of frequency feature F_p is obtained by FFT processing for the denoised signal. Fig. 3-14 shows the result of the FFT result of a UGW signal after denoising, as shown in Fig. 3-15. As expected, the main frequency of the signal mainly concentrates around 30 kHz. Although

there is a peak value at 92 kHz, the amplitude is very small. The peak value is caused by the noise component which cannot be filtered out by the denoising algorithm.
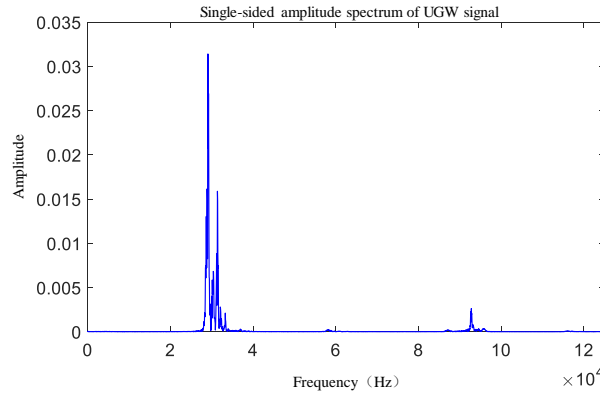
Fig. 3-15 Single-sided amplitude spectrum of one UGW signal

3.2.2 Track Status: Occupied

When a track section is occupied by a train, other trains are not allowed to enter the section. Moreover, as the train approaches this section, the UGW signal would be gradually flooded by the noise caused by train wheelsets. Similarly, with the train moving away from the section, the flooded UGW signal gradually resumes. When the track section is completely occupied by the train, the UGW signal will be completely covered by interference, as shown in Fig. 3-16. Although all the UGW signals are completely flooded by noise under the track occupied condition, the receiver can still obtain 20ms-long signal which should have existed UGW signals according to the synchronous clock. The 20ms signal is shown in Fig. 3-17. Similarly, the signal is denoised by VMD and then FFT is performed to find the feature F_p. The result of FFT is shown in Fig. 3-18. Although the spectrum is still concentrated around 30 kHz, it can be seen that it also contains a lot of unfiltered noise components.
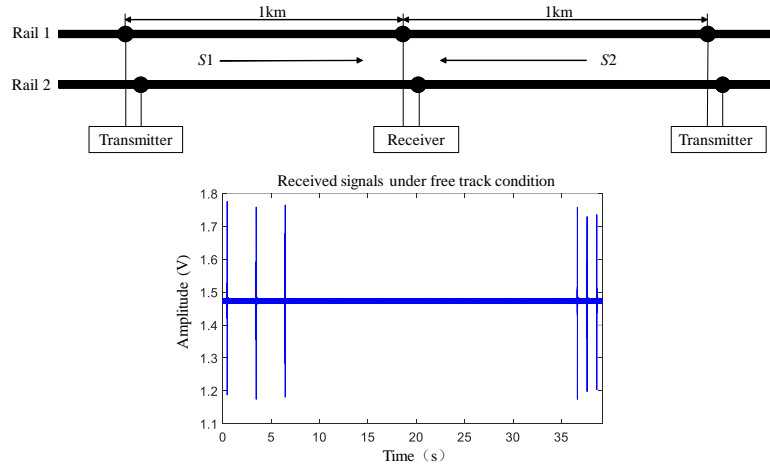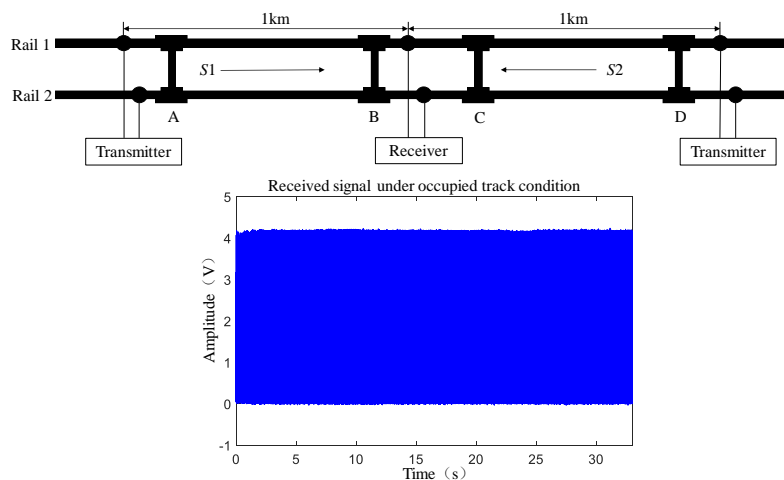

Fig. 3-16 Example of a reception in Rail 2 under occupied track condition
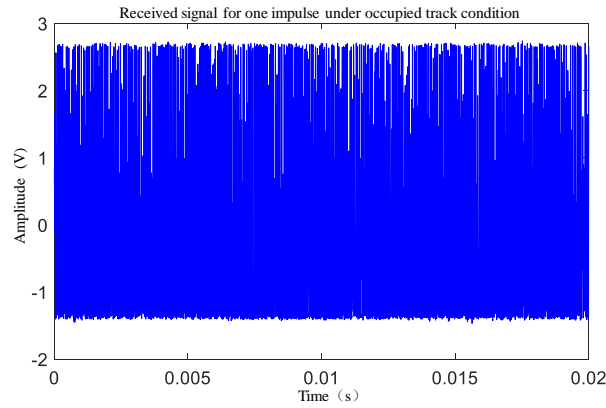
Fig. 3-17 Zoom of an UGW signal received for an occupied track section
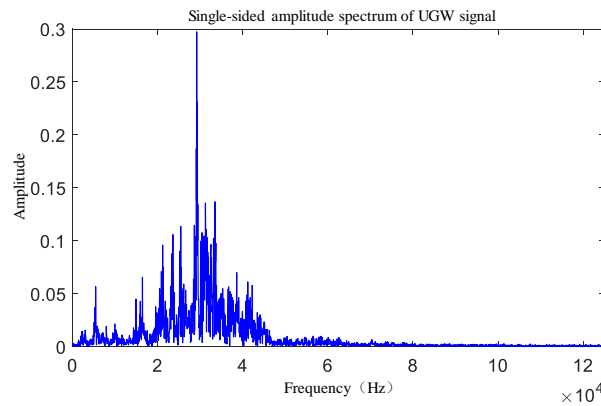
Fig. 3-18 Single-sided amplitude spectrum of one UGW signal

The RMS voltage V_{rms} of track occupied is much higher than that of track free, and the frequency feature F_p is similar to that of rail free.

3.2.3 Track Status: Broken

When track breakage occurs at any point of a section, the transmitted UGW signal cannot be correctly detected by the receiver. Fig. 3-19 shows where track breakages are likely to occur, at E, F, G, and H points. The signal at the receiver end of Rail 2 shown in below is obtained after track breaks at point G. Because the other three locations are in good condition, for Rail 2, the UGW signal $S1$ from the left section can only be received, while the signal $S2$ from the right transmitter is lost. The signal collected by the receiver from the right section of the 20ms is shown in Fig. 3-20. Similarly, the single-sided amplitude-frequency characteristic shown in Fig. 3-21 is obtained by FFT operation after denoising the signal in the 20ms period. It can be seen that there is no frequency component near 30kHz, and only a tiny component exists at 92kHz.

For the broken track section, the feature V_{rms} is much smaller than the corresponding value in the free track section. The frequency feature F_p corresponding to the amplitude of the maximum frequency component is near 92 kHz, which is close to the noise component in the free status, however, the frequencies of $S1$ and $S2$ cannot be identified.
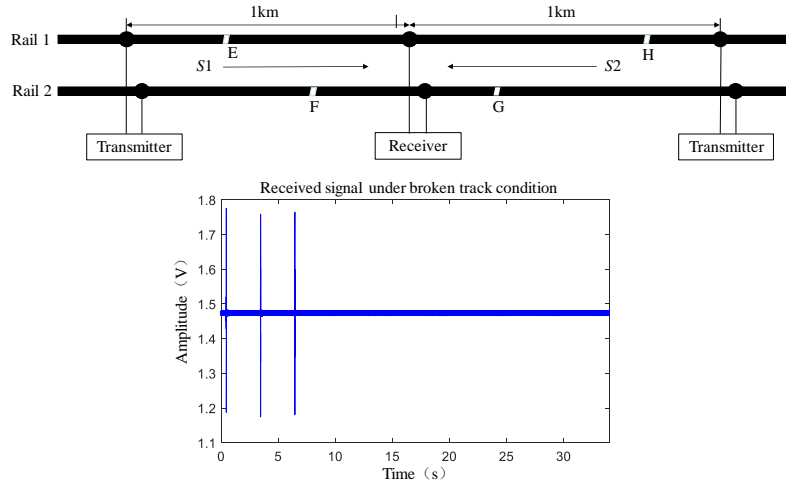
Fig. 3-19 Example of a reception in Rail 2 under broken track condition
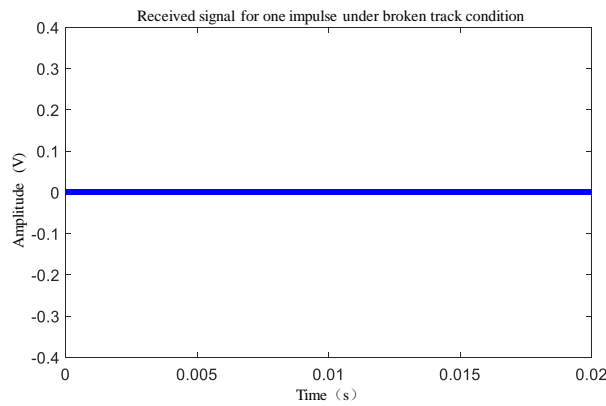
Fig. 3-20 Zoom of an UGW signal received for a broken track section
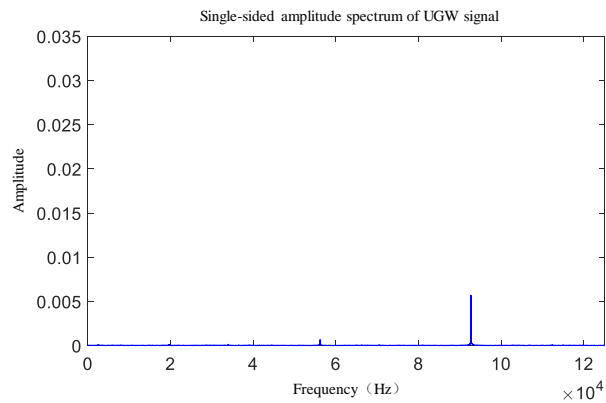
Fig. 3-21 Single-sided amplitude spectrum of one UGW signal

Considering the above situation, it can be concluded that the feature V_{rms} in the time domain is the smallest in the broken status and the largest in the occupied status; the frequency feature F_p corresponding to the amplitude of the maximum frequency component is similar for the occupied status and the free status, but the highest in the broken status. Combined with the features V_{rms} and F_p, the three types of track status can be clearly distinguished. In other words, for the track section i, the features $[V_{rms}\ F_{pi}]$ can be calculated. Therefore, the collected representative data are

analyzed to verify the correctness of the feature extraction methods mentioned above. In Fig. 3-22, the features V_{rms} and F_p of Rail 2 in three status are shown, and each status corresponds to 200 samples.
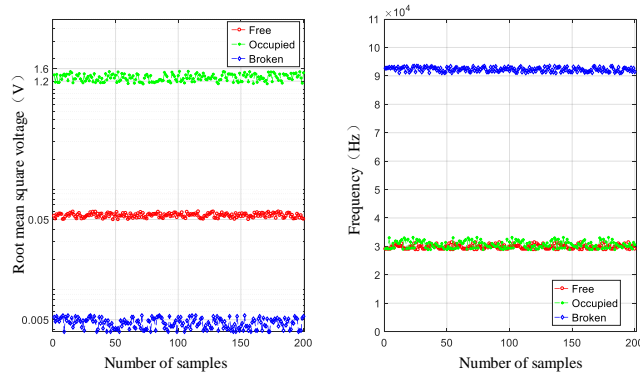
Fig. 3-22 Comparison of two features [V_{rmsi} F_{pi}] for each different track status for Rail 2

As can be seen from Fig. 3-22, when the track section is free, two features [V_{rmsi} F_{pi}] are taken in a small range of their typical values; when the track section is occupied, the value of V_{rmsi} is much higher than that of free, and the value of F_{pi} is close to that of free; when the track breakage occurs, the UGW signal at the receiver is lost, the value of V_{rmsi} is close to 0, and the frequency value F_{pi} corresponding to the highest frequency component is near 92kHz. What happens in Rail 1 is similar to Rail 2.

3.2.4 Temporal and Spatial Dependencies of UGW Features

In Fig. 3-22, the track status can be easily separated in a fixed value form. However, in some cases, the judgement of status trend is also very important. In other words, for track section i, the change of features [V_{rmsi} F_{pi}] in time is important. The information about track status changes overtime, and it can be used to distinguish more complex conditions or effects, such as weather conditions or the effects of rail aging. Therefore, in Fig. 3-23 and Fig. 3-24, the temporal trends of V_{rmsi} and F_{pi} collected in a certain section are analyzed. Each of figure contains six status variations with time.
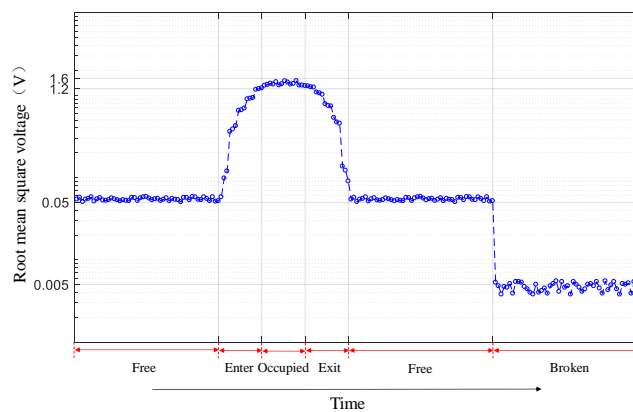
Fig. 3-23 Example of a temporal trend for the feature V_{rmsi} in a certain track section i
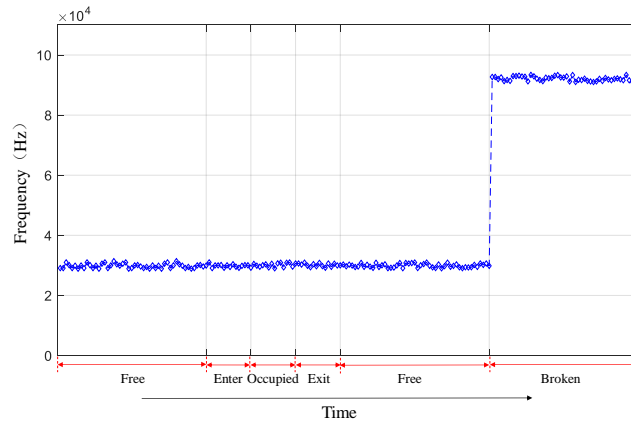
Fig. 3-24 Example of a temporal trend for the feature F_{pi} in a certain track section i

As can be seen from Fig. 3-23, V_{rmsi} stays at a lower constant value when section i is free. When there is a train passing along the track section i, the values for V_{rmsi} start to increase as the train approaches, reaching a maximum when the track section is completely occupied by the train. In the same way, V_{rmsi} decreases gradually as the train exits from the track section i, and then it recovers the previous low value for a free status. Finally, when a breakage occurs in section i, the feature V_{rmsi} drops abruptly to almost zero. With regard to the frequency component F_{pi} shown in Fig. 3-24, no matter whether the track section i is free, the train is approaching or exiting, or the section i is occupied by the train, the maximum frequency component F_{pi} maintains an almost constant value around 30 kHz. Nevertheless, this value sharply increases up to 92kHz when the track status is broken.

On the other hand, it is important to note that the features from other neighboring track sections can also provide additional information about the status of the specific track section i under analysis, due to the spatial dependencies existing among them. Taking those into account, in the proposed UGW-based monitoring system, the broken status is assumed to influence only one track section, whereas the occupied status is likely to influence all the track sections in the specific moving path of the train. This implies that some information from neighboring track sections can enhance the status classification for a certain track section i. In this work, the two aforementioned features [V_{rmsi} F_{pi}] for six neighboring sections are considered to explore their spatial dependencies.

Firstly, it is assumed all the six track sections in Rail 2 are free at the same time, so the two features [V_{rmsi} F_{pi}] for the six sections present a similar value, as shown in Fig. 3-25.
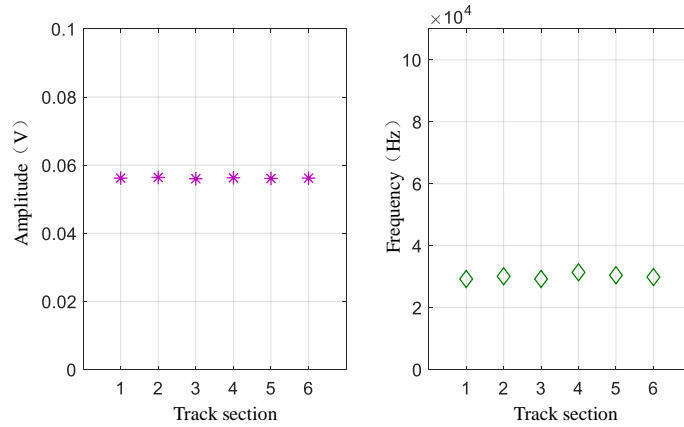
Fig. 3-25 Spatial dependencies of features [V_{rmsi} F_{pi}] for six neighboring track sections under free condition

Then, Fig. 3-26 shows an example case, when the status of track section 3 is broken, whereas the others are free. Compared with the situation in Fig. 3-25, it can be observed that the broken status only affects track section 3 where it occurs, and not the other neighboring sections.
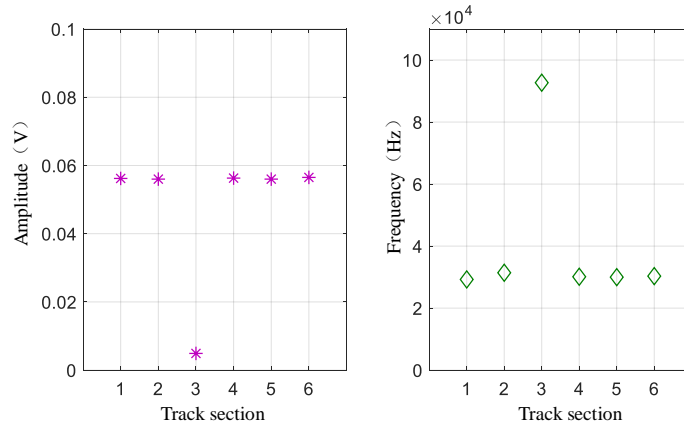
Fig. 3-26 Spatial dependencies of features [V_{rmsi} F_{pi}] for six neighboring track sections when section 3 is broken and others are free

Finally, an illustrative situation, at which a train is passing from track section 1 to track section 6 in Rail 2, is described. The spatial and temporal dependencies of two features [V_{rmsi} F_{pi}] for this situation can be observed in Fig. 3-27, from (a) to (f), at different times. Firstly, at t_1, the track section 1 is occupied by a train, so the feature V_{rms1} is the highest. Even though the other five sections are free, due to the influence of the mechanical noise caused by the train, the adjacent section 2 has relatively higher values than the others. When the train is moving from section 2 to section 5 (from t_2 to t_5), no matter which section is occupied, the feature V_{rmsi} in the corresponding section is the largest, although their immediate neighbors still present relatively higher values than the other three free sections. Finally, when the train arrives in the track section 6, the feature V_{rmsi} for sections 1 to 4 are similar, the value for track section 5 is slightly higher, and the highest value is obtained for track section 6 (time instant t_6). It is worth noting that no matter where the train is, the frequency components F_{pi} for the six sections always show quite stable behavior. It can be concluded from Fig. 3-27 that a train occupying a certain track section affects, not only

that particular track section, but also the immediate adjacent sections. This spatial dependency can be used to improve the final track section status classification.
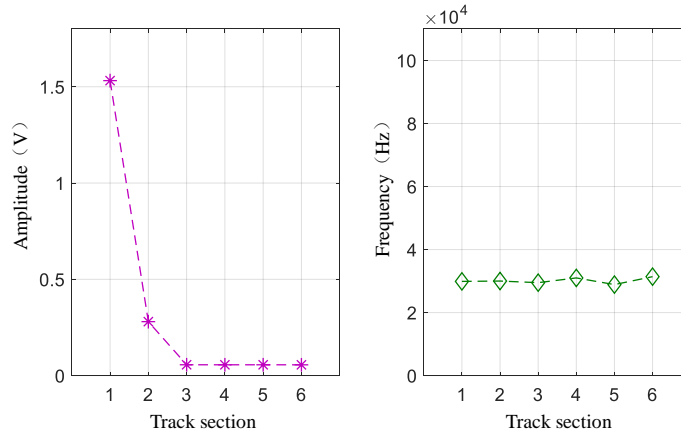
(a) Spatial dependencies of features [V_{rmsi} F_{pi}] for six neighboring track sections when section 1 is occupied by a train (time instant t_1)
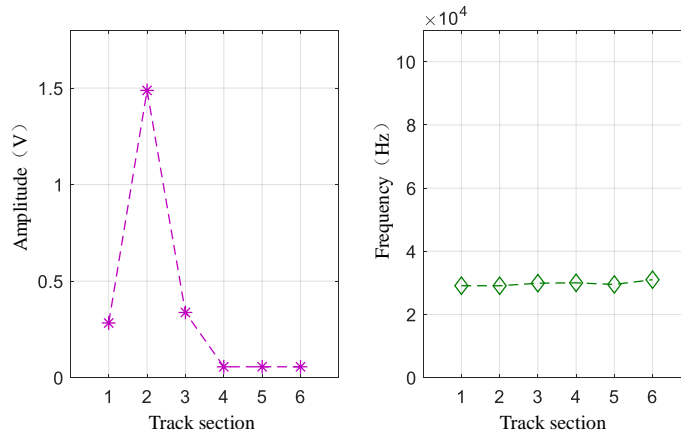
(b) Spatial dependencies of features [V_{rmsi} F_{pi}] for six neighboring track sections when section 2 is occupied by a train (time instant t_2)
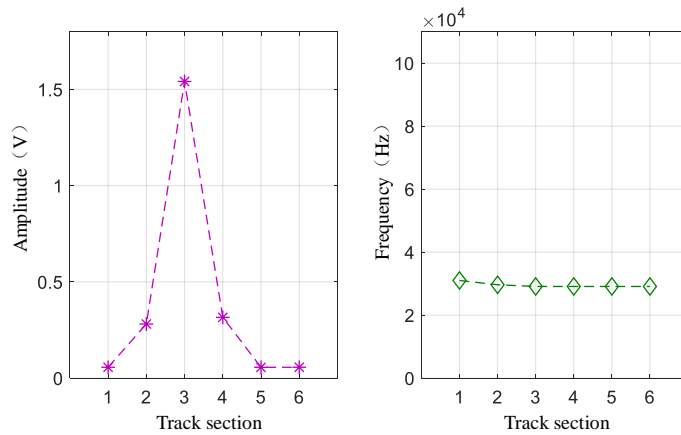
(c) Spatial dependencies of features [V_{rmsi} F_{pi}] for six neighboring track sections when section 3 is occupied by a train (time instant t_3)
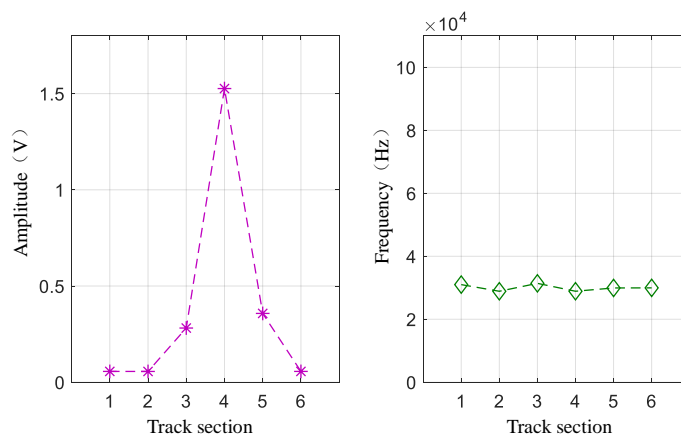
(d) Spatial dependencies of features [V_{rmsi} F_{pi}] for six neighboring track sections when section 4 is occupied by a train (time instant t_4)
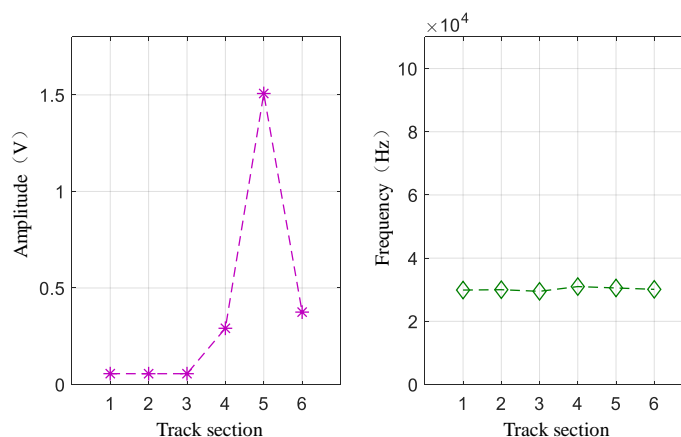
(e) Spatial dependencies of features [V_{rmsi} F_{pi}] for six neighboring track sections when section 5 is occupied by a train (time instant t_5)
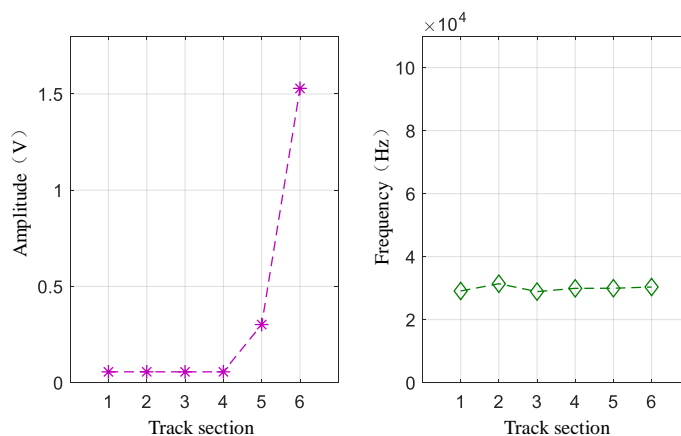
(f) Spatial dependencies of features [V_{rmsi} F_{pi}] for six neighboring track sections when section 6 is occupied by a train (time instant t_6)

Fig. 3-27 Spatial dependencies of features [V_{rmsi} F_{pi}] for six neighboring track sections when a train is moving through them

From the above analysis, it can be seen that the track section status based on UGW signal can be recognized by using the features [V_{rmsi} F_{pi}]. Furthermore, by using the temporal and spatial dependencies between the features, additional information can be provided for the status recognition and classification, which makes the classification more accurate.

3.3   Track Status Identification and Classification based on RNN

In the track breakage monitoring network, the temporal and spatial dependencies of features [V_{rmsi} F_{pi}] for each track section will not explicitly embedded in the network. Thus, a suitable network structure needs to be established, and this network structure can learn the dependencies between these data according to the input information. To detect temporal dependencies, RNN is a good choice for cyclic connections in RNN allow to store memories related to previous events.

Taking six sections as an example, Fig. 3-28 shows the status classification process by RNN for Rail 2. According to the previous description, the values V_{rmsi} and F_{pi} are calculated for every 20ms long UGW signal window and for each track section i. The features [V_{rmsi} F_{pi}]$_{tj}$ are used as the inputs for the RNN, i represents the section, and j represents the time. Through the RNN processing, the output layer of the network consists of 18 track status classification units, each three belonging to a track section i and denoting the three statuses mentioned before: free, occupied and broken. The structure of the two layers RNN network is shown in Fig. 3-29, where N represents the number of cells used in each layer.
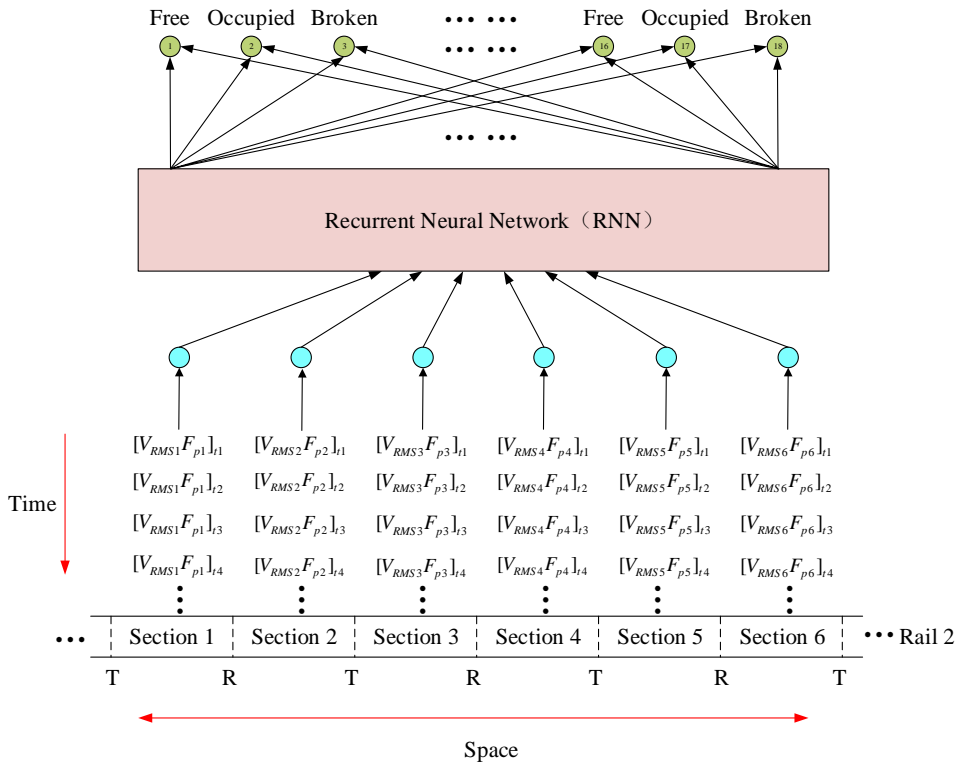
Fig. 3-28 The process of track status determination
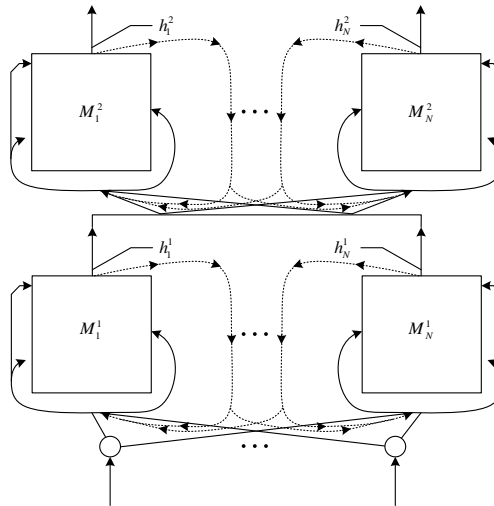
Fig. 3-29 The two layers RNN network structure

Based on the process of track status determination, this work takes six sections as an example, each section has 200 sets of features (t_1 to t_{200}), and 1200 sets of features in total are the input of RNN. Among 1200 sets of features, 80% is used for the training of RNN, and 20% is adopted for testing the network.

Firstly, RNN is configured to achieve the optimal classification effect for the input features. Tab. 3-3 shows the accuracy of the final output classification result under different RNN parameter configurations. Among them, learning rate refers to the magnitude of updating network weights in the optimization algorithm, and different optimization algorithms determine different learning rates. Excessive learning rate may lead to non-convergence of the mode, and the losses oscillate up and down; on the other hand, too small learning rate will lead to slow convergence rate of the mode, which requires longer training. The number of iterations refers to the number of times the whole training set is input to the neural network for training. When the difference between the test error rate and the training error rate is relatively small, the current iteration number is considered to be appropriate. Batch size is the number of samples sent into the model during each training of neural network. In RNN, large batch size usually makes the network converge faster, but due to the limitation of memory resources, large batch size may lead to insufficient memory or kernel crash. The number of LSTM units, which is equivalent to the number of nodes in the hidden layer of the feedforward neural network, determines the complexity of the network model. The number of units is large, the network complexity is high, and the data fitting ability is strong. The number of units needs to be adjusted according to the actual sample. Data preprocessing is carried out before data input, and the optimization of input data can also improve the final classification results.

It can be seen from Tab. 3-3 that the difference between number 1 and 2 is, whether the data are pre-processed or not, and the input data processed by normalized pre-processing method plays a greater role in improving the final classification accuracy of the network; comparing the parameters of number 2 and 3, number 3 increases the number of iterations, and the accuracy of final determination is improved. The difference between number 3 and 4 lies in the difference of learning rate. Number 4 increases the learning rate, and the classification accuracy of the network is improved. Number 5 increases the number of iterations on the basis of number 4, but the final accuracy is the same as number 4. Number 6 increases the number of LSTM units on the basis of number 4, which makes the network more complex, but does not have any positive impact on the final classification accuracy. Therefore, through analyzing the six groups of network parameters in Tab. 3-3, this work chooses the setting of number 4. Under this setting, the network training takes less computing resource, runs fast, and can get a better classification accuracy. That is, the number of LSTM units used in this research is 128, i.e. $N = 128$ in Fig. 3-29.

From Tab. 3-3, only the classification accuracy of the track status for six sections can be obtained, the classification effect cannot be directly observed. The classification result under the setting of number 4 is depicted in Fig. 3-30, the classification result is a point cloud structure represented by several three-dimensional coordinates, each point representing a track status. However, the effect of classification cannot be observed directly from Fig. 3-30, and no obvious boundaries between different classes can be obtained. So, the result shown in Fig. 3-30 is displayed on the two-dimensional surface by using t-SNE algorithm, and the effect after the dimensionality reduction is shown in Fig. 3-31. It can be observed that there are clear boundaries among the three track statuses, most of which can be accurately identified.

Tab. 3-3 RNN network parameter configuration and the classification accuracy

Parameter / Number	Learning rate	Iterations	Batch size	LSTM units	Data pre-processing	Accuracy
1	0.001	10000	10	128	Non-normalization	82.08%
2	0.001	10000	10	128	normalization	97.08%
3	0.001	20000	10	128	normalization	98.33%
4	0.01	20000	10	128	normalization	98.75%
5	0.01	40000	10	128	normalization	98.75%
6	0.01	20000	10	256	normalization	98.33%
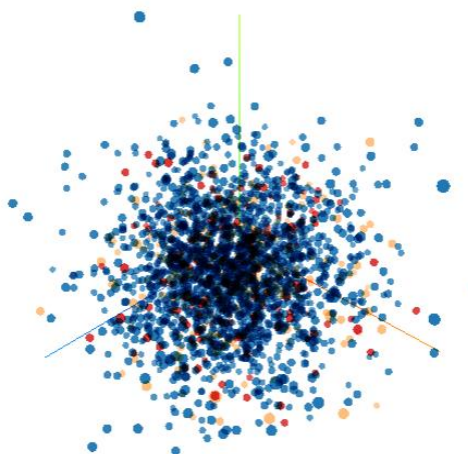
Fig. 3-30 The three-dimensional classification result for track status
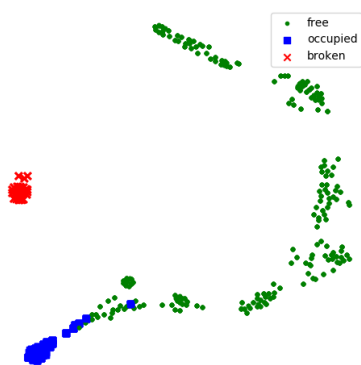
Fig. 3-31 The two-dimensional classification result for track status

It should be noted that no matter which track section status is obtained by the network of Rail 2, the final status of the corresponding section should be determined according to the output of Rail 1 and Rail 2 networks at the same time, and the final classification result is decided in accordance with safe rail operation. Tab. 3-4 shows how to determine the final status for a certain track section i.

Tab. 3-4 The final status determination for corresponding track section

Status of section i in Rail 1	Status of section i in Rail 2	Final status of section i
Free	Free	Free
	Occupied	Occupied
	Broken	Broken
Occupied	Free	Occupied
	Occupied	Occupied
	Broken	Broken
Broken	Free	Broken
	Occupied	Broken
	Broken	Broken

For the track breakage monitoring network based on UGW signal, the classification of track status in each section mainly depends on the features [V_{rmsi} F_{pi}], which are obtained by processing the received signals at the receiver end of each track section. The wireless communication module transmits the features to the remote monitoring center which served with RNN. According to the test results of RNN, the monitoring center gets the track status of all sections within the monitoring covered area in real-time. Once the track breakage is detected, it will alarm immediately and arrange the maintainer to fix the corresponding section in time. Thus, in the process of estimating the track section status, the track breakage is detected, and the detection result has high accuracy.

3.4   Conclusion

In order to overcome the shortcomings of the existing denoising methods for UGW signal, this chapter proposes a method of using VMD algorithm to filter the interference in the UGW signal; extracts the features of the UGW signals in different track status, utilizes the temporal and spatial dependencies of the extracted features and puts forward an algorithm for determining and classifying the track section status by using RNN. The simulation and experiment results show that the VMD algorithm is effective to filter the noise in UGW, and can obtain the reconstructed signal correctly. The feature extraction method can obtain two features [V_{rmsi} F_{pi}], which have great difference under different track status. Using these features as the input of RNN, the high classification accuracy and the clear boundary classification effect can be obtained.

4 Study on Improved Track Breakage Detection System and Related Electrical Model

In view of the situation that the UGW signal cannot propagate through the track breakage maintenance structure, and the previous track breakage detection system based on UGW signal in the repaired track section cannot continue to work normally. This chapter proposes an improved track detection system combining UGW signal with the electrical signal, at the same time, the corresponding electrical simulation models of single and parallel railway lines for electrical signal transmission are also proposed.

4.1　Structure for Improved Track Breakage Detection System

Based on the previous UGW-based track breakage detection system, the structure for the improved track breakage detection system can be observed in Fig. 4-1, it mainly includes power supply unit, signal transmitter and receiver, monitoring center, as well as communication unit. The distance for the signal transmission is still 1km, that means, in the improved system, transmitters and receivers are placed alternately in a 1km track section. All the transmitters and receivers are connected with two rails (Rail 1 and Rail 2) by customized transducers. In general situation, the track is complete and without breakage, the detection part based on UGW signal in transmitters and receivers work in the same way as the previous UGW-based detection system mentioned in Chapter 3. Once the track breakage maintenance structure occurs, the detection part based on UGW signal stop working. The transmitter in the corresponding section turns to the detection part based on the principle of track circuit. In other words, it uses the same transducer to transmit electrical signals instead of the original UGW signals. For one receiver can obtain signals come from its adjacent sections, the corresponding receiver turns on the operating mode of UGW signal and electrical signal in parallel. Thus, an improved track breakage detection system is realized, which is mainly based on UGW signals and supplemented by electrical signals. Compared with the previous system which only uses UGW signal for track breakage detection, the improved one can adapt to the complex track conditions, the detection efficiency and the working life are enhanced. The detection part based on the principle of track circuit generate the electrical signal by the processor at the transmitter end. Through the ADC and power amplifier, the electrical signal connected to the tracks by transducers. In the receiver end, the same kind of transducers is used to receive electrical signals, and these signals are sent to ARM core-board for algorithm processing. In order to determine whether a track breakage occurs, the servers in remote monitoring center

detects the status of each track section according to the information transmitted from communication units in transmitter and receiver end. When the track breakage is detected, the monitoring center will send the alarm information and the location of corresponding alarm track section to relevant workers for timely maintenance.
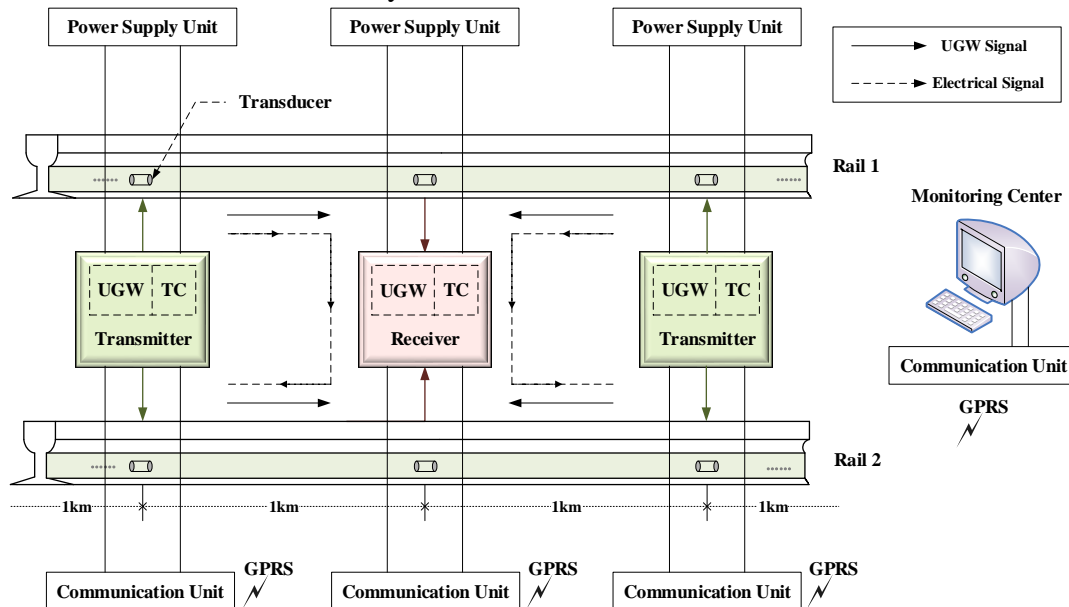
Fig. 4-1 Structure for the proposed track breakage detection system

4.1.1 Transmitter

The transmitter in improved track breakage detection system is composed of UGW transmit device and track circuit transmit device. The structure of UGW transmit device keeps as same as the previous one; whereas, for the track circuit transmit device, the transmitted electrical signals are generated by ARM core-board, after digital-to-analog converter (DAC), these signals are adjusted via pre-amplifier and power amplifier, the electrical signals are connected to tracks by the ground wire of transducers after isolation transformer. The structure of transmitter is shown in Fig. 4-2, where the switches 1 and 2 present isolated control for UGW signals and electrical signals. For a transmitter, when its two adjacent track sections are complete, switch 1 is on and 2 is off, only the part based on UGW signals works; when a breakage maintenance occurs in any of the adjacent sections, switch 1 and 2 are on, the UGW part and the track circuit part of the transmitter work at the same time; once the two adjacent sections are broken at the same time, switch 1 is off and switch 2 is on, only the track circuit part works, but the probability of this situation is very small.
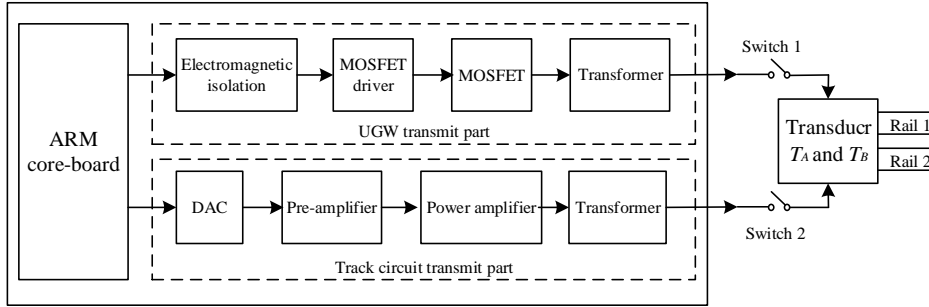
Fig. 4-2 Structure for the transmitter of proposed track breakage detection system

4.1.2 Receiver

Corresponding to the transmitter, the receiver is also composed of UGW part and track circuit part. The receiver part based on UGW signals has the same structure as the previous UGW-based breakage detection system. For the track circuit receiver part, the electrical signals are introduced to the receiver by transducers, and then through the pre-processing by isolation transformer, pre-amplifier, as well as the band-pass filter to get the cleaner receptions. After pre-processing, through the ADC, the sampling signals are sent to ARM core-board for further processing. The receiver structure can be observed in Fig. 4-3. Corresponding to the switches in the transmitter, when the two neighboring sections are complete, the switch 1 is on and 2 is off, the detection part based on UGW signal works; when any of the adjacent section is broken, switches 1 and 2 are on simultaneously, and the UGW-based and track circuit-based detection parts work at the same time; once the two neighboring sections are broken at the same time, switch 1 is off, and 2 is on, only the track circuit-based detection part works.
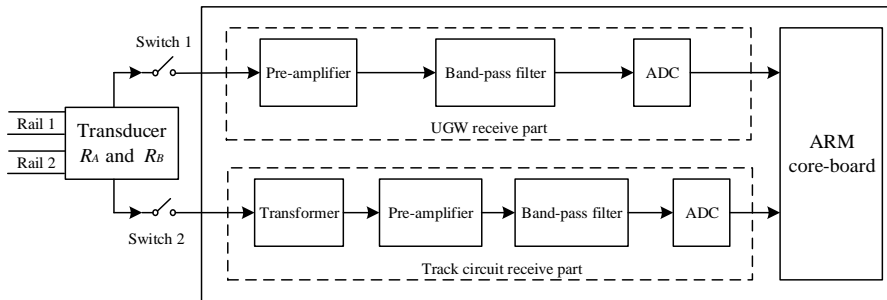
Fig. 4-3 Structure for the receiver of proposed track breakage detection system

4.1.3 Power Supply Unit

For the previous UGW-based detection system, even though it has low power consumption, which is within 5W in the average, in the condition of long-time rainy season or in the place with short illumination time, the solar power supply unit is not enough to support the detection system. Thus, to solve this problem, in the novel improved UGW-electrical proposal, a new power supply unit is adopted.

This new 24V power supply unit consist of one 150W solar panel, two 12V-50Ah storage batteries, as well as a controller which can be used to control the charging and discharging of solar panel. The charging peak voltage of 150W solar panel is around 18V, and the peak current is about 8.5A. It has been tested that two batteries can be filled in 13 hours in sunny conditions, and the charging current can reach 7.5A. In rainy weather, the charging current can reach 2A. When two batteries are fully charged, the system can properly and continuously work for more than 10 days, this ensures the track breakage detection system can be normally used in most areas of China. And also, for waterproof, anti-freezing and prevention of thievery, the storage batteries have been buried underground, this method can improve the service life of batteries. The power supply unit for each transmitter or receiver node is shown in Fig. 4-4.

Fig. 4-4 Power supply unit for each node of track breakage detection system

4.1.4   Design and Installation of Transducer

The sandwich piezoelectric ultrasonic transducer (SPUT) is adopted in the previous UGW-based track breakage detection system, it achieves the purpose of energy conversion by piezoelectric ceramic, piezoelectric film, quartz, as well as other device which have piezoelectric effect. The electro-mechanical conversion effect of SPUT is high, it is easy to design and realization, the cost is low.

Whereas, for the proposed improved detection system, the detection principles of the UGW signal and electrical signal are different. Among them, UGW-based one uses mechanical vibration to spread signal in the track, while the electrical-based one uses electrical signal. Therefore, in order to use the same transducer to transmit UGW signals and electrical signals, and to ensure their compatibility in installation, the design of ultrasonic transducer needs to be improved. The improved customized transducer can be observed in Fig. 4-5. It consists of front and back metal cover plate, prestressed bolt insulation pipe, metal electrode plate, piezoelectric ceramic piece and prestressed bolt. Due to the sandwich structure, piezoelectric ceramic will not

be broken easily, and the frequency stability and temperature stability of the transducer are improved.

(a) Internal structure diagram of SPUT   (b) External structure diagram of SPUT
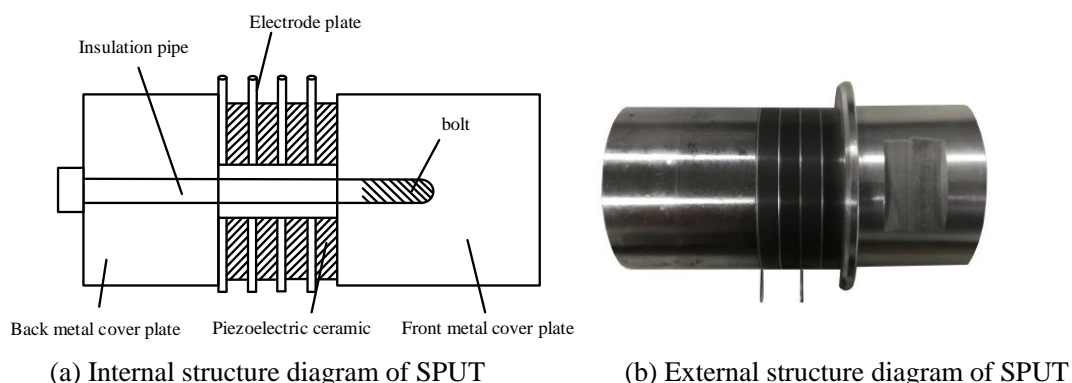
Fig. 4-5 Structure for sandwich piezoelectric transducer

After the internal structure of the transducer meets the requirements of UGW signal transmission, the transducer is packaged with a metal shell, which makes the ground wire not only connected with the negative pole of piezoelectric ceramic, but also connected with the metal shell. Thus, when the track circuit-based detection part works, the electrical signal can be transmitted to the track through the ground wire by the metal shell of the customized transducer. The package diagram for customized transducer is depicted in Fig. 4-6.
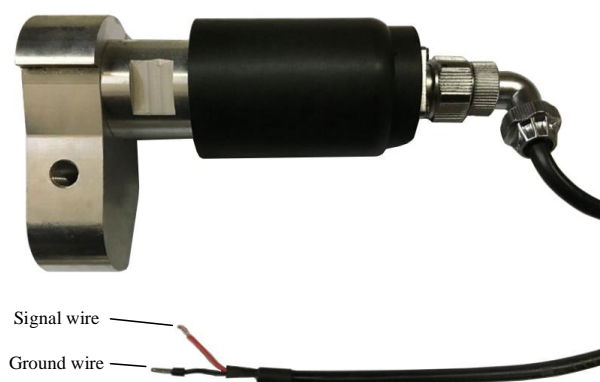
Fig. 4-6 Package diagram for customized transducer

In order to install the customized transducer on the track, and the installation will not affect the normal running of the train, Fig. 4-7 shows the stable installation of the transducer on the rail waist by a custom fixture. Through the transducer, the transmission of UGW signal and electrical signal can be achieved by a common equipment. When UGW signals are adopted for track breakage detection, signal wire and ground wire are connected with the detection device at the same time, and the electric to acoustic signal conversion or acoustic to electric signal conversion are conducted through the piezoelectric ceramic plate inside the transducer. Whereas, only the ground wire of the transducer is used to connect with the detection device, and the electrical signal transmission is conducted by the metal shell of the transducer when the track circuit-based

detection part works. Therefore, the improved detection system only needs to switch the corresponding switch to realize the conversion of two track breakage detection methods, which avoids the extra installation of sensors for electrical signal, and this system achieves high engineering practical value.

Fig. 4-7 Installation diagram of customized transducer

4.1.5 Communication Unit

In the improved detection system, the General Packet Radio Service (GPRS) module and the wireless data transmission module are selected for the real-time information transmission between the remote monitoring center and the track breakage detection transmitter or receiver.

Both GPRS module and wireless data transmission module use broadcast mode to communicate with other modules. That means, any device in the region transmit a signal, all the other devices in the same region can receive it. Therefore, in order to realize point to point communication between different equipment, as well as between equipment and server, each one has a unique identification (ID) when it works. The server and each detection equipment can realize point to point communication with other devices by identifying the ID. The communication mode for the improved track breakage detection system can be observed in Fig. 4-8, all equipment is divided into three types according to the communication mode, which are independent equipment, terminating equipment, as well as data transmission equipment. Among these three types, data transmission equipment only carries wireless data transmission modules, which are installed in areas that cannot be covered by GPRS network, and it transmits information to each other in the form of "relay". Whereas, the communication between data transmission equipment and the server depends on the terminating equipment, which is the first device located in the cover area of GPRS network. The terminating equipment carries both the GPRS module and the wireless data transmission module. Beside to communicate itself data with remote server, it is also responsible for transmitting the data from other data transmission equipment to the server. Take the example marked in Fig. 4-8, when the server needs to communicate with device No. 6,

the ID of device No. 6 and the information it carries must be transmitted to terminating equipment No. 3 together through GPRS module. After receiving confirmation that the server is communicating with the device No. 6 (not itself No. 3), the ID number of device No. 6 will be set as the destination number, the data to be communicated will sent through the data transmission equipment, and then finally transmitted to the device No. 6 through the form of "relay". In addition, independent equipment refers to devices installed in the coverage area of GPRS network, it only carries GPRS module, which can directly communicate with server.
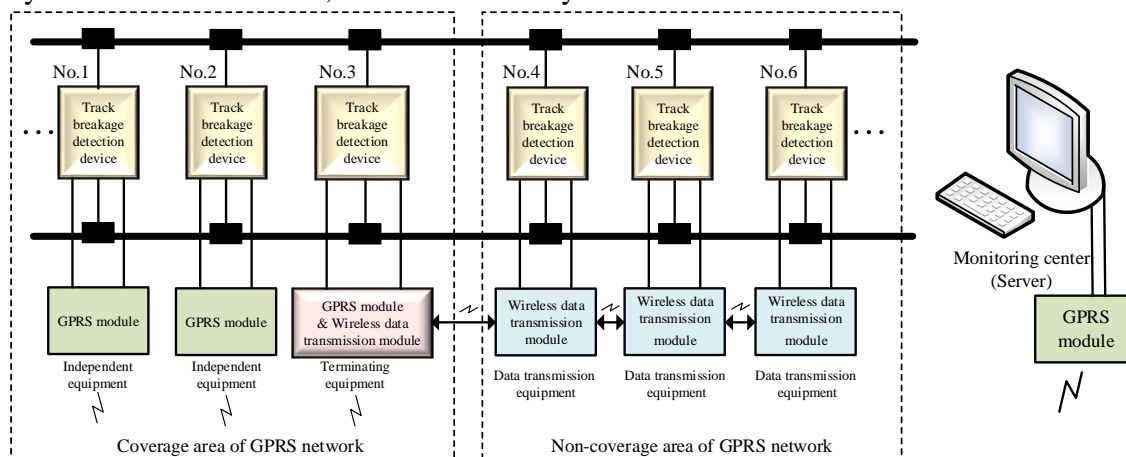
Fig. 4-8 Communication mode for track breakage detection system

4.2   Electrical Model for a Single Railway Line

For track circuit, through two rails, the electrical signals are transmitted from transmitter to receiver, thus actually forms a two-port track network for signal transmission. Due to the resistant R and inductance L of track, leakage capacitance C between two rails, as well as leakage conductance G between two rails are uniformly distributed along the railway direction, which are usually represented by the values of 1km. And also, the geometry, relative position and surrounding condition of the two rails that make up the two-port track network are basically unchanged for the whole railway, so the tracks can be analyzed by using the uniform transmission line theory. In some cases, when the track circuit works, the leakage impedance of rail to ground can be neglected, for the current of the two rails is balanced with each other. Only the leakage impedance between two rails should be taken into consideration. In addition, in practical track circuits, the transient components of the signal attenuate rapidly, so the steady-state solution of track circuit is researched only. Base on the assumptions mentioned above, the electrical simulation models for the track circuit part of the improved track breakage detection system are proposed. Not only the simulation model for a single railway line is considered, but also the model for two neighboring parallel lines with electromagnetic coupling under different humidity conditions are proposed.

According to the aforementioned structure of track circuit part in the improved track breakage detection system, the simulation model for a 1km single railway line is established in Simulink software, the structure for this model is shown in Fig. 4-9, it consists of transmitter, receiver, cable, transformer and track. For the 1km track section, in order to analyze the influence caused by transmission distance, the track breakage position, as well as the train shunt position, the 1km track section is divides into ten cascaded 100m sub-sections. The transmitter is composed of a voltage source and a .mat file which stores the signal data to be sent, on the other hand, the receiver consists of a voltage measurement unit a .mat file that can store the received signal data.
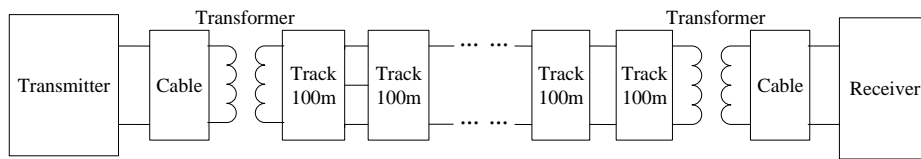
Fig. 4-9 Structure for a single railway line simulation model

A. Cable model

For the improved track breakage detection system, the cable connected between the transmitter and the transformer is the same as the one used between the receiver and the corresponding transformer. These links can be modelled as a quadrupole (two-point device) network, which should take into account propagation parameters, weather conditions, bandwidth, etc. The model has been implemented according to Fig. 4-10, where the values of the parameters are: $R_c=45\pm2.0\Omega$/km, $L_c=750\mu$H/km and $C_c=28\pm3$nF/km, and these values come from the cooperation company. A distance of 100m SPT digital cable is adopted for this connecting cable.

According to the cable model and the relevant circuit knowledge, the transfer matrix of this model can be expressed as equation (4-1), where, $z_1=1/(R_c+j\omega L_c)$, $z_2=j\omega C_c$, and ω represents for the angular frequency of the transmitted signal.
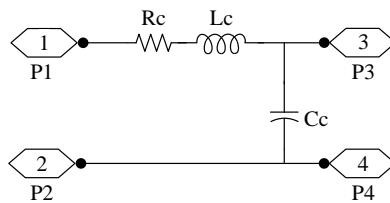
Fig. 4-10 Model used for the connecting cable at the transmitter and the receiver

$$T_c = \begin{bmatrix} 1+\dfrac{z_2}{z_1} & \dfrac{1}{z_1} \\ z_2 & 1 \end{bmatrix} \tag{4-1}$$

B. Transformer model

Due to the high internal impedance of the transmitter and the low impedance of track, in the process of signal transmitted from transmitter to tracks, the impedance mismatch will lead to the attenuation at the transmitter end, further results in the reduction of rail surface voltage. The

purpose of transformer is to make the internal impedance of the transmitter matches the impedance of the track. On the other hand, if the signal generated by transmitter is high, which in order to reduce the attenuation in the transmitter end, the voltage received in track needs to be low, thus to solve the problem that high voltage in tracks may affect the occupied status and broken status. At the receiver end, the rail surface voltage is stepped up through the transformer, in order to reduce the attenuation at the receiver end, and to obtain a slightly higher voltage. The transformer model in the transmitter end can be observed in Fig. 4-11, it consists of two reversed connected capacitance C1 and C2, a transformer whose ratio is n:1, as well as two induction coils L. Points P1 and P2 are connected with cable, while points P3 and P4 are connected to tracks.
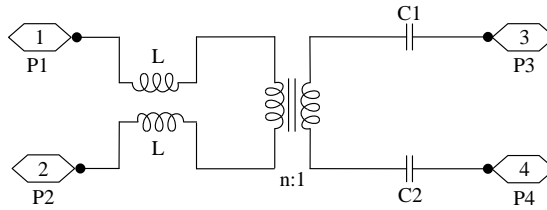
Fig. 4-11 Model of the transformer at the transmitter end

According to the transmission line equation, the equivalent coefficient T_{trans} of two-port network can be obtained in (4-2), where L_{trans} is the value of inductance L, C_{trans} is the value of capacitances C1 and C2. The structure of the transformer both in transmitter and receiver is the same, while the signal transmission direction is opposite. For the transformer in the receiver end, the equivalent coefficient $\overline{T}_{trans}$ of the two-port network is similar with the one in the transmitter end, only to exchange the two elements on the main diagonal of (4-2), which can be expressed as equation (4-3).

$$
T_{trans} = \begin{bmatrix} n & \dfrac{j\omega L_{trans}}{n} + \dfrac{2}{j\omega C_{trans}} \\ 0 & \dfrac{1}{n} \end{bmatrix}
\tag{4-2}
$$

$$
\overline{T}_{trans} = \begin{bmatrix} \dfrac{1}{n} & \dfrac{j\omega L_{trans}}{n} + \dfrac{2}{j\omega C_{trans}} \\ 0 & n \end{bmatrix}
\tag{4-3}
$$

C. Track model

Based on the transmission line theory, a railway track can be modelled as an electrical network formed by a combination of distributed parameters. The distributed parameters are used to represent a track section as a track transmission line model. For a specified track circuit, the characteristic parameters are a serial resistance and inductance, together with a parallel capacitance and conductance. The capacity and the conductance are strongly affected by the track

construction (ballast) and the environmental conditions, such as the weather and soil conditions. A symmetric two-port model has been also used here to represent a track section. Furthermore, the length of the section has been considered as a cascade of identical subsections. Fig. 4-9 already showed a 1km long track section, approximated by 10 equal subsections, whereas the model for every 100m long subsection is shown in Fig. 4-12. The parameters for resistance R_t (Ω/km) and inductance L_t (H/km) represent the rail impedance, whereas the conductance G_t (S/km) and capacitance C_t (F/km) mean the track shunt admittance. Every set of these four parameters is defined per unit length, and some of these parameters can be obtained by measurements [95]. These four parameters for resistance, inductance, conductance and capacitance for each 100m are represented by R_{t100}, L_{t100}, G_{t100} and C_{t100}, respectively. It's two-port equivalent coefficient can be expressed as (4-4), where, $z1 = 1/(R_{t100}/2 + j\omega L_{t100}/2)$, and $z2 = G_{t100} + j\omega C_{t100}$.
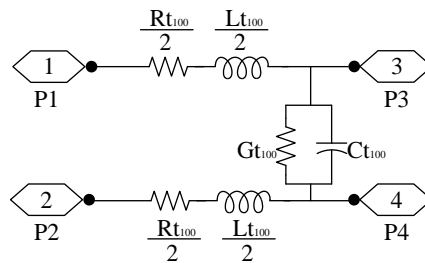
Fig. 4-12 Model of the track per 100m

$$T_{\text{track}} = \begin{bmatrix} -2\dfrac{z_2}{z_1} & -\dfrac{2}{z_1} \\ -z_2 & -1 \end{bmatrix} \tag{4-4}$$

4.3   Electrical Model for Parallel Railway Lines

Usually, the track is laid on the ballast, the change of weather environment around the track has a great influence on the parameters of the ballast, which leads to a large leakage current and causes interference to the adjacent railway line. Thus, the electrical signals generated by transmitter can be sent not only through the railway line, but also through the ground to adjacent parallel lines. For the receiver, it can also receive signals from its own transmission channel and neighboring railway lines. The track itself shows the inductive impedance, if the frequency of the electrical signals transmitted in the track is high, for the long-distance transmission, there will be mutual inductance between adjacent lines. In this work, low-frequency signals are selected for the track circuit-based detection part in the improved system. Therefore, mutual inductance between adjacent lines is ignored in the simulation analysis, only the influence of ground on signal transmission is taken into account. The leakage situation of rail to ground is depicted in

Fig. 4-13. And the simulation model structure for two parallel railway lines can be observed in Fig. 4-14, in which the internal structure for single railway line is the same as the structure mentioned in Chapter 4.2, and the coupling represents the interaction between Line 1 and 2.
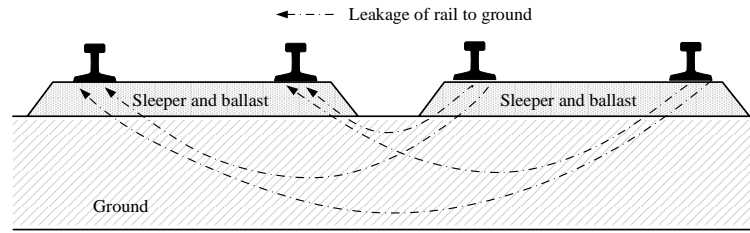
Fig. 4-13 Leakage situation of rail to ground
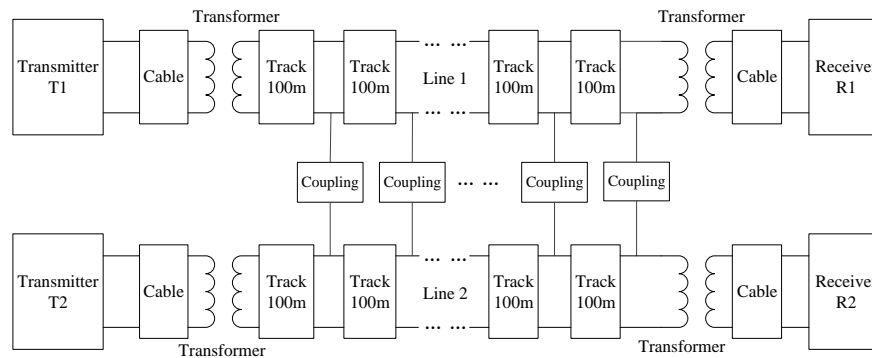
Fig. 4-14 Simulation model structure for two parallel railway lines

For the model described in Fig. 4-14, first to take the influence of earth conductivity in it. The earth conductivity mainly dependent on the status of the ballast, humidity, dirt, temperature, as well as the covered vegetation. It is important for the determination of the conductance value, and it shows a fairly large range of values: any values between 0.01mS/m and 100mS/m are usually selected, which covering almost all the environmental conditions and geological types [96]. At same time, abundant data are interpolated by equitation (4-5), and these data represent for the calculation of the ground conductance ρ as a function of the frequency and water content. W stands for dimensionless water content, f is the frequency, and the three coefficients are k_1=0.842, k_2=1.435, k_3=0.072, respectively [97].

$$\rho = k_1 W^{k_2} f^{k_3} \qquad\qquad (4\text{-}5)$$

According to equation (4-5), for different water content, the relationship between conductivity and frequency is shown in Fig. 4-15. As can be observed from this figure, under the same water content condition, the effect of frequency change on conductivity is very weak and can be neglected. Less water content indicates that the track is under high temperature and dry conditions, and the increase of water content means that the track is working under rainy or humidity environment.
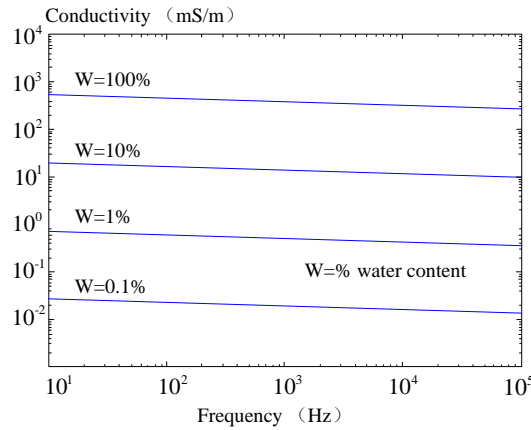
Fig. 4-15 Relationship between frequency and conductivity under different water content [96]

Next, consider the effect of soil permittivity. The soil permittivity is not constant, it increases with decreasing frequency, and strongly changes with frequency, temperature, humidity and so on. This behavior may be caused by the solid particles, water, and air voids in soil. Even though the frequency variation of the permittivity and its upper limit are relatively independent on the soil type, the permittivity depends on the amount of water and increase with the volume fraction of water is similar for different soil types. The permittivity of pure water is larger than 80, while the conductivity is 0; dry soil has a typical permittivity of 3.5 and a conductivity of 10mS/m. The data which represent for the calculation of the ground permittivity ε as a function of the frequency and water content are interpolated by equitation (4-6), in which the W represents water content, expressed as a form of percentage, f is frequency in Hz, and the three constant coefficients are $h_1=28370$, $h_2=0.774$, $h_3=-0.59$ respectively [96].

$$\varepsilon = h_1 W^{h_2} f^{h_3} \tag{4-6}$$

According to equation (4-6), the relationship of soil permittivity with frequency and water content can be observed in Fig. 4-16. As can be seen from it, the soil permittivity is closely related both to the change of frequency and change of water content.
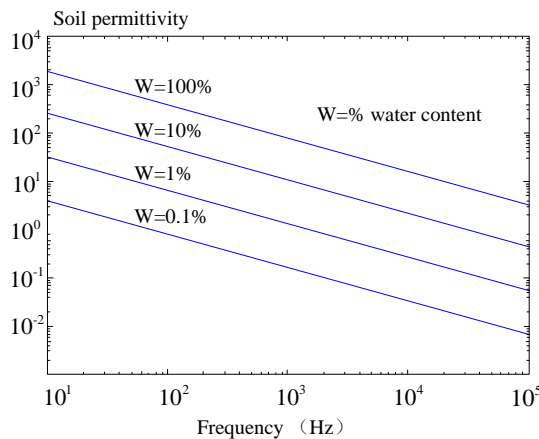
Fig. 4-16 Relationship between frequency and permittivity under different water content [96]

To sum up, the coupling model between two adjacent parallel railway lines for each 100m distance in this work is shown in Fig. 4-17, where the change of G_{ground} value reflects the influence of conductivity, and the value of C_{ground} represents the variation of soil permittivity.
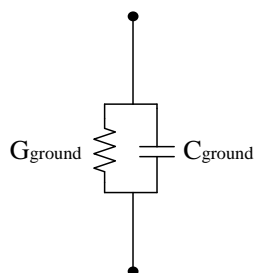
Fig. 4-17 Model for coupling between two near parallel railway lines

4.4   Conclusion

In order to solve the problem that when the track breakage maintenance structure occurs, the UGW signals cannot propagate through this structure and the previous UGW-based track breakage detection system cannot continue to be used in the corresponding section, an improved UGW-electrical mixed track breakage detection system is proposed in this chapter. The improved system is not only compatible with the transmission and processing of UGW signals and electrical signals, but also the performance of power supply units, communication units, as well as other parts in the system have been greatly improved. The improved system can cope with more complex running environment for a train. At the same time, aiming at the track circuit-based part in the improved system, electrical simulation models for a single railway line, as well as for the parallel two railway lines are proposed. In particular, the coupling between two adjacent parallel railway lines under different water content is discussed. These two electrical simulation models provide an appropriate simulation platform for the subsequent analysis of the transmitted electrical signals in track.

5 Electrical Signal Transmission and Detection Algorithm for the Improved System

For the track circuit-based part in the improved track breakage detection system, an electrical signal transmission method using spread spectrum communication for reference is put forward in this chapter. Spread spectrum sequences are adopted in the proposed transmission method. And a novel adaptive peak detection algorithm is also proposed based on the characteristics of the received signal in the new transmission scheme. By identifying the peak values of six continuous periodic signals, the track status of the detected section can be determined.

5.1　Study on Electrical Signal Transmission

The spread spectrum sequences have the properties of high auto-correlation itself, as well as the low cross-correlation with other sequences. To utilize the properties in the signal transmission can obtain high transmission gain, suppress the noise, and reduce multipath interference from other signal sources, etc. Thus, a novel electrical signal transmission scheme which can be applied in the improved track breakage detection system is proposed. Based on the four sets of spread spectrum sequences *Kas*(4,4,15), *Kas*(6,8,63), *LS*(4,19,3) and *LS*(8,71,7), the performance of the four sets is compared by using the simulation model aforementioned and the concept of correlation bound proposed here. Through the comparison, the sequence used for the electrical signal transmission in this work is determined.

5.1.1　Sequence Selection

Kas(4,4,15) is a set of four Kasami sequences with a period length of 15, and this set is described in detail in Tab. 5-1. Sequences No. 1 and 3 are selected for the study, and they are denoted as Kas15_1 and Kas15_3 respectively, these two sequences can be seen from Fig. 5-1. The ACFs for sequence Kas15_1 and Kas15_3 themselves, as well as the CCFs between these two sequences are shown in Fig. 5-2. As can be seen from the ACF signals, 15-bit Kasami sequences have obvious ACF peaks, and though the CCF signals which represent the multipath interferences are not very small, the useful signals transmitted can still be recognized. It should be noted that different sequences in the same set with the same period length have different auto-correlation performances, that is to say, the anti-noise performances are variable from each other.

Tab. 5-1 15-bit Kasami sequences

No.	Sequence
1	-1 -1 1 1 -1 1 1 1 -1 -1 -1 -1 1 -1 1
2	1 -1 1 -1 -1 -1 -1 1 1 1 -1 1 -1 -1 -1
3	-1 1 -1 1 1 -1 1 -1 1 -1 1 1 1 1 -1
4	1 1 1 -1 1 1 -1 -1 -1 1 1 -1 -1 1 1

Fig. 5-1 Two 15-bit Kasami sequences

Fig. 5-2 Auto- and cross- correlation signal for two 15-bit Kasami sequences

For the sake of determining the effect of the same sequence on the signal transmission performance under different period lengths, a set of Kasami sequences with the period length of 63 is introduced. This set of sequence can be observed in Tab. 5-2, and it can be denoted as *Kas*(6,8,63). Two sequences No. 1 and 4 are selected here, they are represented by Kas63_1 and Kas63_4, respectively. From Fig. 5-3, these two sequences can be observed in detail. Their respective ACFs, as well as the CCFs between these two sequences are shown in Fig. 5-4. Compared with the situation in Fig. 5-2, it can be observed that with the increase of the sequence length, the amplitude of ACF peak increases, the effective signal are more likely to be extracted from disturbances.

Tab. 5-2 63-bit Kasami sequences

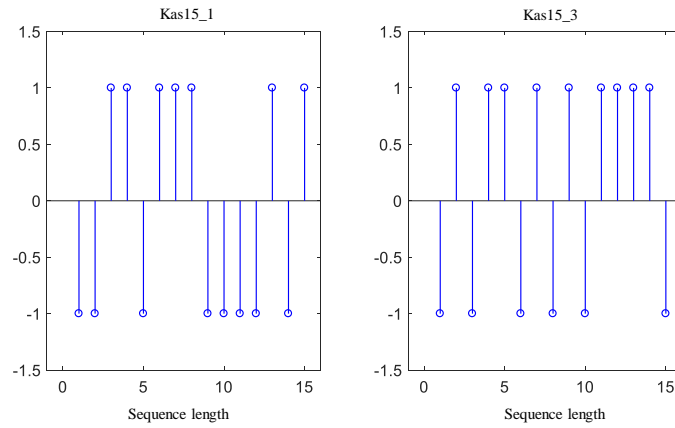| No.	Sequence
1	1 -1 1 1 -1 -1 -1 1 1 1 -1 1 -1 -1 -1 -1 1 1 -1 1 -1 1 1 1 -1 -1 1 1 1 1 -1 1 1 1 1 1 -1 -1 -1 -1 -1 -1 1 -1 1 -1 1 -1 -1 1 1 -1 -1 1 -1 -1 -1 1 -1 -1 1 -1 1
2	1 -1 -1 1 1 1 1 1 1 -1 -1 -1 1 1 -1 -1 -1 1 1 -1 1 1 1 -1 -1 1 -1 -1 1 1 1 1 -1 -1 -1 1 -1 1 -1 1 1 1 1 - 1 -1 -1 -1 1 1 1 1 1 -1 -1 1 1 -1 1 1 -1 -1 1 -1
3	1 1 1 -1 1 1 -1 1 -1 1 1 -1 1 -1 -1 1 1 -1 1 -1 -1 1 -1 1 1 1 -1 1 1 -1 -1 -1 -1 -1 1 1 1 -1 1 1 1 -1 1 1 1 1 -1 1 -1 1 -1 -1 1 -1 1 -1 -1 -1 -1 1 -1 1 1
4	-1 -1 -1 -1 1 -1 -1 -1 1 -1 1 -1 -1 -1 1 -1 -1 -1 1 1 - 1 -1 1 -1 1 1 1 1 -1 1 1 -1 -1 1 1 -1 -1 1 1 1 -1 -1 -1 -1 -1 1 -1 -1 -1 -1 1 1 1 -1 -1 -1 1 1 1 1 -1 -1 1
5	1 1 -1 -1 -1 -1 1 1 -1 -1 1 1 -1 1 -1 1 -1 -1 -1 1 1 1 -1 -1 1 -1 1 -1 1 -1 1 -1 1 1 -1 1 1 1 1 -1 -1 1 1 1 -1 1 1 -1 1 1 -1 1 1 1 -1 1 -1 -1 1 1 1 -1 -1
6	-1 1 -1 1 -1 1 -1 -1 -1 -1 -1 1 1 -1 1 1 -1 1 -1 -1 -1 -1 -1 -1 -1 -1 -1 1 -1 -1 1 1 1 -1 1 -1 1 1 -1 -1 1 1 -1 -1 1 -1 -1 1 1 -1 -1 -1 1 -1 1 1 -1 1 -1 1 -1 1 1 1
7	-1 1 1 1 1 -1 1 -1 -1 1 -1 -1 -1 1 1 1 1 1 1 1 1 -1 - 1 1 -1 1 1 -1 -1 -1 -1 1 -1 1 -1 -1 1 -1 -1 1 -1 1 -1 1 1 -1 -1 -1 1 -1 -1 -1 -1 -1 -1 1 1 -1 -1 -1 -1 -1 -1
8	-1 -1 1 -1 -1 1 1 -1 1 1 1 1 1 1 1 1 -1 1 -1 -1 -1 1 - 1 1 1 1 -1 -1 -1 -1 1 -1 -1 1 -1 -1 -1 -1 -1 1 -1 1 1 -1 -1 1 1 1 1 1 -1 1 -1 1 1 1 1 1 1 -1 1 1 1 -1

Fig. 5-3 Two 63-bit Kasami sequences
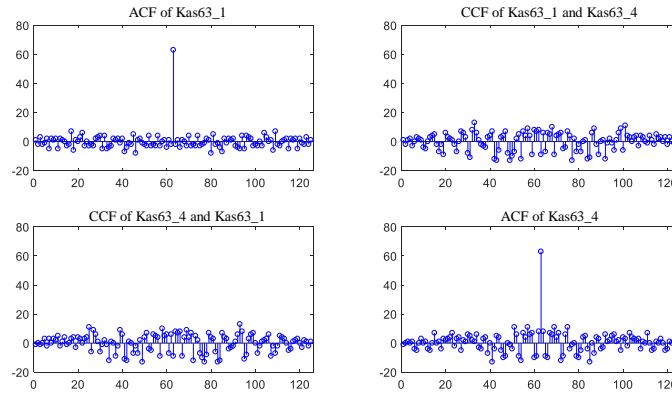
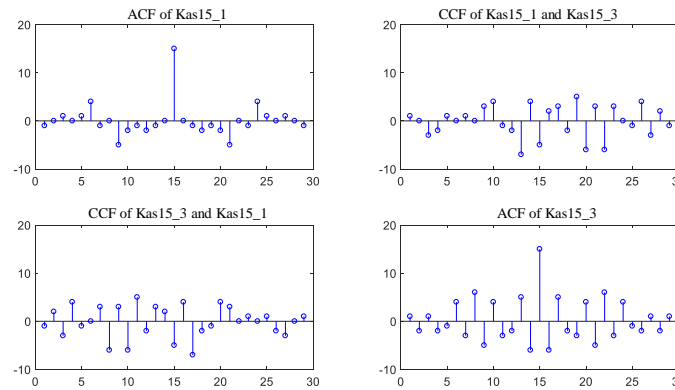Fig. 5-4 Auto- and cross- correlation signal for two 63-bit Kasami sequences

Even though in the case of similar period length of sequence, different types of spread spectrum sequence still have variable effects on signal transmission performance. A set of LS sequences $LS(4,19,3)$, which with the length of 19, can be observed in Tab. 5-3. The number of zeros inserted in the middle of each sequence is 3. Taking the sequences No. 1 and No. 3 as the examples, they are respectively denoted as LS19_1 and LS19_3, and can be seen from Fig. 5-5.

Tab. 5-3 19-bit LS sequences

No.	Sequence																		
1	1	-1	-1	-1	1	-1	1	1	0	0	0	1	1	-1	1	1	1	1	-1
2	1	-1	-1	-1	-1	1	-1	-1	0	0	0	1	1	-1	1	-1	-1	-1	1
3	1	-1	1	1	1	-1	-1	-1	0	0	0	1	1	1	-1	1	1	-1	1
4	1	-1	1	1	-1	1	1	1	0	0	0	1	1	1	-1	-1	-1	1	-1

Fig. 5-5 Two 19-bit LS sequences

Fig. 5-6 shows the ACFs of sequence LS19_1 and LS19_3, as well as the CCFs between these two sequences. As can be seen from this figure, unlike the Kasami sequence, in both ACF and CCF of LS sequence, there exists an IFW with the length of 3*2+1, 3 is the number of zeros inserted in the LS sequence. In the IFW, there is no interference, the peaks for ACF signals can

be accurately identified. While, in the external of the IFW, there are interferences with higher amplitude compared with the situation for 15-bit Kasami sequences.
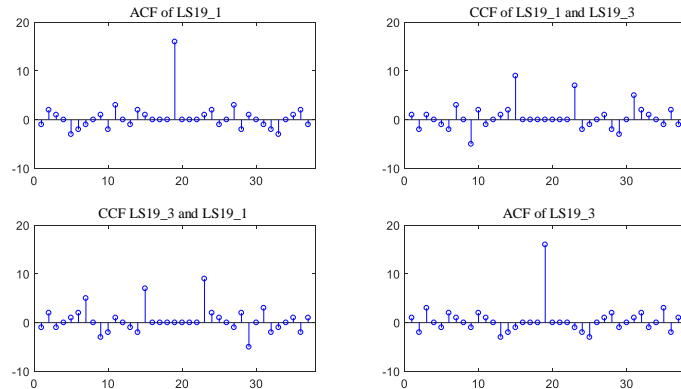
Fig. 5-6 Auto- and cross- correlation signal for two 19-bit LS sequences

Corresponding to the 63-bit Kasami sequence, the set of LS sequence $LS(8,71,7)$ with the period length of 71 is also selected, as can be seen from Tab. 5-4. In each sequence, seven zeros are inserted in the middle of them. Two sequences No. 1 and No. 3 are selected in the set, and they are represented by LS71_1 and LS71_3, respectively. Fig. 5-7 shows the two selected 71-bit LS sequences, and Fig. 5-8 is the ACFs and CCFs for these two groups of sequences. Similar to the 19-bit LS sequence, for the LS sequence with period length of 71, there is no interference in the IFW of length 7*2+1, whereas, a slightly high noise is introduced in the external of this IFW.

Tab. 5-4 71-bit LS sequences

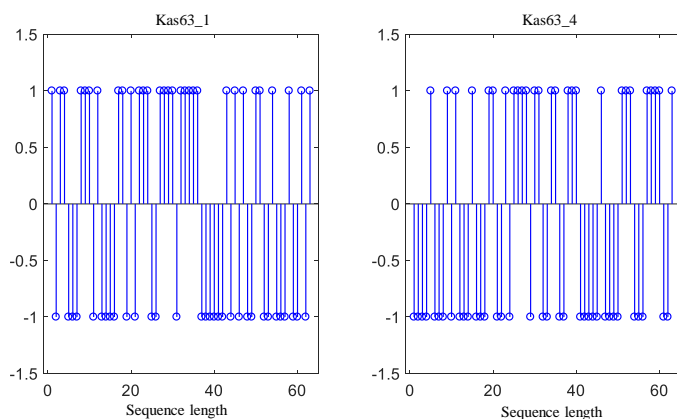| No.	Sequence
1	1 -1 -1 -1 -1 1 -1 -1 1 -1 -1 -1 -1 1 -1 -1 1 -1 -1 -1 1 -1 1 1 1 -1 -1 -1 1 -1 1 1 0 0 0 0 0 0 0 1 1 -1 1 -1 -1 -1 1 1 1 -1 1 -1 -1 -1 1 1 1 -1 1 1 1 1 -1 1 1 -1 1 1 1 1 -1
2	1 -1 -1 -1 -1 1 -1 -1 -1 1 1 1 1 -1 1 1 1 -1 -1 -1 1 -1 1 1 -1 1 1 1 -1 1 -1 -1 0 0 0 0 0 0 0 1 1 -1 1 -1 -1 -1 1 -1 -1 1 -1 1 1 1 -1 1 1 -1 1 1 1 1 -1 -1 -1 1 -1 -1 -1 -1 1
3	1 -1 -1 -1 -1 1 -1 -1 1 -1 -1 -1 -1 1 -1 -1 -1 1 1 1 -1 1 -1 -1 -1 1 1 1 -1 1 -1 -1 0 0 0 0 0 0 0 1 1 -1 1 -1 -1 -1 1 1 1 -1 1 -1 -1 -1 1 -1 -1 1 -1 -1 -1 -1 1 -1 -1 1 -1 -1 -1 -1 1
4	1 -1 -1 -1 -1 1 -1 -1 -1 1 1 1 1 -1 1 1 -1 1 1 1 -1 1 -1 -1 1 -1 -1 -1 1 -1 1 1 0 0 0 0 0 0 0 1 1 -1 1 -1 -1 -1 1 -1 -1 1 -1 1 1 1 -1 -1 -1 1 - 1 -1 -1 -1 1 1 1 -1 1 1 1 1 -1

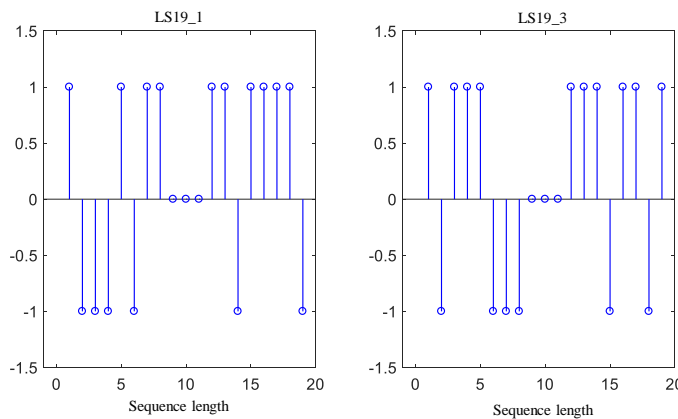| No.	Sequence
5	1 -1 -1 -1 1 -1 1 1 1 -1 -1 -1 1 -1 1 1 1 -1 -1 -1 -1 1 -1 -1 1 -1 -1 -1 -1 1 -1 -1 0 0 0 0 0 0 0 1 1 -1 1 1 1 1 -1 1 1 -1 1 1 1 1 -1 1 1 -1 1 -1 - 1 -1 1 1 1 -1 1 -1 -1 -1 1
6	1 -1 -1 -1 1 -1 1 1 -1 1 1 1 -1 1 -1 -1 1 -1 -1 -1 -1 1 -1 -1 -1 1 1 1 1 -1 1 1 0 0 0 0 0 0 0 1 1 -1 1 1 1 1 -1 -1 -1 1 -1 -1 -1 -1 1 1 1 -1 1 -1 -1 -1 1 -1 -1 1 -1 1 1 1 -1
7	1 -1 -1 -1 1 -1 1 1 1 -1 -1 -1 1 -1 1 1 -1 1 1 1 1 -1 1 1 -1 1 1 1 1 -1 1 1 0 0 0 0 0 0 0 1 1 -1 1 1 1 1 -1 1 1 -1 1 1 1 1 -1 -1 -1 1 -1 1 1 1 -1 -1 -1 1 -1 1 1 1 -1
8	1 -1 -1 -1 1 -1 1 1 -1 1 1 1 -1 1 -1 -1 -1 1 1 1 1 -1 1 1 1 -1 -1 -1 -1 1 -1 -1 0 0 0 0 0 0 0 1 1 -1 1 1 1 1 -1 -1 -1 1 -1 -1 -1 -1 1 -1 -1 1 -1 1 1 1 -1 1 1 -1 1 -1 -1 -1 1

Fig. 5-7 Two 71-bit LS sequences
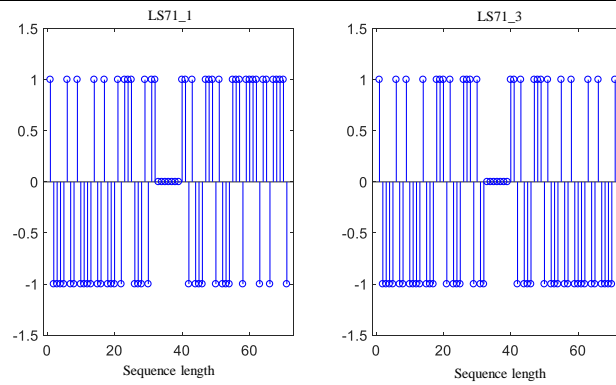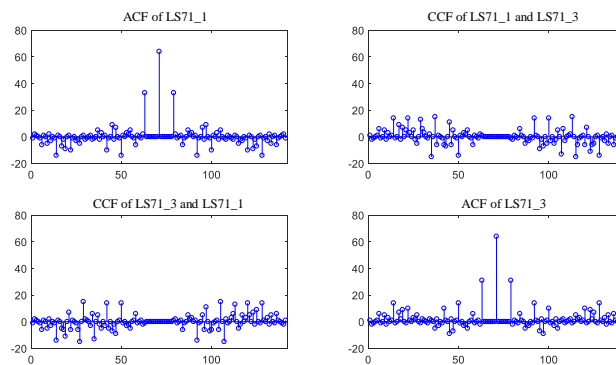

Fig. 5-8 Auto- and cross- correlation signal for two 71-bit LS sequences

Taking the four sets of sequences aforementioned into account, the sequence used in the electrical signal transmission for the improved track breakage system is determined by comparing the performance of the four sets of sequences in the same transmission scheme. Then, the transmission scheme needed to be determined.

5.1.2 Modulation Scheme

Similar to the process of DS-SS transmitter, both Kasami sequences and LS codes need a certain amount of bandwidth when transmitted through channels. The common solution is to make the sequence transmit within the available bandwidth through modulation. Indeed, it was already tested that a Binary Phase Shift Keying (BPSK) modulation is suitable in most applications [98]. In the case of BPSK modulation, the phase of the carrier varies with the state of the modulation sequence. When the sequence is "1", the carrier after modulation is in the same phase with the original carrier, and when the sequence is "0", the phase is inversely changed, this is to say that, the carrier phase under modulation sequence "1" and "0" differs each other by π.

Taking into account the previous considerations, a BPSK-like modulation is proposed here for the transmission of the Kasami and LS sequences. The idea is to keep the same carrier waveform in the transmissions, but to include the sequence information as an inversion of the carrier. In this way, when the bit of a certain sequence is equal to 1, a common carrier is transmitted, whereas whether the bit of the sequence is -1, an inverted carrier is transmitted (polarity change), and also, when the bit of the sequence is 0, a carrier with the amplitude of 0 is transmitted. Thus, this BPSK-like modulation approach uses the N_c periods of f_c=125Hz sine carrier with the amplitude of 3V as a modulation carrier. Note that, N_c =1, and $P = 40$ is the ratio between the sampling frequency f_s=5kHz and the carrier one fc, equivalent to the number of samples used to represent a carrier period. Fig. 5-9 depicts a period of modulation carrier. The modulation process to be conducted is expressed by (5-1), where $e[k]$ is the modulated signal to be transmitted; $c[k]$ is the binary sequence used to encode the emission (Kasami or LS); L is the length of this sequence; and $p[k]$ is a symbol with P samples per period (at a sampling frequency $f_s = 5$kHz).
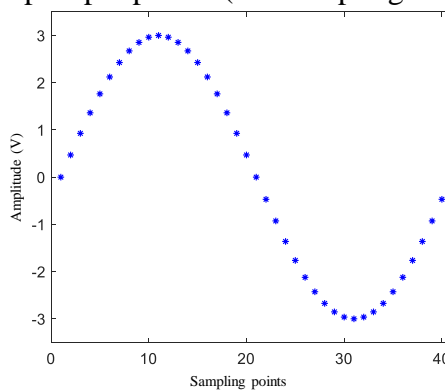
Fig. 5-9 One period of 125Hz sine carrier signal

$$e[k] = \sum_{i=0}^{N_c \cdot P \cdot L - 1} c\left[\frac{i}{N_c \cdot P}\right] \cdot p[k-i] \tag{5-1}$$

Fig. 5-10 to Fig. 5-13 respectively show the modulation results obtained by Kas15_1, Kas63_1, LS19_1 and LS71_1.
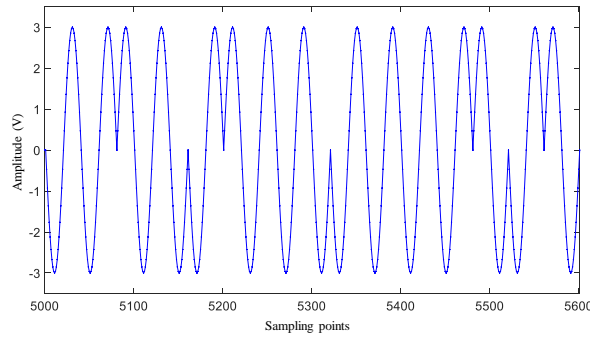
Fig. 5-10 The modulated signal by sequence Kas15_1
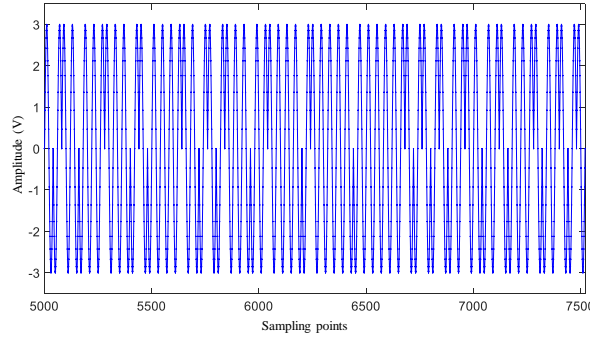
Fig. 5-11 The modulated signal by sequence Kas63_1
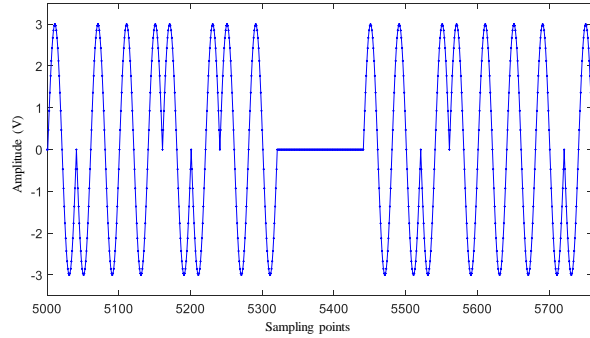
Fig. 5-12 The modulated signal by sequence LS19_1
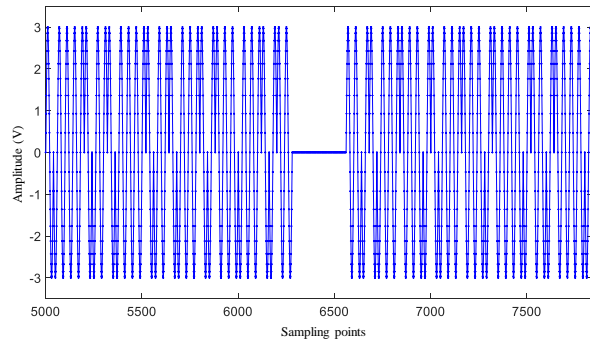
Fig. 5-13 The modulated signal by sequence LS71_1

Unlike the DS-SS processing at the receiver end, in order to take advantage of the better performance of sequences, the signal $r[k]$ acquired at the receiver is BPSK demodulated to obtain the signal $d[k]$, according to (5-2), where $d[k]$ is the output from the demodulation stage; $r[k]$ is the input signal coming from the acquisition stage; and $p[k]$ is the modulation symbol represented by P=40 samples.

$$d[k] = \sum_{i=0}^{N_c \cdot P - 1} r[i+k] \cdot p[i] \tag{5-2}$$

Afterwards, the demodulated output $d[k]$ should be correlated in order to search for possible emissions coming from the transmitters. This correlation process is described in (5-3), where $t[k]$ is the correlation output; $d[k]$ is the previous demodulation output; $c[k]$ is the transmitted code, Kasami or LS; and L is the length of the mentioned code.

$$t[k] = \sum_{i=0}^{L-1} d[i \cdot N_c \cdot P + k] \cdot c[i] \tag{5-3}$$

For the eight sequences (Kas15_1/Kas15_3, Kas63_1/Kas63_4, LS19_1/LS19_3 and LS71_1/LS71_3) mentioned above, in the transmitter end, the respective modulation signals are saved in .mat file in the simulation model. Taking advantage of the simulation models described in Fig. 4-9, the modulated signal transmissions in the 1km-long track section under ideal environment are simulated, and the corresponding ACF and CCF signals can be observed from Fig. 5-14 to Fig. 5-17.
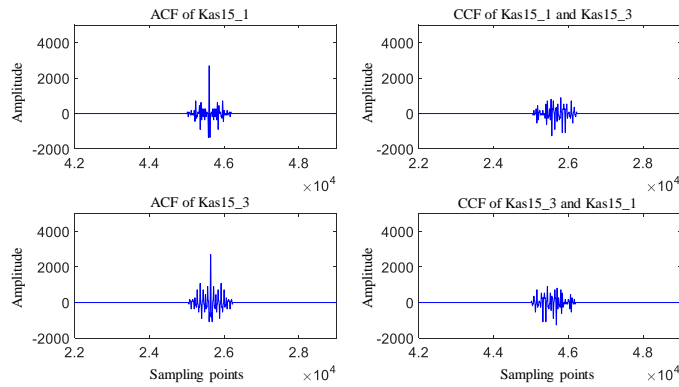
Fig. 5-14 Correlation signals acquired in the receiver end, modulated by sequences Kas15_1 and Kas15_3
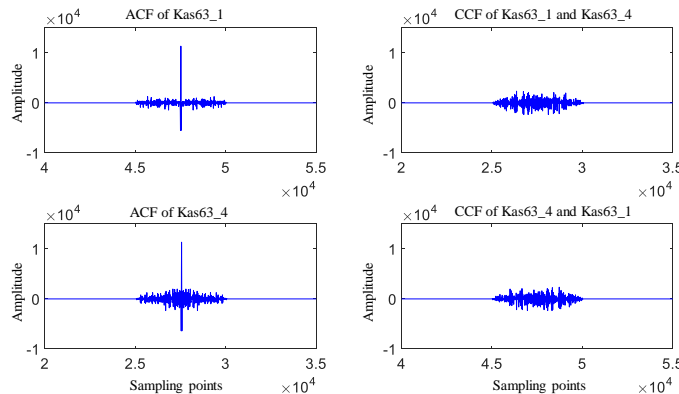
Fig. 5-15 Correlation signals acquired in the receiver end, modulated by sequences Kas63_1 and Kas63_4
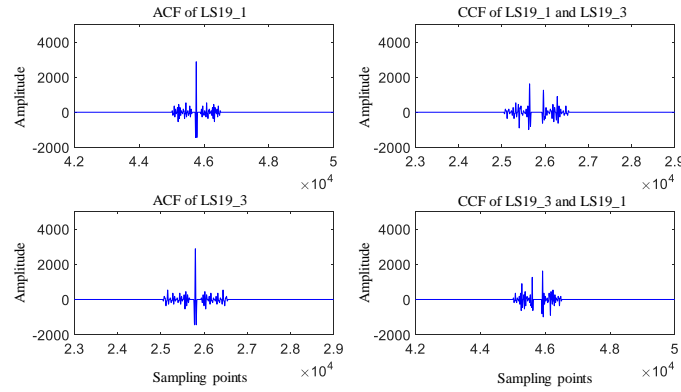
Fig. 5-16 Correlation signals acquired in the receiver end, modulated by sequences LS19_1 and LS19_3
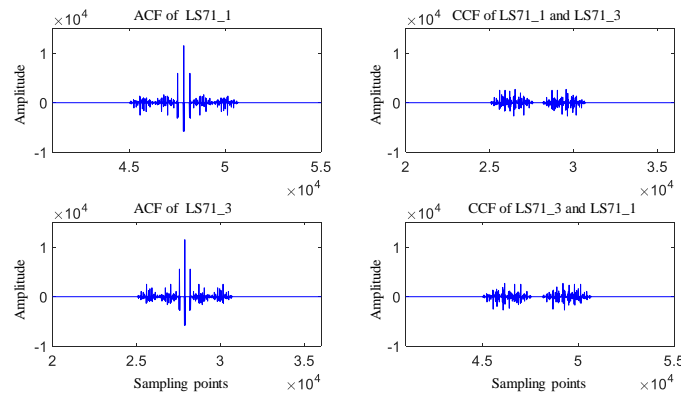
Fig. 5-17 Correlation signals acquired in the receiver end, modulated by sequences LS71_1 and LS71_3

As can be observed from Fig. 5-14 to Fig. 5-17, in section *i*, when the sine carriers are modulated with sequence A in the transmitter end: if the receiver in the same section get the correct transmission, by the process of demodulation and correlation, the ACF signals with high peaks values can be detected, the useful signal can be distinguished among interferences; on the other hand, if the receiver obtained the signal transmitted from other sections, the CCF signals with lower amplitude will be calculated. Taking the situation shown in Fig. 5-17 as an example. If the carriers are modulated by sequence LS71_1 in the transmitter end of section *i*, using the same sequence LS71_1 as the demodulation sequence, only when the receiver get the correct transmission signal from section *i*, the upper left part in Fig. 5-17 can be obtained; whereas, when the receiver get the signals come from other section, which its sequence used for modulation is LS71_3, the upper right part in Fig. 5-17 is got, and it represents the multipath interference. Using sequence LS71_3 as the modulation sequence in receiver end consistent with the situation described above, and this situation can be observed in the two lower parts of Fig. 5-17.

Combining the simulation results from Fig. 5-14 to Fig. 5-17 with the content aforementioned, the distribution structure of sequences in the railway line can be projected as in Fig. 5-18. The interference between neighboring lines is considered. For section *i*, only the receive get the transmission signals from its native section, the ACF signals with high peak value can be obtained.

When section i receives signals from adjacent sections i-1 or i+1, or from any other sections j, j-1 or j+1 of the parallel railway line, what the receiver can be obtained in section i are CCF signals which represent for interferences. Thus, only four sequences are good enough to recognize the transmitted signals on the track. It is worth noting that, the four sequences A, B, C and D shown in Fig. 5-18 is the different sequences from the same set. From above, the four sets of sequences Kas(4,4,15), Kas(6,8,63), LS(4,19,3) and LS(8,71,7) all meet the requirement of signal transmission in this work.

Line 1

Section i-1	Section i	Section i+1
Sequence B	Sequence A	Sequence B

Section j-1	Section j	Section j+1
Sequence D	Sequence C	Sequence D

Line 2

----- Modulated signal by sequence A   ----- Modulated signal by sequence B

----- Modulated signal by sequence C   ----- Modulated signal by sequence D
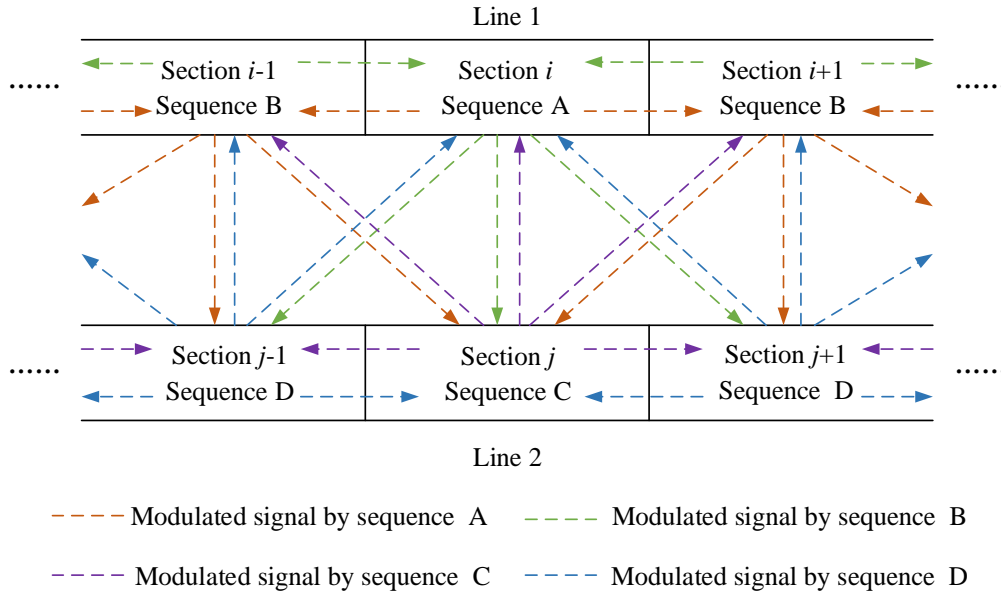
Fig. 5-18 The distribution structure of sequences in the railway line

5.1.3 Correlation Bound

As has been already commented, the selected codes are required to have a suitable aperiodic AC function to ensure proper transmission detection and high process gain, as well as low aperiodic CC values to reduce multiple access interference among simultaneous emitters.

Some previous works have already analyzed the aperiodic correlation properties of codes [99-100], whereas the selection and optimization of sequence families with suitable aperiodic correlation properties still receive a considerable interest [101-102]. The search for sequences with suitable aperiodic correlation properties has been studied mainly on empirical bases. The complexity of this search often increases as the length of sequences does, thus constraining the search possibilities. A solution could be the use of suboptimal procedures that limit the search to fewer possibilities, or to stop the search when a quality parameter used to evaluate the sequences reaches a certain threshold.

One common approach in literature to quantify the performance provided by sequences is based on the AC bound θ_{AC} and on the CC bound θ_{CC} [103]. The global bound $\theta = \max\{\theta_{AC}, \theta_{CC}\}$ is a commonly used figure of merit, considered as the maximum between the AC bound θ_{AC} and

the CC bound θ_{CC}. It provides a ratio between the maximum sidelobe obtained in both correlation functions and the AC main peak. At the same time, this work defines a novel bound θ_R, as the ratio between the maximum value obtained in the experimentally received AC functions and the ideal AC main lobe obtained under ideal operation conditions (track section is complete, environment is dry, and no train occupies the corresponding track section). Due to their relevance in this work, the bounds θ_{AC} and θ_R are represented in (5-4) and (5-5), respectively. Where $C_{ap,ap}$ denotes the AC function for certain test conditions, $C_{np,np}[0]$ is the AC main lobe under ideal conditions; and M is the number of sequences in the set, that is, the number of uncorrelated or pseudo-uncorrelated sequences available.

$$\theta_{AC} = \max\left\{ \frac{\left\|C_{a_p,a_p}[\tau]\right\|}{C_{a_p,a_p}[0]}; \forall p \in [0,\cdots,M-1]; \forall \tau \neq 0 \right\} \tag{5-4}$$

$$\theta_R = \max\left\{ \frac{\left\|C_{a_p,a_p}[\mu]\right\|}{C_{n_p,n_p}[0]}; \forall p \in [0,\cdots,M-1]; \forall \mu \right\} \tag{5-5}$$

Next, the performance of eight sequences is evaluated by calculating the bounds θ_{AC} and θ_R based on the simulation model. The process of evaluation is also the process to verify the feasibility of the electrical signal transmission scheme proposed in this work, as well as the reliability of signal transmission in the presence of coupling interference between adjacent railway lines.

Take the sequence $Kas(4,4,15)$ as an example, in the model proposed in Fig. 4-14, the signal which is modulated by sequence Kas15_1 is used as the output signal of the transmitter in Line 1, while the signal modulated by sequence Kas15_3 used as the transmitted signal in Line 2. These two signals are simultaneously transmitted to the receiver end through their respective 1km long track sections. Because of the electromagnetic coupling between two railway lines, receiver R1 and R2 can not only receive the modulated signal sent by the transmitter in their own section, but also receive the interference signal comes from the neighboring line simultaneously. Therefore, the values of each ACF and CCF can be calculated at the receiver end. In order to further determine the reliability of signal transmission with the modulation scheme, Gaussian white noises with variable SNR are added to railway Line 1 and Line 2 respectively on the basis of coupling interference. Under different interference conditions, the peak value of ACF signal obtained by which receiver is more easily identified, then the sequence applied in the transmission of this line has better performance, that is to say, the sequence with better performance has lower auto-correlation bound value θ_{AC}.

Similar with the example of sequence *Kas*(4,4,15), the sequences selected from *Kas*(6,8,63), *LS*(4,19,3) and *LS*(8,71,7) are also applied to the model in Fig. 4-14. The lower the bounds θ_{AC} are (always below one), the better the performance is for the corresponding sequences. This condition implies that the correlation maximum can be detected more easily among sidelobes, as well as the transmitted signal can be distinguished from noise. In some previous works, it has been experimentally stated that the limit for these 2 bounds θ_{AC} and θ_{CC} should be 0.5 [104].

From this point of view, take the average value of ten times calculation for each noise condition, as shown in Fig. 5-19 to Fig. 5-22, except for the 71-bit LS code, all the other types of sequences have good performance. Although the 63-bit Kasami sequences have better performance than the other ones in general, the 15-bit Kasami and 19-bit LS codes still show a stable performance in bad noise conditions.
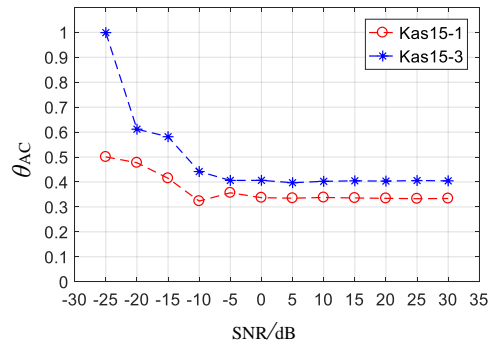

Fig. 5-19 Auto-correlation bound θ_{AC} for different Gaussian noise conditions (Kas15_1 and Kas15_3)

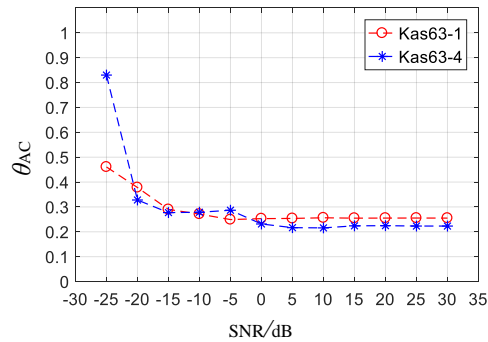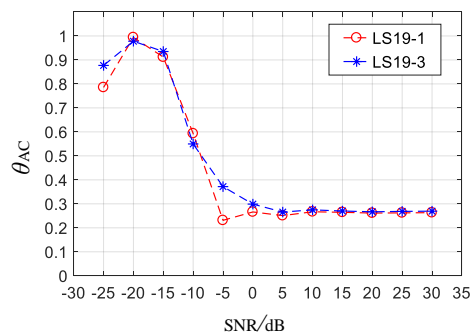Fig. 5-20 Auto-correlation bound θ_{AC} for different Gaussian noise conditions (Kas63_1 and Kas63_4)

Fig. 5-21 Auto-correlation bound θ_{AC} for different Gaussian noise conditions (LS19_1 and LS19_3)
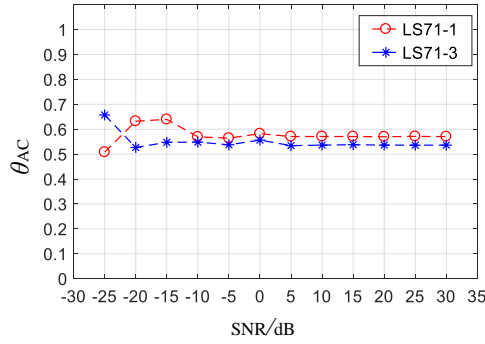
Fig. 5-22 Auto-correlation bound θ_{AC} for different Gaussian noise conditions (LS71_1 and LS71_3)

Another comparison about the bound θ_{AC} and θ_R for Kasami and LS codes has been performed for different track conditions in Tab. 5-5. Assuming that track no. 1 is always under the normal operation mode, without train occupation, whereas track no. 2 is under different occupancy conditions, each value in Tab. 5-5 comes from the average of five times calculation.

Tab. 5-5 The bound comparison for four types of sequences under different track conditions

No.	Test Condition	15-bit Kasami		63-bit Kasami		19-bit LS		71-bit LS	
		θ_{AC}	θ_R	θ_{AC}	θ_R	θ_{AC}	θ_R	θ_{AC}	θ_R
1	Track 1：Normal	0.3337	⋯	0.2548	⋯	0.2629	⋯	0.5170	⋯
	Track 2：Normal	0.3989	⋯	0.2237	⋯	0.2631	⋯	0.4911	⋯
2	Track 1：Normal	0.3328	⋯	0.2545	⋯	0.2629	⋯	0.5171	⋯
	Track 2：Off	0.8496	0.0100	0.9186	0.0039	0.7689	0.0118	0.9985	0.0054
3	Track 1：Normal	0.3327	⋯	0.2545	⋯	0.2629	⋯	0.5171	⋯
	Track 2：Shunt in the transmitter end	0.4055	0.1507	0.2209	0.1511	0.2496	0.1502	0.4906	0.1508
4	Track 1：Normal	0.3329	⋯	0.2545	⋯	0.2629	⋯	0.5171	⋯
	Track 2：Shunt in the middle	0.4034	0.1242	0.2193	0.1240	0.2590	0.1240	0.4911	0.1240
5	Track 1：Normal	0.3328	⋯	0.2545	⋯	0.2629	⋯	0.5170	⋯
	Track 2：Shunt in the receiver end	0.4017	0.0264	0.2177	0.0265	0.2576	0.0265	0.4920	0.0264

In test no. 1, since there is no train on both tracks, the signals encoded with Kasami or LS sequences should have similar AC functions, with reduced sidelobes, to minimize crosstalk interference, thus making easy to detect the arrival of transmissions. In this situation, the AC bound θ_{AC} becomes relevant about the behavior of the system. The lower bound θ_{AC} is, the easier the determination of the instant of arrival for the transmitted signals is. On the other hand, since this situation is considered as the ideal or normal one, the AC main peak obtained here is taken

as the value $C_{np,np}[0]$ in (5-4) and (5-5) for further analysis. In test no. 2, the emitter for track no. 2 is off, which means there is no signal transmitted to the receiver. In this case, the bound θ_{AC} is not relevant since there is no transmitted sequence for receiver no. 2, whereas the bound θ_R provides information about the coupling influence from track no. 1.

From test no. 3 to 5, track no. 2 is occupied by trains in different locations (near the emitter, in the middle of track section, and near the receiver), thus meaning that significant differences in the relative power level of the received signals can appear due to coupling effects along the track section. In these three last cases, the signals transmitted through the track with no train have a relatively high influence on the signals transmitted through the other track, so the AC bounds θ_{AC} are similar to those in the normal mode (test no. 1), while the bounds θ_R are very low and decrease when the trains are approaching to the receiver end. These figures imply that train occupancy can be detected in further processing, not being mistaken by coupling interference coming from the other transmitter. In general, both the AC bound θ_{AC} and the bound θ_R become significant. The bound θ_{AC} is a key point to distinguish the corresponding transmission at the receiver, whereas the bound θ_R allows the analysis of the influence of one emitter on the other one through their CC function. Both bounds also vary under different track conditions and train occupancy. From these figures, it can be concluded that 15-bit and 63-bit Kasami sequences present a slightly better performance than 19-bit and 71-bit LS codes, while 15-bit Kasami sequence keeping the computational and implementation complexity low due to its reduced length.

Finally, some simulation results with changing environmental conditions and track imperfections have been considered. Taking the four sequences Kas15_1, Kas63_1, LS19_3 and LS71_3 which have relevant better performance in each set, as well as applying them to modulated the carrier in the transmitter end of both neighboring railway lines in Fig. 4-14. Then, according to the Fig. 4-15 and 4-16, the conductivity and permittivity of soil around the track change for different water contents. Corresponding to the frequency of 125Hz, the values under different water contents are used in the model mentioned in Fig. 4-14. These may lead to the variance of capacitance and conductance, both in the rail itself and in the electromagnetic coupling between two near parallel tracks. Taking this into account, the AC bounds for the four types of codes considered here are shown in Fig. 5-23 under different water contents. As can be observed, the AC bound for 63-bit Kasami sequences is much lower for the three water contents; also, although the AC bound for 15-bit Kasami sequences is higher than 63-bit one, it always keeps below 0.5.
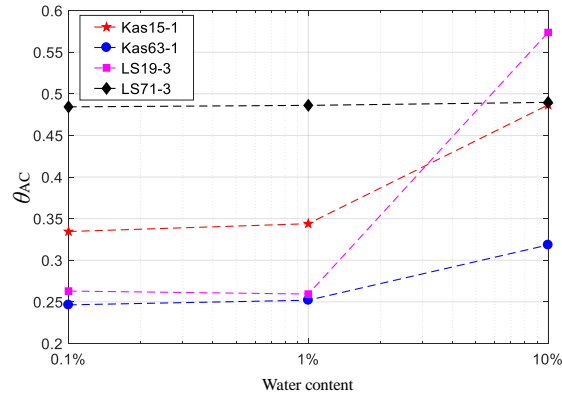
Fig. 5-23 Auto-correlation bound θ_{AC} under different water contents in soil

To sum up, the modulated signal by 63-bit Kasami sequence has excellent performance in anti-noise performance under different SNR conditions, different track statuses, as well as the variable water content of ground. Therefore, the modulation signal by 63-bit Kasami sequence is selected as the electrical transmitted signal in the improved track breakage detection system. The modulated signals used in the following of this work are all generated after the modulation of 125Hz sinusoidal carrier with sequence Kas63_1.

5.2　Novel Adaptive Peak Detection Algorithm and Track Status Identification Method

The estimation of the track section state mainly depends on the processing of the correlation signals $t[k]$ obtained in the receiver. Some previous works have usually determined the state of a track section by comparing the received signal amplitude or the correlation output with a fixed threshold. Nevertheless, as mentioned previously, this approach presents some drawbacks, as noise and interference can become higher than the fixed threshold, then validating them as correct transmission.

Taking into account these issues, an adaptive peak detection algorithm is proposed here, where no fixed threshold or any empirical factor is considered. The dataflow of the proposal can be observed in Fig. 5-24. Subsequently, every module will be explained in detail.

Received Signal: $r[k]$
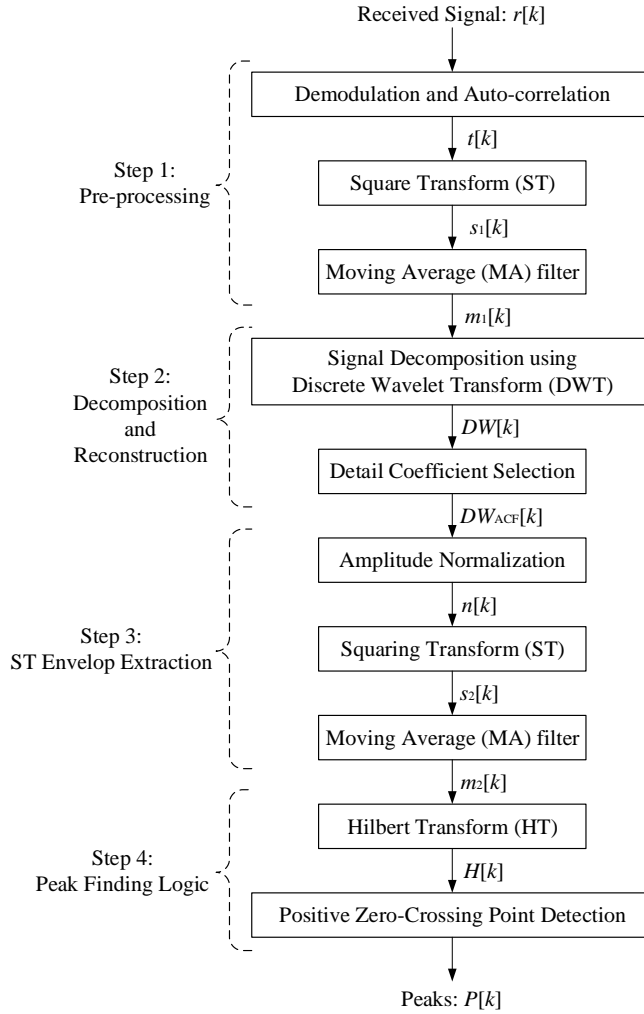
Fig. 5-24 Flow-process diagram of the proposed peak detection algorithm

5.2.1 Signal Pre-processing

This stage has been partly presented before, at least for the first module dedicated to the demodulation and correlation processes to obtain the correlated output $t[k]$. Afterwards, a squaring operation is applied (5-6), in order to discard the uncertainties from bipolar signals and to enhance the main lobes of the ACF signals [105-106].

$$s[k] = t[k] \cdot t[k] \qquad (5\text{-}6)$$

Then, the resulting squared signal $s[k]$ is smoothened by a moving average (MA) filter. This is a straight-forward approach to reduce random noise while keeping a sharp step response. Every sample from the input signal $s[k]$ is averaged by a group of nearby samples according to (5-7) [107]. Where $m[k]$ is the output averaged signal; and K is the number of samples involved in the average. Alternative to (5-7), a certain number of samples from the input signal $s[k]$ can be also chosen symmetrically around the output sample $m[k]$. Empirically, the length of the MA filter has been fixed equal to the width of the ACF main lobe [108]. If this length is shorter, the filter

provides numerous envelopes for a single ACF peak, thus leading to additional zero crossing points in next stages after the HT. Otherwise, if the length is too long, it involves useless information, thus also implying false detections. It is worth noting that, in this case, the length of the ACF main lobes is around 8ms. Thus, if the sampling frequency is $f_s = 5\text{kHz}$, the window size is $K = 40$ samples

$$m[k] = \frac{1}{K} \sum_{k=0}^{K-1} s[i+k] \tag{5-7}$$

For clarity's sake, Fig. 5-25 indicates an example of the received signal $r[k]$ from a simulation that will be used to illustrate how the proposed algorithm works. In this way, Fig. 5-26 plots the intermediate and resulting signals for the pre-processing stage, including the correlation signal $t[k]$, the squared signal $s_1[k]$ and the averaged signal $m_1[k]$, respectively.
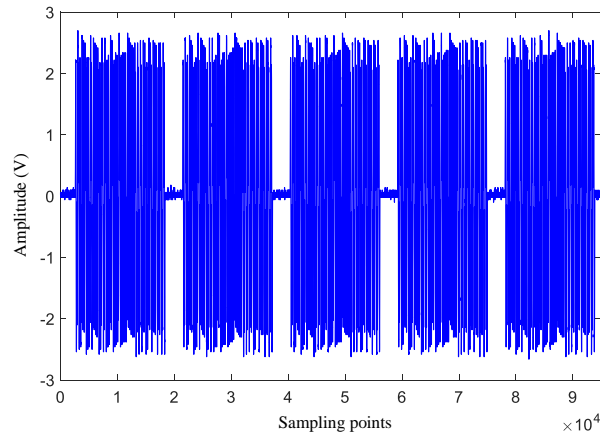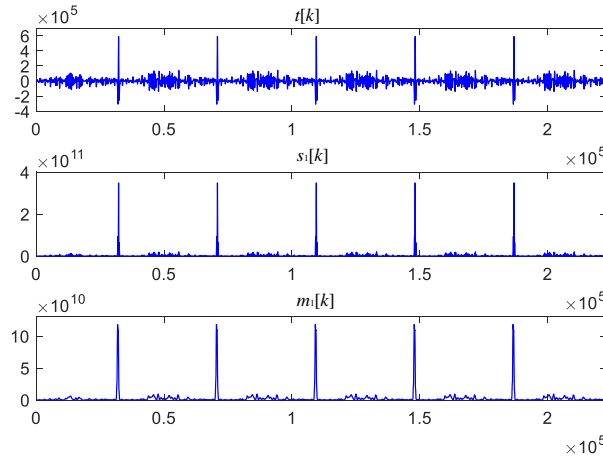

Fig. 5-25 Example of an acquired signal $r[k]$

Fig. 5-26 Resulting signals at the different modules in step 1: the correlation signal $t[k]$, the squared signal $s_1[k]$ and the average signal $m_1[k]$

5.2.2 Signal Decomposition and Reconstruction

In this stage, the smoothed signal $m_1[k]$ resulting from the previous step is firstly decomposed by using the DWT. Thus, the corresponding coefficients associated with the ACF main lobe frequency band are extracted. In order to select the suitable wavelet function, it is worth noting that, if this wavelet function and the input signal have certain degree of similarity, the transformation energy will be concentrated, which can effectively reduce the computation [109-110]. The Daubechies wavelet has been found to provide more accurate information with regard to the input signal $m_1[k]$ than others, since this is similar to the second-order Daubechies wavelet (db2), based on the principle of self-similarity.

The ACF signals are sampled at f_s = 5kHz, so their frequency components are from 0Hz to 2.5kHz. In the case of the signal $m_1[k]$ to be processed, most of the energy is focused on the range from 90Hz to 160Hz, due to the modulation carrier f_c = 125Hz. Fig. 5-27 indicates how the frequency range is decomposed at every level, as well as the coefficients involved in each frequency band. For the band of interest mentioned before, the coefficients D5 and D6 can offer an appropriate reconstruction of the initial signal $m_1[k]$. Following the example case, Fig. 5-28 depicts the output reconstructed signal $DW_{ACF}[k]$ based on both of the coefficients D5 and D6.
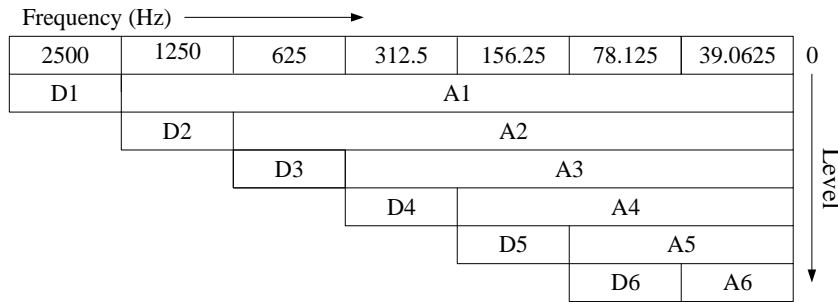
Fig. 5-27 Brief scheme of the performed DWT decomposition
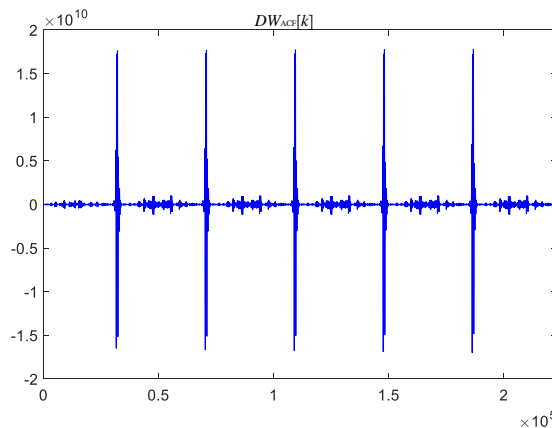
Fig. 5-28 Resulting signal $DW_{ACF}[k]$ after step 2

5.2.3 ST Envelop Extraction

Through this stage, the reconstructed ACF signal $DW_{ACF}[k]$ is normalized in terms of amplitude before another squaring and MA filtering. This normalization makes signals maintain

in the range from -1 to 1, so the following processing will be conducted under the same amplitude scale.

$$n[k] = norm(DW_{ACF}[k]) = \frac{DW_{ACF}[k]}{\max(|DW_{ACF}[k]|)} \tag{5-8}$$

Where $n[k]$ is the resulting normalized signal. Then, a squaring transform and a MA filter, similar to those described in step 2 are applied to signal $n[k]$ in order to smoothen the envelop extraction. Fig. 5-29 is the example for signal $n[k]$, where the maximum amplitude of the final signal $m_2[k]$ corresponds to the correct ACF peak.
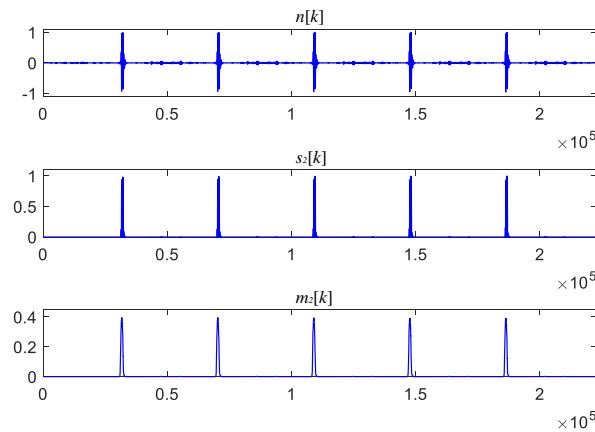
Fig. 5-29 Signals involved in step 3: normalized signal $t[k]$, squared signal $s_2[k]$ and average signal $m_2[k]$

5.2.4 Peak Finding Logic

The last stage consists of a HT, in order to avoid the usage of any threshold in the ACF peak determination. Fig. 5-30 graphically describes the way the ACF peaks (main lobes) are finally determined. It can be observed that the maximum value of the input signal $m_2[k]$ matches the positive zero-crossing point in $H[k]$ after the HT. Fig. 5-31 presents the simulation results for the example case: the input signal $m2[k]$ is plotted with a dashed line, whereas the solid line represents the HT result $H[k]$, and the dots determine the zero-crossing points. The correlation main lobes from the ACF function are identified correctly。
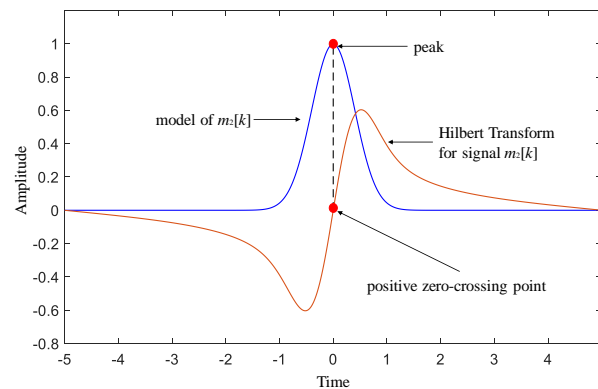
Fig. 5-30 Peak detection based on the positive zero-crossing of the Hilbert transform signal
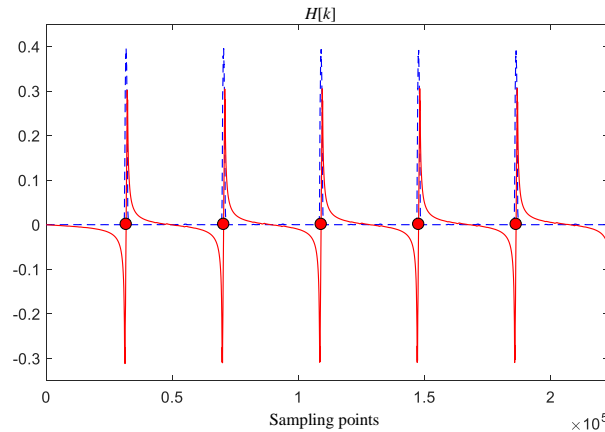
Fig. 5-31 Peak detection based on the positive zero-crossing of the HT signal

It should be noted that, in the case of electrical signals transmission, the receiver uploads the detected peak value to the remote monitoring center, and the server distinguishes them by detecting the peak values of six continuous signals. The speed of fast train is 120km/h in usual, and the high-speed train is 300km/h. That is to say, considering the length of the train itself, it takes about 40s for the fast train to pass through a 1km track section, while high-speed train takes less time. For the six continuous received signals, the peak value of correlation signals obtained at the receiver end is relatively small, then the track breakage is considered to be happened; if there is a variable trend in the peak value of correlation signals, it is considered to be the case of train occupancy.

However, for the area covered by the track breakage detection monitoring network, as the number of broken sections is small, the track status determination is not included in the LSTM network aforementioned. Instead, the peak value of correlation functions in the track circuit applied track section is detected on the receiver end, and the determination is sent to the remote monitoring center through the wireless communication module. When the correlation peak remains above 50% of the ideal value, and the difference between each correlation peak is small, then the detected track section is considered free; if the peak values of six continuous correlation signals are all less than 15% of the ones in the ideal situation, the track is meant to be broken; once there is a fluctuation from upper 50% to under 15% for the peak values of six continuous correlation signal, the track section is occupied by a train.

5.3   Experimental Results

In addition to the simulation results for different steps shown in above, the proposed track circuit based on the signal encoding with a 63-bit Kasami sequence has been applied to a 1km-long track section. The involved experimental equipment mainly includes a transmitter, a receiver,

some cables, and the transducers. Fig. 5-32 and Fig. 5-33 show the transmitter and receiver respectively. Fig. 5-34 shows the installation at the transmitter end. Note that the one at the receiver end is similar.
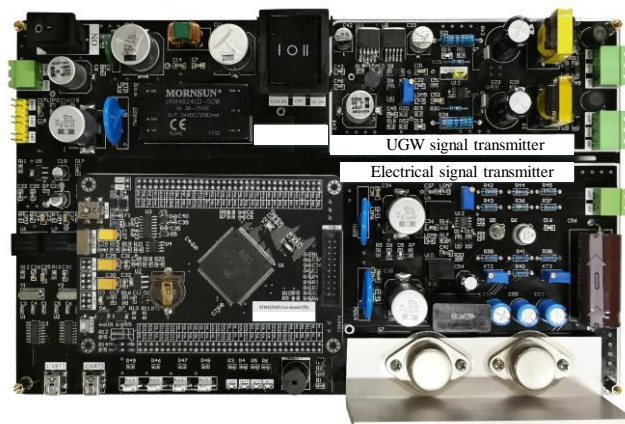

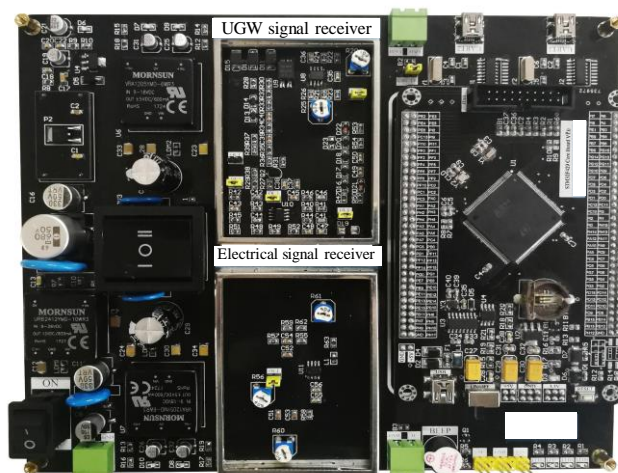Fig. 5-32 The transmitter board of the improved track broken detection system

Fig. 5-33 The receiver board of the improved track broken detection system
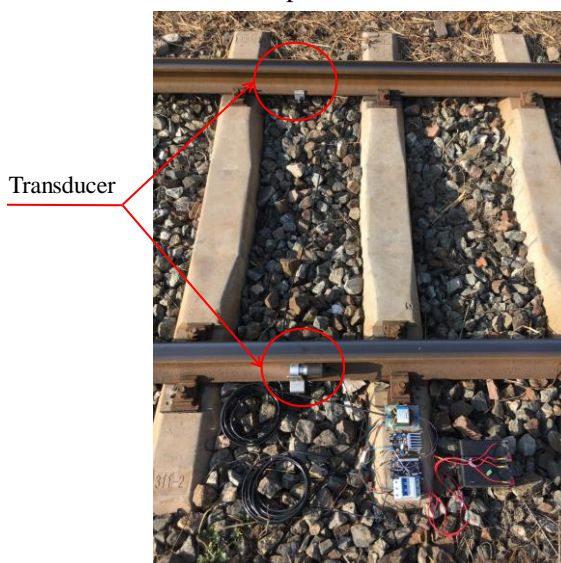
Fig. 5-34 Installation of equipment at the transmitter end

The hardware design for both the transmitter and the receiver is based on the microprocessor STM32F429. At the transmitter end, the 63-bit Kasami sequence is stored in the microprocessor to modulate the 125Hz sine carrier, and then the modulated signal goes through an integrated DAC. The converted signal is amplified by two stages based on OPA445 and OPA541, and finally, the adjusted signal with the output amplitude of 2.5V after the transformer is sent to the transducer. Thus, through the transducer, the electrical signal is connected with rail. By the 1km long track distance transmission, at the receiver, the signals first go through a transformer with an opposite ratio corresponding to the transformer in the transmitter end, then, the signals propagate through a 4th-order Butterworth band-pass filter to discard the interference. Before the ADC with a sampling frequency of 5kHz, a level-adjusting circuit mainly based on TL074 is also included. The acquired signals are then processed by the algorithm described before, running in the corresponding processor. After being modulated by 63-bit Kasami sequences, the signal is sent every 10s, and the receiver end also collects and processes the signal at the same time interval.

In order to demonstrate the feasibility of the encoded transmission scheme, as well as the accuracy and reliability of the peak detection algorithm in the proposed improved track breakage detection system, some experimental tests have been conducted under different track and noise conditions. For that purpose, the signal $e[k]$ to be transmitted, encoded by a 63-bit Kasami sequence, is sent every 10s.

5.3.1 Signal Transmission and Detection under Different Track Status

In the first scenario, no additional noise is included in the system and the track section does not present any breakage or joint maintenance, or any train occupation. Fig. 5-35 indicates the three transmissions acquired under these free track states, whereas Fig. 5-36 depicts the corresponding correlation signal $t[k]$ and the final resulting signal $H[k]$. For clarity's sake, the signal $H[k]$ is zoomed out to clearly observe how the correlation peaks and zero-crossing points in $H[k]$ match each other.

Fig. 5-35 Received signal $r[k]$ under free condition

Fig. 5-36 Correlation signal $t[k]$ (up) and final resulting signal $H[k]$ (middle), as well as a zoom of the middle one (down), under free conditions

Whether there is a breakage in any place in the 1km long track section, the amplitude of the received signal $r[k]$ rapidly decreases, but it does not disappear and interference become increasingly significant. The breakage in the experimental track section can be observed in Fig. 5-37. For this scenario, three periodic transmissions are displayed in Fig. 5-38, where interference has a higher amplitude than the received signal $r[k]$. Although the received transmissions have low amplitude and include noise, the correlation signal $t[k]$ still provides clear peaks due to the satisfactory robustness against noise from the encoding scheme. It is worth noting that the amplitude of the main lobes from the correlation signal $t[k]$ is smaller than that obtained under ordinary conditions. Anyway, the different correlation peaks can be obtained in Fig. 5-39.
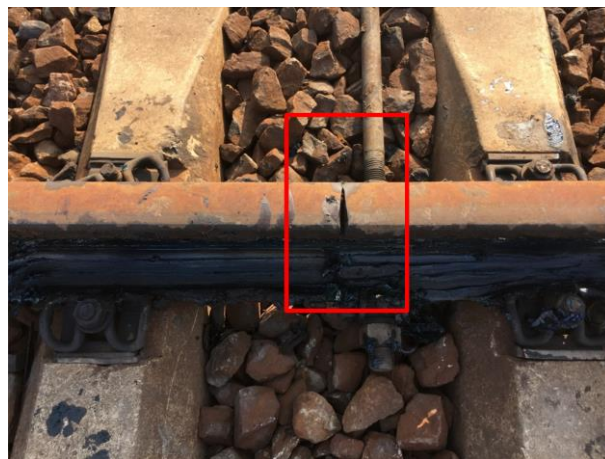
Fig. 5-37 View of a breakage in the 1km-long track section
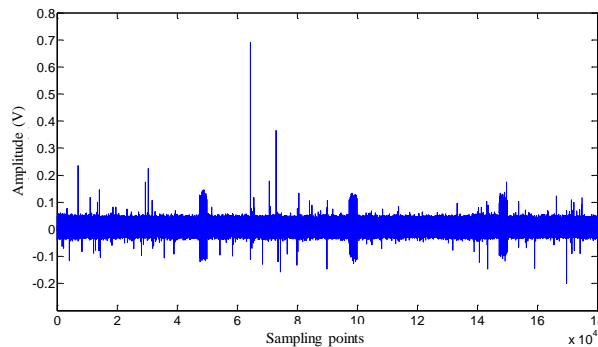
Fig. 5-38 Received signal *r*[*k*] when there is a breakage in track

Fig. 5-39 Correlation signal *t*[*k*] (up) and final resulting signal *H*[*k*] (middle), as well as a zoom of the left one (down), with a track breakage

When the breakage occurs, the joint bar is used to fix the gap. The received signal *r*[*k*] after passing through the joint maintenance can be observed in Fig. 5-40. When compared to the normal condition without any joint maintenance, the amplitude of the received signal *r*[*k*] is lower again, although the correlation peaks can still be detected as displayed in Fig. 5-41.

Fig. 5-40 Received signal *r*[*k*] after including a joint maintenance
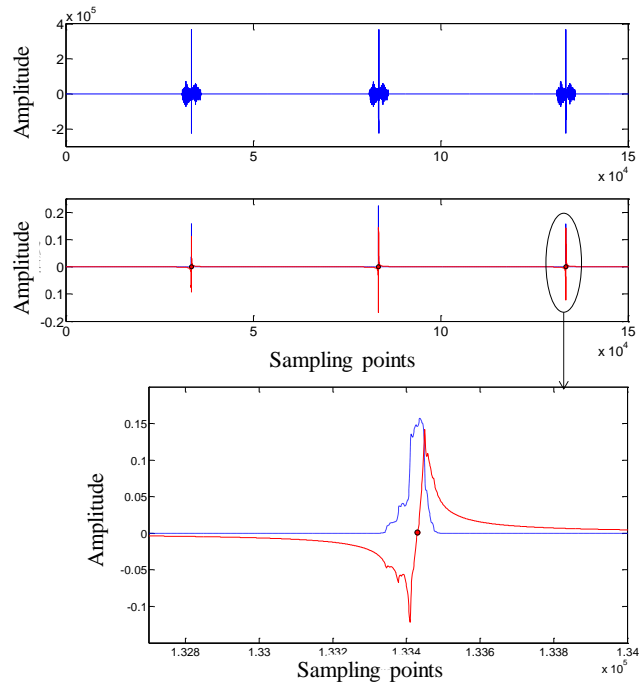
Fig. 5-41 Correlation signal *t*[*k*] (up) and final resulting signal *H*[*k*] (middle), as well as a zoom of the right one (down), for a section with a joint maintenance

The last aspect for analysis is the influence when the detection track section is occupied by a train. In this experiment, a short-circuiter which used to simulate the train occupied status is installed in the middle of the 1km track section, the installation of the short-circuiter can be observed in Fig. 5-42.
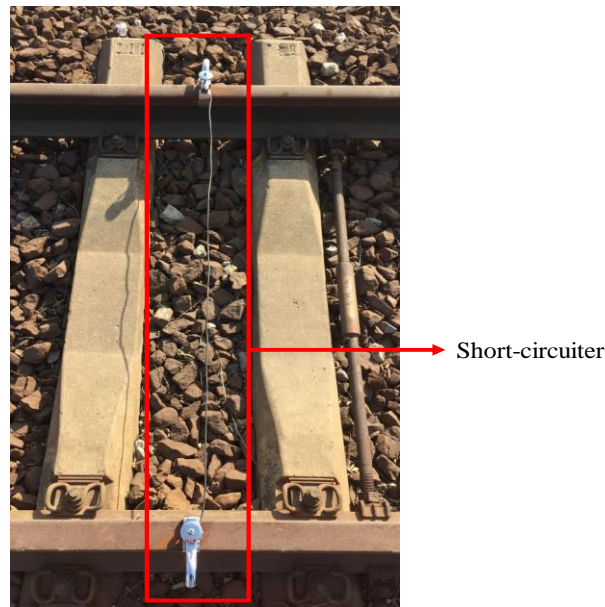
Fig. 5-42 Using a short-circuiter to simulate track occupation

Under the experimental condition described in Fig. 5-42, the obtained signal in the receiver end can be observed in Fig. 5-43, the amplitudes of these three periods of signals are similar with the ones shown in Fig. 5-38. Fig. 5-44 depicts the corresponding correlation signal *t*[*k*] and the

final resulting signal $H[k]$. For clarity's sake, the signal $H[k]$ is also zoomed out to clearly observe how the correlation peaks and zero-crossing points in $H[k]$ match each other.
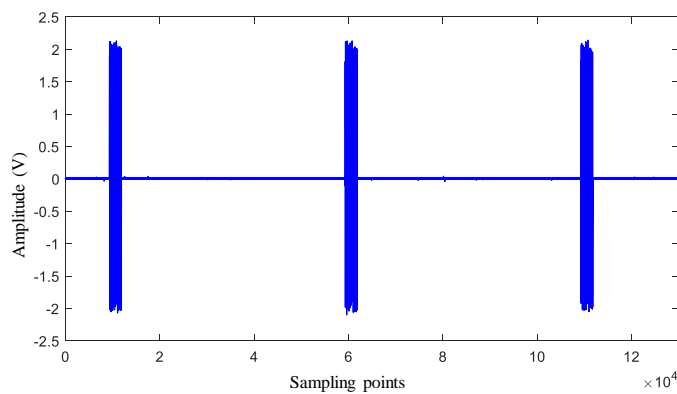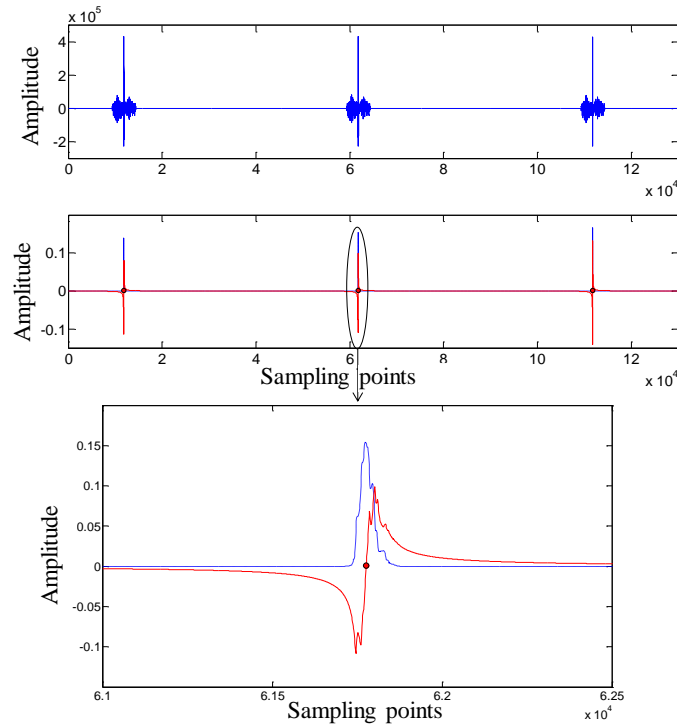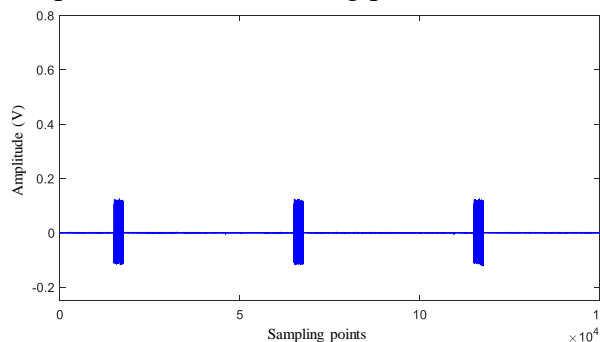

Fig. 5-43 Received signal $r[k]$ when using a short-circuiter

Fig. 5-44 Correlation signal $t[k]$ (up) and final resulting signal $H[k]$ (middle), as well as a zoom of the left one (down), for a section with a shunt equipment

5.3.2 Signal Transmission and Detection under Different Noise Condition

After analyzing the signal transmission, identification and detection in different track conditions, the influence that noise and interference have on the performance of the proposed detection system is analyzed. For that purpose, in the first example, interference has been added to the received signal $r[k]$, according to the spectrum often generated by trains circulating in railways [111]. It consists of a 50Hz fundamental sine and its main harmonics. Fig. 5-45 shows the received signal $r[k]$ in these conditions, with a SNR of 4.1dB, whereas Fig. 5-46 plots the detection of the resulting peaks, which are still correctly validated, though the correlation side lobes have a relatively high amplitude.
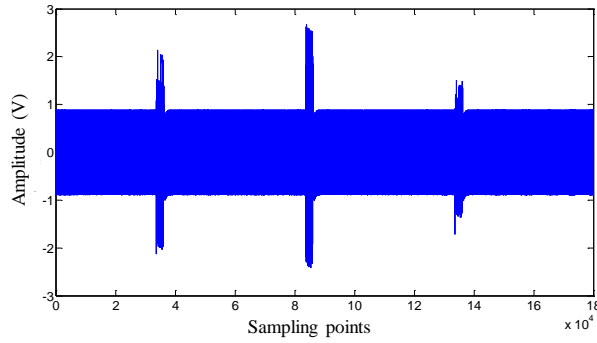
Fig. 5-45 Received signal *r*[*k*] after inserting interference caused by trains
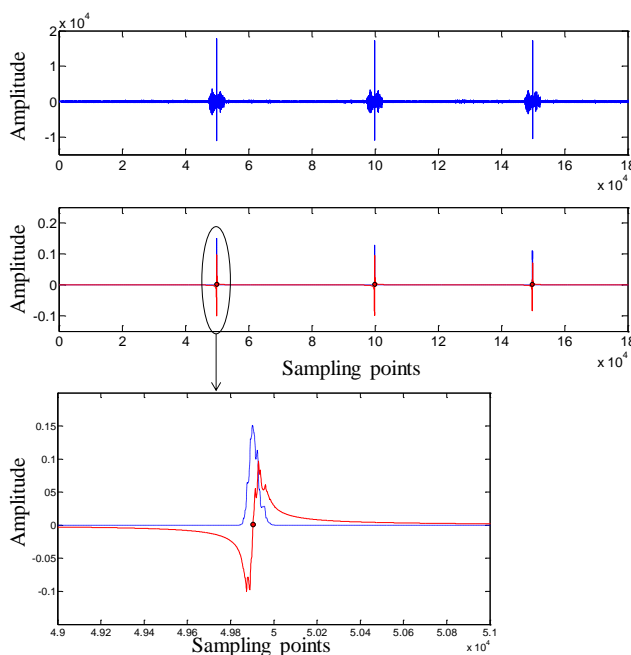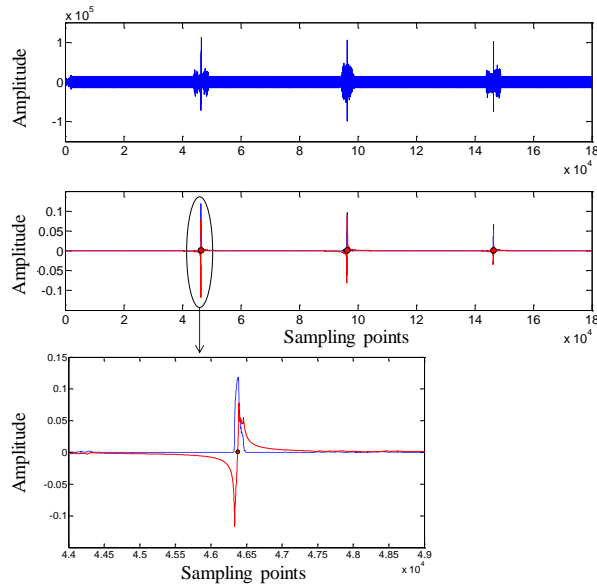

Fig. 5-46 Correlation signal *t*[*k*] (up) and final resulting signal *H*[*k*] (middle), as well as a zoom of the left one (down), when interference caused by train is added

In the second example, an oscillation noise, which combines the 225Hz and 350Hz frequency components, is added to the basic signal. The signal *r*[*k*] obtained at the receiver end with SNR=9.7dB can be observed in Fig. 5-47, and its corresponding ACF and HT results, *t*[*k*] and *H*[*k*] respectively, are depicted in Fig. 5-48. In the zoomed graph, it is still possible to observe the correspondence between the ACF peaks and the positive zero-crossing points.
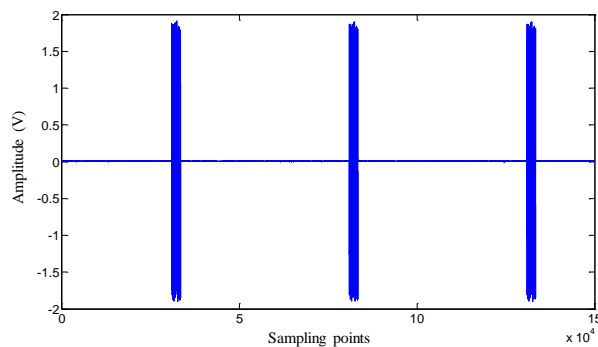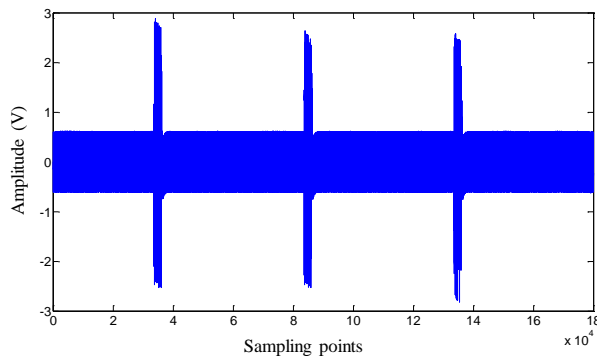

Fig. 5-47 Received signal *r*[*k*] including an oscillation noise
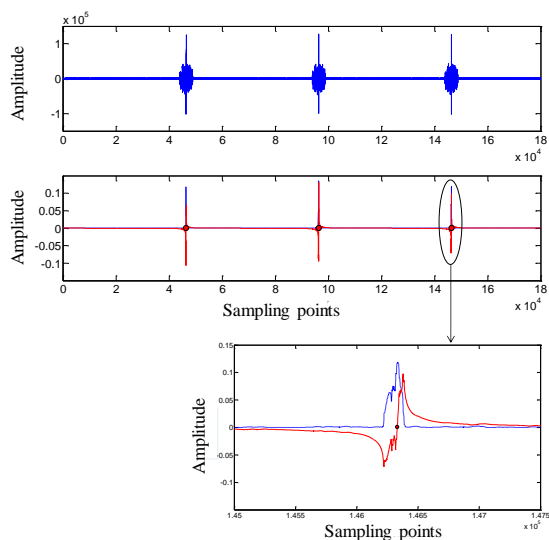
Fig. 5-48 Correlation signal $t[k]$ (up) and final resulting signal $H[k]$ (middle), as well as a zoom of the first one (down), when oscillation noise is inserted

An equi-distribution noise with SNR=14.8dB has also been brought into the transmission channel, where the corresponding received signal $r[k]$ is presented in Fig. 5-49. After all the processing steps, the correct correlation peaks are detected in Fig. 5-50.
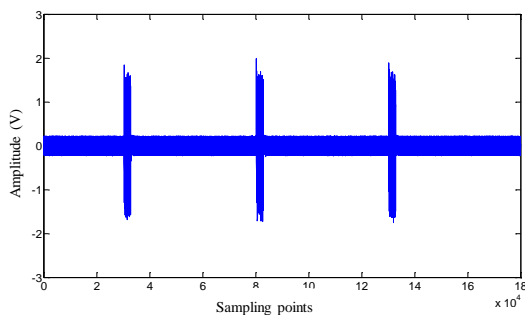
Fig. 5-49 Received signal $r[k]$ with an equi-distribution noise
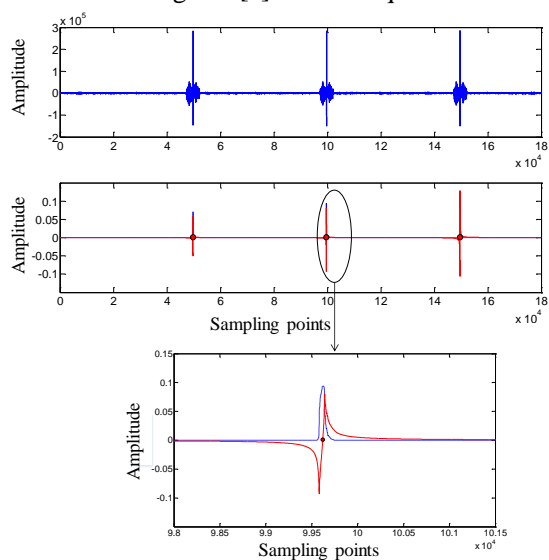
Fig. 5-50 Correlation signal $t[k]$ (up) and final resulting signal $H[k]$ (middle), as well as a zoom of the middle one (down), when an equi-distribution noise is inserted

Finally, a Gaussian noise with SNR=-20dB has been inserted in the transmission channel. In this situation, the received signal $r[k]$ is shown in Fig. 5-51. Though it is not possible to distinguish the received transmissions before processing, the correct ACF peaks can still be observed in Fig. 5-52, and the peaks are detected correctly from the positive zero-crossing points.

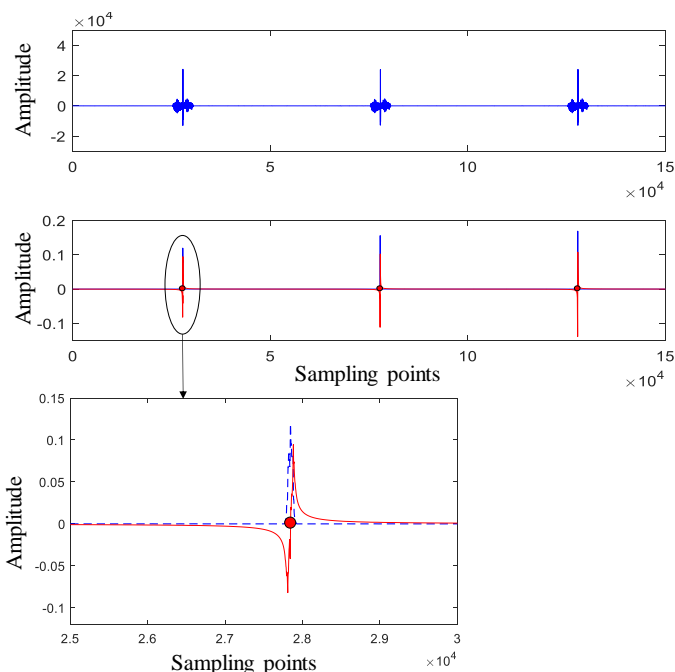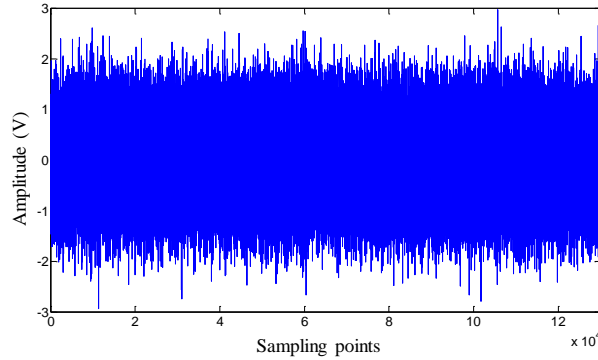
Fig. 5-51 Received signal $r[k]$ with a Gaussian noise (SNR=-20dB)
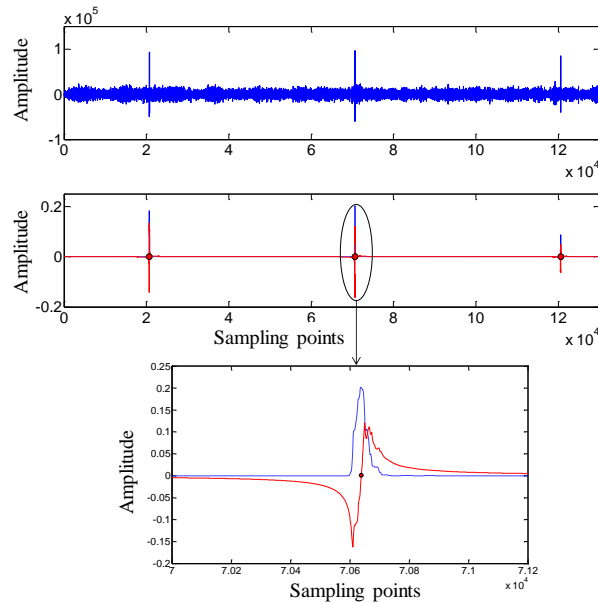
Fig. 5-52 Correlation signal $t[k]$ (up) and final resulting signal $H[k]$ (middle), as well as a zoom of the middle one (down), when an SNR= -20dB Gaussian noise is inserted

To conclude, considering all the experimental conditions as mentioned above, no matter how high the amplitudes of the received signals are, and what type of the added noise is, the proposed track circuit part in the improved track breakage detection system can work properly. The system can receive the transmitted signals through 1km-long track sections, and it can detect the corresponding correlation peaks by means of the proposed 63-bit Kasami sequence modulated signal transmission scheme as well as the adaptive peak detection algorithm. Even though in some cases of incomplete track breakage, the peak value of ACF signal obtained by the receiver end is similar to the peak value under track occupied status, the correct track status can still be determined by detecting the peaks of six continuous ACF signals.

5.4   Conclusion

A novel signal transmission method based on spread spectrum sequences is proposed for the track-circuit based part in the improved track breakage detection system. In order to verify the performance of four selected sets of sequence, the concept of correlation bound is put forward. At the same time, according to the characteristics of received signal, an adaptive peak detection algorithm is discussed here. The signals transmission is simulated by using the electrical models proposed in Chapter 4, and the encoding of the electrical transmission based on the 63-bit Kasami sequences are determined to apply in the system. Finally, through the different experimental tests with different track status and noise environments, the accuracy and reliability of the proposed transmission scheme and adaptive peak detection algorithm are verified.

6 Summary and Future Works

6.1 Summary

In China, rail transportation carries heavy passenger and freight missions. Tracks are an important part of rail transportation, and their integrity affects the safety of train operation. Through the analysis of a large number of accidents caused by track breakage and the causes of track breakage, it is known that real-time, accurate and stable breakage detection of tracks is of great significance. For the detection system, the determination of the track breakage is often based on the processing result of the transmitted signal. Therefore, it is of great significance to denoise the signals and to improve the signal recognition in the track breakage detection system.

6.1.1 Main Contributions

The real-time track breakage detection system is taken as the research background for this thesis. The algorithm of track breakage detection based on UGW signals and electrical signals, as well as the improvement of the track breakage detection system combined with UGW signals and electrical signals is studied. The main contributions of this work are as follows:

1. To solve the problem of window function's time-frequency characteristics contradiction and mode mixing, the method of interference suppression using VMD algorithm is proposed. By applying the VMD algorithm to the simulated UGW signal under different noise conditions, as well as to the experimental signal actually containing noise, the deviation between the reconstructed signal and the original one, as well as the SNR of the reconstructed signal, are calculated to measure the denoising performance. In view of the UGW signal after denoising, a feature extraction method based on different track conditions is proposed. According to the distinction of the two extracted features (the RMS value V_{rms}, and the frequency F_p corresponding to the peak value of the spectrum signal), as well as their respective temporal and spatial dependencies, an ideal of adopting RNN for the determination and classification of the track status is proposed. The extracted features at different time of each track section is used as the input of RNN. Through the calculation of the accuracy of the classification results and the display on the 2D plane, it is known that the RNN can be adopted to carry out real-time detection of track status, thus, the breakage can be found out in time.

2. In view of the situation that the UGW signal cannot propagate through the track breakage maintenance structure, and the previous track breakage detection system based on UGW signal in the repaired track section cannot continue to work normally, an improved track detection system combining UGW signal with the electrical signal is proposed. The improved system is not only compatible with the transmission and processing of UGW signals and electrical signals, but also the performance of power supply units, communication units, as well as other parts in the system have been greatly improved. The improved system can cope with more complex running environment for a train. At the same time, aiming at the track circuit-based part in the improved system, electrical simulation models for a single railway line, as well as for the parallel two railway lines are proposed. In particular, the coupling between two adjacent parallel railway lines under different water content is discussed. These two electrical simulation models provide an appropriate simulation platform for the subsequent analysis of the transmitted electrical signals in track.

3. For the track circuit-based part in the improved track breakage detection system, an electrical signal transmission method using spread spectrum communication for reference is put forward. In order to take advantage of the better performance of sequences (with higher auto-correlation main lobe, as well as lower cross-correlation side), a signal transmission scheme based on the spread spectrum sequences is proposed. In order to verify the performance of four selected sets of sequences, the concept of correlation bound is put forward. At the same time, according to the characteristics of received signal, an adaptive peak detection algorithm is discussed here. The signals transmission is simulated by using the electrical models proposed for the improved system, and the encoding of the electrical transmission based on the 63-bit Kasami sequences are determined to apply in the system. Through the different experimental tests under different track status and noise environments, the accuracy and reliability of the proposed transmission scheme and adaptive peak detection algorithm are verified.

The improved real-time track breakage detection system works mainly based on UGW signals, and supplemented by electrical signals. Through the researches on the processing of UWG and electrical signals, as well as on the determination of track status, it can be concluded that the improved broken track detection system is stable and reliable. It can determine the track status of the detected section, as well as solve the broken track situation in real time, in order to ensure the running safety of the train.

6.1.2 Innovations

This work realizes the denoising, feature extraction and track status recognition in the previous UGW based track breakage detection system. On the basis, the improved tracking detection system combined with electrical signal transmission, as well as the corresponding electrical signal transmission and recognition algorithm are realized. The research involves the following innovations:

1.   A signal denoising, feature extraction and track status classification algorithm for UGW-based track breakage detection system is proposed.

In order to solve the problem of window function selection, mode mixing and inaccurate signal reconstruction in the existing UGW denoising algorithm, this work proposes to apply VMD denoising algorithm for UGW signals. The algorithm can obtain a high SNR reconstructed signal with fewer mode decomposition times. According to the UGW signal received under different track status, a feature extraction method for UGW signal is proposed. By using the differences of features in different track conditions and the temporal and spatial independences among the feature, an algorithm for identifying and classifying track status by using RNN is proposed. The algorithm has high accuracy, and can detect the track status in real time.

2.   An improved real-time track breakage detection system combined with the principle of track circuit detection is proposed, and the corresponding track circuit model is established.

An improved real-time track breakage detection system combined with the principle of track circuit is proposed here. The detection system is compatible both with the transmission and processing of UGW signals and electrical signals, and can be applied to more complicated working environment. And also, the improved system can effectively solve the problem that the previous UGW-based track breakage detection system cannot work normally when there is a broken track maintenance structure in the detected section. The proposed simulation models for single railway line and for the two parallel railway lines which contain electromagnetic coupling, provide a better simulation platform for the electrical transmission.

3.   A new electrical signal transmission scheme is proposed for the improved track breakage detection system.

Based on the idea of DS-SS communication, the Kasami sequences with a length of 63 bits have the characteristics of high auto-correlation peak and low cross-correlation amplitude. Therefore, for the track circuit-based part of the improved detection system,

a transmission scheme to modulate the 125Hz sinusoidal carrier by using the 63-bit Kasami sequence is proposed. The modulated signal propagates the 1km-long track section, and in the receiver end, after demodulation, correlation operations with the same sequences are performed. The method has high signal processing gain and can suppress the effects caused by noises and multipath interferences from other channels.

4. An adaptive peak detection algorithm is proposed, based on the correlation signals obtained in the improved system.

In the improved track breakage detection system, the receiver end finally obtains a series of correlation signals, and the track status of the corresponding detection section is identified according to the peak value of the correlation signal. In order to accurately detect the peak signal, a novel adaptive peak detection algorithm that excludes fixed threshold settings and empirical parameter settings is put forward. The simulation and experimental verification show that the algorithm is stable and reliable.

Based on the above innovations, this work provides a practical solution for real-time track breakage detection.

6.2 Future Works

For the problems of signal identification and detection in the track breakage detection system, future research works can start from the following aspects:

1. **Research on track simulation model.** Due to the wide variety of environments in which the railway lines work, there may be interference between the rails and the ground, between the rails themselves, as well as between the rails and the electrical traction lines. In this work, the electromagnetic interference of rail-to-rail is neglected in the establishment of the simulation model, only the rail-to-ground leakage under different water content is considered. The various influence factors for the electrical simulation model need to be considered in future works.

2. **Research on automatic CBTC system.** In this work, the spread spectrum sequence is used to modulate the phase of the sinusoidal carrier signal, and no information is carried in the signal transmission. However, the automatic CBTC system is currently developing. Therefore, using the sequence to perform the recognition of track status, and using the same sequence to transmit more information (such as position, running speed, and running environment, etc.) is the next step of work.

3. **Research on intelligent algorithm of track breakage detection system.** The railway lines are complex and huge, and the types of signals transmitted in the track are

not the same. In this work, the processing method using the RNN is proposed only for the UGW signal. For various kinds of signals in the monitoring area, how to simultaneously process the state information of all the sections through the intelligent algorithm is the next problem that needs to be solved.

References

[1]   X.H. Qu. Design technology of Qinhuangdao-Shenyang dedicated passenger railway [J]. Journal of Railway Science and Engineering, 2004, 1(1): 32-38.

[2]   F. Xia. High-speed railway changes China [J]. Time Report, 2016, 1: 10-14.

[3]   G. Wang, H.G. Xu. Influence of the belt and road initiative on China high speed railway development [J]. China Transportation Review, 2017, 39(9): 6-9.

[4]   Q.Y. Zhou, Y.H. Zhang, F.S. Liu, et al. The review of the development history of high-speed railway rail technology [J]. China Railway, 2018, 3: 1-8.

[5]   L. Yuan, Y. Yang, Á. Hernández. Improvement of an UGW-based track circuit for operation on repaired railway sections [C]. IEEE 17th International Conference on Ubiquitous Wireless Broadband, 2017: 1-5.

[6]   P.F. Zhang, X.Y. Lei, L. Gao, et al. Analysis of the static monitoring data for CWR on high-speed railway bridge [J]. Journal of Railway Engineering Society, 2016, 11: 40-62.

[7]   X.X. Wu, B. Yang, G.Y. Jia. Fracture reason analysis for rail on line [J]. Physical Testing and Chemical Analysis Part A: Physical Testing, 2010, 46(5): 332-334.

[8]   D. Feng, Z.Y. He, S. Lin, et al. Risk index system for catenary lines of high-speed railway considering the characteristics of time-space differences [J]. IEEE Transactions on Transportation Electrification, 2017, 3(3): 739-749.

[9]   H. Dong, B. Ning, B.G. Cai, et al. Automatic train control system development and simulation for high-speed railways [J]. IEEE Circuits and Systems Magazine, 2010, 10(2): 6-18.

[10]   M. Lesk. Safety risks---human error or mechanical failure: Lessons from railways [J]. IEEE Security and Privacy, 2015, 13(2): 99-102.

[11]   J.J. Garcia, C. Losada, F. Espinosa, et al. Optimal estimation techniques to reduce false alarms in railway obstacle detection [C]. IEEE International Conference on Industrial Technology, 2005.

[12]   J.J. Garcia, J. Urena, M. Mazo, et al. Sensory system for obstacle detection on high-speed lines [J]. Transportation Research Part C, 2010, 18(4): 536-553.

[13]   J.J. Garcia, A. Hernandez, J. Urena, et al. FPGA-based architecture for a multisensory barrier to enhance railway safety [J]. IEEE Transaction on Instrumentation and Measurement, 2016, 65(6): 1352-1363.

[14]   X.P. Meng. Analysis and countermeasure research on the problem of rail breakage preventation [J]. China Railway, 2016, 8: 25-29.

[15]   A.A. Markov, D.A. Shpagin, M.N. Shilov. Ultrasonic multichannel flaw detector for testing rails with signal recording [J]. Russian Journal of Nondestructive Testing, 2003, 39(2): 105-114.

[16]   Q.G. Yuan, J.M. Zhang, L.W. Man. Investigation on structure and dynamics of rail flaw detection vehicle [J]. Applied Mechanics and Materials, 2013(446-447): 635-639.

[17]   M.X. Lin. ScanMaster immersed ultrasonic C-scan testing system [J]. Nondestructive Testing，2010, 32(12): 994-996.

[18]   Y.B. Wang. Reflections on the effective use of "skylights" in the railway hub area of standard speed train [J]. Shanghai Railway Science and Technology, 2017, 4: 38-39.

[19]   Y.S. Shi, Y.H. Zhang, P. Li, et al. Exploring on dynamic sensitivity setting of rail flaw detection vehicle used on high speed railway [J]. Railway Engineering, 2014, 9: 113-116.

[20]   Y.H. Zhang, G.Y. Xu, P. Li, et al. Key technology to autonomous ultrasonic detection system of rail flaw detection car [J]. China Railway Science, 2015, 36(5): 131-136.

[21]   H.Y. Tam, S.Y. Liu, B.O. Guan, et al. Fiber bragg grating sensors for structural and railway applications [C]. Proceedings Photonics Asia: Advanced Sensor Systems and Application II, 2004: 85-97.

[22]   T.H.T. Chan, L. Yu, H.Y. Tam, et al. Fiber bragg grating sensors for structural health monitoring of Tsing Ma bridge: Background and experimental observation [J]. Engineering Structures, 2006, 28(5): 648-659.

[23]   Y. Wang, Z.J. Yu, L.Q. Zhu. Automatic detection of fence completeness for high-speed railway [C]. IEEE International Conference on Service Operations, Logistics and Informatics, 2011: 585-588.

[24]   Y.J. Zhang, F. Liu, Y.H. Jing, et al. Application of FBG sensing technique for monitoring and early warning system of high-speed railway track conditions [C]. 25th International Conference on Optical Fiber Sensors, 2017.

[25]   A. Catalano, F.A. Bruno, C. Galliano, et al. An optical fiber intrusion detection system for railway security [J]. Sensors and Actuators A: Physical, 2017(253): 91-100.

[26]   D. Hesse, P. Cawley. A single probe spatial averaging technique for guided waves and its application to surface wave rail inspection [J]. IEEE Transactions on Ultrasonics, Ferroelectrics, and Frequency Control, 2007, 54(11): 2344-2356.

[27]   C.M. Lee. J.L. Rose, Y.H. Cho. A guided wave approach to defect detection under shelling in rail [J]. NDT and E International, 2009, 42(3): 174-180.

[28]   S. Coccia, I. Bartoli, A. Marzani, et al. Numerical and experimental study of guided waves for detection of defects in the rail head [J], NDT and E International, 2011, 44(1): 93-100.

[29]   S. Moustakidis, V. Kappatos, P. Karlsson, et al. An intelligent methodology for railways monitoring using ultrasonic guided waves [J]. Journal of Nondestructive Evaluation, 2014, 33(4): 694-710.

[30]   P.W. Loveday, C.S. Long. Laser vibrometer measurement of guided wave modes in rail track [J]. Ultrasonics, 2015(57): 209-217.

[31]   P.W. Loveday, C.S. Long, D.A. Ramatlo. Mode repulsion of ultrasonic guided waves in rails [J]. Ultrasonics, 2018(84): 341-349.

[32]   M. Evans, A. Lucas, I. Ingram. The inspection of level crossing rails using guided waves [J]. Construction and Building Materials, 2018(179): 614-618.

[33]   J.J. Wu, Z.F. Tang, F.Z. Lu, et al. Ultrasonic guided wave focusing in waveguides with constant irregular cross-sections [J]. Ultrasonics, 2018(89): 1-12.

[34]   D.A. Ramatlo, D.N. Wilke, P.W. Loveday. Development of an optimal piezoelectric transducer to excite guided waves in a rail web [J]. NDT and E International, 2018(95): 72-81.

[35]   R.P. Reiff. Acoustic rail-break detection demonstration at MTA New York city transit [J]. Transit Cooperative Research Results Digest, 2006(2): 1-7.

[36]   C. Nucera, R. Phillips, L. Francesco. Ultrasonic guided wave monitoring of railroad tracks [J]. Advances in Science and Technology, 2013, 83(83): 198-207.

[37]   J. Chen, C. Roberts, P. Weston．Fault detection and diagnosis for railway track circuits using neuro-fuzzy system [J]. Control Engineering Practice, 2008, 16(5): 585-596.

[38]   L. Oukhellou, A. Debiolles, T. Denoeux, et al. Fault diagnosis in railway track circuits using Dempster-Shafer classifier fusion [J]. Engineering Applications of Artificial Intelligence, 2010, 23(1): 117-128.

[39]   L.H. Zhao, J.P. Wu, Y.K. Ran. Fault diagnosis for track circuit using AOK-TFRs and AGA [J]. Control Engineering Practice, 2012, 20(12): 1270-1280.

[40]   K. Verbert, B.D. Schutter, R. Babuska. Fault diagnosis using spatial and temporal information with application to railway track circuits [J]. Engineering Applications of Artificial Intelligence, 2016(56): 200-211.

[41]   J.L. Wybo. Track circuit reliability assessment for preventing railway accidents [J]. Safety Science, 2018(3): 1-8.

[42]   M.X. Tian, B. Zhao, Y.Z. Min. A novel method of real-time broken rail detection based on principle of track circuits [J]. Journal of Lanzhou Jiaotong University, 2013, 32(1): 58-62.

[43]   K.P. Liu, Y.P. Zhang, B. Zhao, et al. Design of transmission system of real-time broken rail detection [J]. Journal of Railway Science and Engineering, 2013, 10(1): 123-128.

[44]   M.X. Tian, Y.F. Chen, B. Zhao, et al. Summary of real-time broken rail detection methods[J]. Journal of Lanzhou Jiaotong University ,2011, 30(1): 122-126.

[45]   M. Guerrieri, G. Parla, C. Celauro. Digital image analysis technique for measuring railway track defects and ballast gradation [J]. Measurement, 2018(113): 137-147.

[46]   V.K. Chillara, B. Ren, C.J. Lissenden. Guided wave mode selection for inhomogeneous elastic waveguides using frequency domain finite element approach [J]. Ultrasonics, 2016(67): 199-211.

[47]   P.W. Loveday, C.S. Long, D.A. Ramatlo. Mode repulsion of ultrasonic guided waves in rails [J]. Ultrasonics, 2018(84): 341-349.

[48]   A. Angulo, J. Allwright, C. Mares, et al. Finite element analysis of crack growth for structural health monitoring of mooring chains using ultrasonic guided waves and acoustic emission [J]. Procedia Structural Integrity, 2017(5): 217-224.

[49]   M.A. Fakih, S. Mustapha, J. Tarraf, et al. Detection and assessment of flaws in friction stir welded joints using ultrasonic guided waves: experimental and finite element analysis [J]. Mechanical Systems and Signal Processing, 2018(101): 516-534.

[50]   J.L. Rose, M.J.A. Jr, Y. Cho. Elastic wave analysis for broken rail detection [J]. American Institute of Physics, 2002(615): 1806-1812.

[51]   S. Fateri, N.V. Boulgouris, A. Wilkinson, et al. Frequency-sweep examination for wave mode identification in multi-model ultrasonic guided wave signal [J]. IEEE Transactions on Ultrasonics, Ferroelectrics, and Frequency Control, 2014, 61(9): 1515-1524.

[52]   O.R. Gericke. Spectrum and contour analysis of ultrasonic pulses for improved nondestructive testing [J]. 1960.

[53]   H. Kwun, K.A. Bartels, C. Dynes. Dispersion of longitudinal waves propagating in liquid-filled cylindrical shells [J]. Journal of the Acoustical Society of America, 1999, 105(5): 2601-2611.

[54]   N. Marc, L.J. Jacobs, J.M. Qu, et al. Time-frequency representations of Lamb waves [J]. Acoustical Society of America, 2001, 109(5): 1841-1847.

[55]   H.Z. Hosseinabadi, B. Nazari, R. Amirfattahi, et al. Wavelet network approach for structural damage identification using guided ultrasonic waves [J]. IEEE Transactions on Instrumentation and Measurement, 2014, 63(7): 1680-1692.

[56]   T. Liu, J. Li, X.F. Cai, et al. A time-frequency analysis algorithm for ultrasonic waves generating from a debonding defect by using empirical wavelet transform [J]. Applied Acoustics, 2018(131): 16-27.

[57]   M.H.S. Siqueira, C.E.N. Gatts, R.R. Silva, et al. The use of ultrasonic guided waves and wavelets analysis in pipe inspection [J]. Ultrasonics, 2004, 41(10): 785-797.

[58]   R. Sharma, S.R.M. Prasanna, R.K. Bhukya, et al. Analysis of the intrinsic mode functions for speaker information [J]. Speech Communication, 2017(91): 1-16.

[59]   K.S. Biju, M.G. Jibukumar. Ictal EEG classification based on state space modeling of intrinsic mode functions [J]. Procedia Computer Science, 2018(125): 468-475.

[60]   M.B.A. Malek, S.S. Hanna. Using filter bank property to simplify the calculations of empirical mode decomposition [J]. Communications in Nonlinear Science and Numerical Simulation, 2018(62): 429-444.

[61]   D.K.B. Ismail, P. Lazure, I. Puillat. Advanced spectral analysis and cross correlation based on the empirical mode decomposition: application to the environmental time series [J]. IEEE Geoscience and Remote Sensing Letters, 2015, 12(9): 1968-1972.

[62] Z.H. Wu, N.E. Huang. Ensemble empirical mode decomposition: a noise assisted data analysis method [J]. Advances in Adaptive Data Analysis, 2009(1): 1-41.

[63] Z.Y. Shen, N.Z. Feng, Y. Shen, et al. A ridge ensemble empirical mode decomposition approach to clutter rejection for ultrasound color flow imaging [J]. IEEE Transactions on Biomedical Engineering, 2013, 60(6): 1477-1487.

[64] S.C. Lin, P.C. Li. Automatic contrast enhancement using ensemble empirical mode decomposition [J]. IEEE Transactions on Ultrasonics, Ferroelectrics, and Frequency Control, 2011, 58(12): 2680-2688.

[65] C.H. Chen, G.G. Lee. Neural network for ultrasonic NDE signal classification using time-frequency analysis [C]. International Conference on Acoustics, Speech, and Signal Processing, 1993(1): 493-496.

[66] L. Sylvie, M. Daniel. Neural classification of lamb wave ultrasonic weld testing signals using wavelet coefficients [J]. IEEE Transactions on Instrumentation and Measurement, 2001, 50(3): 672-678.

[67] M. Solis, H. Benitiz. Location of material flaws using wavelet analysis and neural network [C]. IEEE Ultrasonic Symposium, 2002: 841-844.

[68] V.F. Grappone. Broken rail detector for communications-based train control and positive train control applications: US, US6655639 [P]. 2003.

[69] Y. Chen. Discussion on the test scheme of the true root mean square value of the asymmetric high voltage impulse signals [J]. Railway Signalling and Communication, 2014, 50(2): 18-20.

[70] G.Q. Li, X.C. Wu. Application of ZFFT algorithm based on multiple modulation in detection of track circuit signal [J]. Computer Measurement and Control, 2016, 24(1): 262-265.

[71] R.J. Hill. Optimal construction of synchronizable coding for railway track circuit data transmission [J]. IEEE Transactions on Vehicular Technology, 1990, 39(4): 390-399.

[72] R. Escudero, A. Hernández, M.C. Pérez, et al. Local maximum detection for active sensory systems based on encoding and correlation techniques [J]. IEEE International Instrumentation and Measurement Technology Conference, 2012: 1697-1702.

[73]   V. Osipov, M. Osipov. Space-time signal binding in recurrent neural networks with controlled elements [J]. Neurocomputing, 2018(308): 194-204.

[74]   W. Zhang, C.D. Li, T.W. Huang, et al. Synchronization of memristor-based coupling recurrent neural networks with time-varying delays and impulses [J]. IEEE Transactions on Neural Networks and Learning Systems, 2015, 26(12): 3308-3313.

[75]   H.L. Deng, L. Zhang, X. Shu. Feature memory-based deep recurrent neural network for language modeling [J]. Applied Soft Computing, 2018(68): 432-446.

[76]   D.P. Tao, X. Lin, L.W. Jin, et al. Principal component 2-D long short-term memory for font recognition on single Chinese characters [J]. IEEE Transactions on Cybernetics, 2016, 46(3): 756-765.

[77]   X.Y. Song, R. Ward. Deep sentence embedding using long short-term memory networks: analysis and application to information retrieval [J]. IEEE/ACM Transactions on Audio, Speech, and Language Processing, 2016, 24(4): 694-707.

[78]   K. Bunte, S. Haase, M. Biehl, et al. Stochastic neighbor embedding for dimension reduction and visualization using arbitrary divergences [J]. Neurocomputing, 2012(90): 23-45.

[79]   L.V.D. Maaten, G. Hinton. Viualizing data using t-SNE [J]. Journal of Machine Learning Research, 2008(9): 2579-2605.

[80]   X.J. Shu, J. Wang, H.B. Wang, et al. Chaotic direct sequence spread spectrum for secure underwater acoustic communication [J]. Application Acoustics, 2016(104): 57-66.

[81]   N.X. Quyen, T.Q. Duong, N.S. Vo, et al. Chaotic direct-sequence spread-spectrum with variable symbol period: A technique for enhancing physical layer security [J]. Computer Networks, 2016(109): 4-12.

[82]   E. Garcia, J.A. Paredes, F.J. Alvarez, et al. Spreading sequences in active sensing: A review [J]. Signal Processing, 2015, 106: 88-105.

[83]   H.M. Wei. Spread spectrum communication and application [M]. Xi'an, Xidian University Press, 2007: 17-23.

[84]   J. Aparicio, A. Jimenez, F.J. Alvarez, et al. Accurate detection of spread-spectrum modulated signals in reverberant underwater environments [J]. Applied Acoustics, 2015, 88: 57-65.

[85]   J. Aparicio, A. Jimenez, F.J. Alvarez, et al. Characterization of an underwater positioning system based on GPS surface nodes and encoded acoustic signals [J]. IEEE Transactions on Instrumentation and Measurement, 2016, 65(8): 1773-1784.

[86]   S. Stanczak, H. Boche. Are LAS-codes a miracle? [C]. IEEE Global Telecommunications Conference, 2001.

[87]   L. Freitag, M. Stojanovic, M. Singh, et al. Analysis of channel effects on direct-sequence and frequency-hopped spread-spectrum acoustic communication [J]. IEEE Journal of Oceanic Engineering, 2001, 26(4): 586-593.

[88]   M.C. Perez, J. Urena, C.D. Marziani, et al. Very efficient correlator for loosely synchronized codes [J]. Electronics Letters, 2010, 46(16): 1127-1129.

[89]   E. Garcia, J. Urena, J.J. Garcia, et al. Multilevel LS sequences with flexible ZCZ length and their application to local positioning systems [C]. IEEE International Instrumentation and Measurement Technology Conference Proceedings, 2012.

[90]   L.R. Welch. Lower bounds on the maximum cross-correlation of signals [J]. IEEE Transactions Information Theory, 1974(20): 397-399.

[91]   T. Kasami. Weight distribution formula for some class of cyclic codes [M]. US: University of North Carolina Press, 1969.

[92]   F. Liu, X.L. Tong, C. Zhang, et al. Multi-peak detection algorithm based on the Hilbert transform for optical FBG sensing [J]. Optical Fiber Technology, 2018(45): 47-52.

[93]   N. Sangeetha, X. Anita. Entropy based texture watermarking using discrete wavelet transform [J]. Optik, 2018(160): 380-388.

[94]   K. Dragomiretskiy, D. Zosso. Variational mode decomposition [J]. IEEE Transactions on Signal Processing, 2014, 62(3): 531-544.

[95]   J.C. Carcia, J.A. Jimenez, F. Espinosa, et al. Characterization of railway line impedance based only on short-circuit measurements [J]. International Journal of Circuit Theory and Applications, 2015, 43(8): 984-994.

[96]   A. Mariscotti, P. Pozzobon. Determination of the electrical parameters of railway traction lines: calculation, measurement, and reference data [J]. IEEE Transactions on Power Delivery, 2004, 19(4): 1538-1546.

[97]   J.H. Scott, R.D. Carrol, D.R. Cunningham. Dielectric constant and electrical conductivity measurements of moist rock: A new laboratory method [J]. Journal of Geophysical Research，1967, 72(20): 5101-5115.

[98]   F.J. Álvarez, J. Ureña, J.J. García, et al. A comparative analysis of two modulation schemes for the efficient transmission of complementary sequences in a pulse compression ultrasonic system [C]. Internatioanl Conference on Telecommunications and Computer Networks, San Sebastian, Spain, 2004.

[99]   D. Sarwate, M. Pursley. Cross-correlation properties of pseudo-random and related sequences. Proceedings of the IEEE. 1980, 68(5):593-619.

[100]   P. Fan, M. Darnell. Sequence design for communications applications [M]. England: Research Studies Press LTD., 1996.

[101]   J. Lahtonen. On the odd and the aperiodic correlation properties of the Kasami sequences [J]. IEEE Transactions on Information Theory, 1995, 41(5):1506-1508.

[102]   J.X. Song, P. Babu, D.P. Palomar. Optimization methods for designing sequences with low autocorrelation sidelobes. IEEE Transactions on Signal Processing, 2015, 63(15): 3998-4009.

[103]   F.J. Alvarez, A. Hernandez, J.A. Moreno, et al. Doppler-tolerant receiver for an ultrasonic LPS based on Kasami sequences [J]. Sensors and Actuators A: Physical, 2013, 189: 238-253.

[104]   L. Yuan, Y. Yang, A. Hernández. Improvement of high-voltage impulses in track circuits with Kasami and LS codes [J]. International Journal of Circuit Theory and Application, 2018(4): 926-941.

[105]   D. Panigrahy, M. Rakshit, and P.K. Sahu, FPGA implementation of heart rate monitoring system [J]. Journal of Medical Systems, 2016, 40(3): 49.

[106]   R. Gutiérrez-Rivas, J.J. García, W.P. Marnane, et al. Novel real-time low-complexity QRS complex detector based on adaptive thresholding [J]. IEEE Sensors Journal, 2015, 15(10): 6036–6043.

[107]   P. Sasikala, R.S.D. Wahidabanu. Robust R peak and QRS detection in electrocardiogram using wavelet transform [J]. International Journal of Advanced Computer Science and Applications, 2010, 1(6): 48–53.

[108] M. Rakshit, S. Das. An efficient wavelet-based automated R-peaks detection method using Hilbert transform [J]. Biocybernetics and Biomedical Engineering, 2017, 37(3): 566–577.

[109] J.J. Di, L.C. Zhang. Research on asymmetric pulse signal waveform based on wavelet analysis [J]. Modern Electronics Technique, 2012, 35(3): 123–128.

[110] S.G. Mallat. Multifrequency channel decompositions of images and wavelet models [J]. IEEE Transactions on Acoustics Speech and Signal Processing, 1989, 37(12): 2091–2110.

[111] J.H. Jiao, Y.H. Wen, M. Li, et al. Research on vehicle onboard measurement system of traction harmonic current for analyzing interference on track circuit [C]. IEEE International Symposium on Microwave, Antenna, Propagation and EMC Technologies, Shanghai, China, Oct. 2015.

Achievements during the Period of Ph.D

1. **Lei Yuan**, Yuan Yang, Álvaro Hernández. Improvement of high-voltage impulses in track circuits with Kasami and LS codes [J], International Journal of Circuit Theory and Applications, 2018, 46(4): 926-941. (SCI index：000430108000016)

2. **Lei Yuan**, Yuan Yang, Álvaro Hernández, Lin Shi. Feature extraction for track section status classification based on UGW signals [J].Sensors, 2018, 18(4): 1225-1246.
    (SCI index：000435574800297)

3. **Lei Yuan**, Yuan Yang, Álvaro Hernández, Lin Shi. Novel adaptive peak detection method for track circuits based on encoded transmissions [J]. IEEE Sensors Journal, 2018, 18(15)：6224-6234. (SCI index：000438730200023)

4. Yuan Yang，**Lei Yuan**，Jiaxu Wang. Modified digital filter algorithm for high-voltage impulse track circuit [J]. Information and Control （Accepted, in Chinese）

5. Yuan Yang, **Lei Yuan**. The design of a novel digital asymmetric HVI code generator [C]. Proceedings of the 2015 International Conference on Electrical and Information Technologies for Rail Transportation (EITRT 2015), Zhuzhou, China, Oct. 17-19, 479-487, 2015. (EI index：20161202139471)

6. **Lei Yuan**, Yuan Yang, Álvaro Hernández. A simulation model for high-voltage impulse track circuits [C]. XXII Seminario Anual de Automática, Electrónica Industrial e Instrumentación (SAAEI 2016), Elche, Spain, Jul. 6-8, 2016.

7. **Lei Yuan**, Yuan Yang, Álvaro Hernández. Track circuit improvement with high-voltage impulse encoding [C]. 21st IEEE International Conference on Emerging Technologies & Factory Automation (ETFA 2016), Berlin, Germany, Sept. 6-9, 2016.

8. **Lei Yuan**, Yuan Yang, Álvaro Hernández. Improvement of an UGW-based track circuit for operation on repaired railway sections [C]. IEEE 17th International Conference on Ubiquitous Wireless Broadband (ICUWB 2017), Salamanca, Spain, Sept. 12-15, 2017. (EI index：20181805117465)

9. **Lei Yuan**, Yuan Yang, Álvaro Hernández, Shuyu Li. Application of VMD algorithm in UGW-based rail breakage detection system [C]. 20th IEEE International Conference on Vehicular Electronics and Safety (ICVES 2018), Madrid, Spain, Sept. 12-14, 2018.